

Controlled few-body interactions in ultracold bosonic mixtures

Dissertation

zur

Erlangung des Doktorgrades (Dr. rer. nat.)

der

Mathematisch-Naturwissenschaftlichen Fakultät

der

Rheinischen Friedrich-Wilhelms-Universität Bonn

vorgelegt von

Claudia Weber

aus

Düsseldorf

Bonn 2009

Angefertigt mit Genehmigung der Mathematisch-Naturwissenschaftlichen Fakultät
der Rheinischen Friedrich-Wilhelms-Universität Bonn

1. Gutachter: Prof. Dr. Dieter Meschede
2. Gutachter: Prof. Dr. Massimo Inguscio

Tag der Promotion: 16.02.2010

Erscheinungsjahr: 2010

Diese Dissertation ist auf dem Hochschulschriftenserver der ULB Bonn
http://hss.ulb.uni-bonn.de/diss_online elektronisch publiziert.

Zusammenfassung

Gegenstand dieser Arbeit sind zwei Experimente mit heteronuklearen Bose-Bose Gemischen.

Das Ziel des ersten Experiments ist die kontrollierte Dotierung eines Rubidium-Bose-Einstein-Kondensats mit einzelnen Cäsium-Atomen. Letztere können die Rolle einer nicht-destruktiven Messsonde übernehmen um quantenmechanische Prozesse zeit- und orts aufgelöst zu untersuchen. Im Rahmen dieser Arbeit wird die Erzeugung und Speicherung beider Komponenten, einzelne Atome und Kondensat, sowie deren Detektion realisiert. In einem ersten Experiment werden bis zu zehn Cäsium-Atome als Messsonde in Kontakt mit einer kalten Rubidium-Atomwolke gespeichert und aus der Einzelatomdynamik werden Wechselwirkungsparameter extrahiert. Damit ist ein wichtiger Schritt auf dem Weg zur kontrollierten Dotierung eines Kondensats erfolgt.

Das Ziel des zweiten Experiments ist die Erzeugung und Spektroskopie ultrakalter heteronuklearer Kalium-Rubidium-Moleküle mit universellen Eigenschaften. Nahe zweier magnetischer s -Wellen-Feshbach-Resonanzen werden schwachgebundene Kalium-Rubidium-Moleküle in hohen Vibrationszuständen hergestellt und ihre Bindungsenergie sowie die Position der zugehörigen Feshbachresonanz bestimmt. Zusammen mit zwei schmalen d -Wellen-Feshbachresonanzen bilden sie die Grundlage für eine präzisere Parametrisierung des Kalium-Rubidium-Molekülpotentials. Dessen genaue Kenntnis dient der Optimierung der Transfermethoden um die Moleküle über kohärente Kopplung in den Vibrationsgrundzustand zu bringen. Diese Moleküle besitzen ein permanentes Dipolmoment, deren anisotrope, langreichweitige Dipol-Dipol-Wechselwirkung z.B. für Anwendungen in der Quanteninformationsverarbeitung von Interesse ist.

Abstract

In this thesis two experiments with heteronuclear Bose-Bose mixtures are discussed. The goal of the first experiment is a controlled doping of a rubidium condensate with single caesium atoms. These undertake the task of a non-destructive probe to investigate quantum mechanical phenomena time- and spatially resolved. In this thesis the necessary methods to produce, store, and detect both components, single atoms and the condensate, are realized. In a first experiment up to 10 caesium atoms are stored as a probe in contact with a cold rubidium atomic cloud. The interaction parameters are extracted from the dynamics of the single atoms. This is an important step towards the controlled doping of a condensate.

The aim of the second experiment is the production and spectroscopy of ultracold heteronuclear potassium-rubidium molecules with universal properties. Close to two magnetic s -wave Feshbach resonances weakly bound molecules in high vibrational states are created, and their binding energy and the position of the associated Feshbach resonance are determined. These results in combination with two narrow d -wave Feshbach resonances provide the basis for a more precise parametrization of the potassium-rubidium molecular potential. The knowledge of this is important to identify a proper scheme to transfer the molecules via coherent coupling into their rovibrational ground state. These molecules offer a permanent dipole moment and thus are of particular interest for e.g. quantum information processing due to their anisotropic, long-range dipole-dipole interaction.

Parts of this thesis have been published in the following journal articles:

- M. Haas, V. Leung, D. Frese, D. Haubrich, S. John, C. Weber, A. Rauschenbeutel, and D. Meschede, *Species-selective microwave cooling of a mixture of rubidium and caesium atoms*, New Journal of Physics, 9 (2007), p. 147
- C. Weber, G. Barontini, J. Catani, G. Thalhammer, M. Inguscio, and F. Minardi, *Association of ultracold double-species bosonic molecules*, Phys. Rev. A, 78 (2008), p. 061601
- G. Thalhammer, G. Barontini, J. Catani, F. Rabatti, C. Weber, A. Simoni, F. Minardi, and M. Inguscio, *Collisional and molecular spectroscopy in an ultracold Bose-Bose mixture*, New Journal of Physics, 11 (2009), p. 055044
- G. Barontini, C. Weber, F. Rabatti, J. Catani, G. Thalhammer, M. Inguscio, and F. Minardi, *Observation of Heteronuclear Atomic Efimov Resonances*, Phys. Rev. Lett., 103 (2009), p. 043201

Contents

Introduction	1
1 Ultracold quantum gases	5
1.1 BEC in ideal gases	5
1.2 BEC in weakly interacting gases	7
2 Few-body interactions	11
2.1 Elastic scattering in the limit of low energies	11
2.2 Molecular potentials of alkali atoms	15
2.3 Feshbach resonances and molecules	19
2.3.1 Feshbach resonance	19
2.3.2 Classification and selection rules	21
2.3.3 Universality	22
2.3.4 Theoretical approaches	23
2.3.5 Loss mechanisms	24
3 Towards an ultracold mixture	27
3.1 Vacuum system	27
3.2 Laser system for trapping and detection	29
3.3 Magneto-optical trap	32
3.4 Magnetic trap	36
3.5 Transport of the atoms from the MOT to the QUIC trap	38
3.6 Evaporative cooling	39
3.7 Optical dipole trap	43
3.7.1 Power stabilization of the dipole trap beams	46
3.8 Absorption imaging	49
4 Single Cs atoms in a cold cloud of Rb atoms	53
4.1 Single Cs atom MOT	53
4.2 Fluorescence of single Cs atoms	55
4.3 Cold collisions	60
4.4 Single Cs atoms in the presence of Rb	62
4.4.1 Determination of the number of Rb atoms	63
4.4.2 Experimental sequence	64
4.4.3 Dynamics in the single Cs atom MOT in the presence of Rb	65

5	KRb molecules	73
5.1	Ultracold heteronuclear molecules	73
5.2	Association of ultracold bosonic KRb molecules	75
5.2.1	Experimental preparation of an ultracold K-Rb mixture	75
5.2.2	Association and detection of KRb molecules	77
5.3	Experimental results and analysis	79
5.3.1	Association spectrum	79
5.3.2	Spatial overlap	82
5.3.3	Lifetime of the KRb dimers	85
5.3.4	Modulation amplitude dependence	87
5.3.5	Binding energy and Feshbach position	88
5.3.6	Conclusion	90
5.4	Higher order Feshbach resonances	91
6	Conclusion and outlook	95
6.1	A single Cs atom immersed in a Rb BEC	95
6.1.1	Cooling a single Cs atom to its motional ground state	96
6.1.2	Probing the decoherence of a Rb BEC by a single Cs atom	97
6.2	Heterospecies dimers and trimers	98
6.2.1	Molecules in the rovibrational ground state	98
6.2.2	From dimer to trimer states	99
A	Properties of ^{87}Rb, ^{133}Cs and ^{41}K	103
B	Power stabilization	105
	Bibliography	107

Introduction

Ultracold atoms provide a framework to investigate a broad spectrum of quantum mechanical phenomena, not evident in nature. The invention of laser cooling [1] and evaporative cooling [2] enabled to access a regime where all processes obey the laws of quantum mechanics, and where the preparation, manipulation as well as read-out of well-defined quantum states can be realized rather easily. Thus, this regime allows to experimentally investigate fundamental questions and applications of quantum physics.

The experimental breakthrough has taken place with the first observation of the phase transition to a Bose-Einstein condensate (BEC) [3, 4]. During the following years, plenty of experiments all over the world have been set up building on these results. Their focus is widely spread covering a wide range of applications and research directions.

First experiments investigated the wave nature of particles, the long-range phase coherence and the properties of superfluidity of the novel state of matter by the observation of interference between two BECs [5] and quantized vortices [6]. Different kinds of experiments have studied single particle effects, e.g. Anderson localization [7, 8], where the particle wave functions localize in the presence of disordered potentials. Similar experiments exploiting single particle effects have been realized with single neutral trapped atoms, such as the quantum walk [9].

However, many interesting quantum phenomena in nature rely on the interaction between particles, e.g., superconductivity [10], formation of dimer [11] and trimer states [12] and entanglement [13]. Thus, ultracold neutral atoms have become even more important by the observation of optical [14] and magnetic Feshbach resonances [15] providing a tool to tune the interaction strength and its character in a controlled way.

This tunability of the interaction strength allows to enter a new regime of strongly correlated systems occurring in strongly interacting and strongly confined gases. The most prominent example is the phase transition of a superfluid to a Mott-insulator state [16, 17, 18], where the long-range phase coherence of the superfluid is transformed into particle correlations. The resulting perfectly periodic lattice of matter simulates a defect-free solid, and thus is ideally suited to analyze fundamental processes in the field of condensed matter. Strong correlations have also been induced in low dimensional systems for example by realizing the Tonks-Girardeau gas [19, 20] or the super-Tonks-Girardeau gas [21]. In these one-dimensional strongly interacting gases of bosons the two-particle wave function exhibits a node and the bosons mimic some properties of fermionic systems.

Ultracold gas experiments do not have to be restricted to single species. Extending the quantum gas experiments to heteronuclear mixtures additional phenomena can be studied. Despite the Pauli exclusion principle quantum degeneracy of fermions obeying the Fermi-Dirac statistic can be achieved via sympathetic cooling [22, 23]. Feshbach resonances can be exploited to tune the interaction strength between the mixture components without effecting the interaction within one component. Depending on the character of the interaction, two different regimes, i.e. the BEC and Bardeen-Cooper-Schrieffer (BCS) regimes, emerge, connected via a Feshbach resonance. In the first regime, fermions can form bosonic molecules enabling them to undergo a phase transition to a molecular condensate [24, 25, 26]. In the BCS regime superfluids of cooper pairs have been realized [27], showing an energy gap in their excitation spectrum [28].

Bose-bose mixtures are less intensively studied so far. Two of the few experiments explored the different topologies of heteronuclear condensates in different interaction regimes ranging from phase separation to quenching or a collapse [29, 30].

In this thesis two different research directions of such bosonic double-species mixtures are presented. Most of the time during my PhD I spent at the rubidium-caesium (Rb-Cs) mixture experiment in the group of Prof. D. Meschede in Bonn. In-between I worked six months at the potassium-rubidium (K-Rb) mixture experiment in the group of Prof. M. Inguscio in Florence. Both experiments deal with ultracold heteronuclear mixtures, where the inter-species interaction plays a crucial role. However, the respective main focus of these experiments is very different.

Rb-Cs mixture

In Bonn we work with a strongly imbalanced mixture of Rb and Cs, motivated by striving to control and analyze many-body physics on a single particle level. The minority species can be regarded as an impurity. Two groups have studied imbalanced mixtures in which the impurity concentration is one order of magnitude below the bulk density. The first experiment, a fermionic imbalanced spin mixture, has shown a phase transition from polarons, quasi-particles that form when impurities are dressed with atoms from the majority, to molecules, as the interaction strength between the spin components increases [31]. The second group investigated the quantum transport through a Tonks-Girardeau gas with the impurity atoms as a probe [32]. The impurities are initially localized and show a non-ballistic motion while propagating through the gas, and density fluctuations in the Bose gas are observed.

In the extreme case of only one neutral atom immersed in a BEC, the impurity species performs the task of a probe, which ideally does not disturb the many-body system, but allows to analyze processes such as decoherence [33] or phase fluctuations of a BEC [34] with high spatial and temporal resolution.

In addition, the intriguing field of quantum information processing can be explored with such systems, as neutral atoms are promising candidates for quantum bits (qubits) due to their relatively long coherence times [35]. Quantum information science requires large systems, where coherent interactions can entangle particles and external manipulations

can be performed with single particle and high spatial resolution. In two complementary approaches so far only one of these requirements could be realized in each case:

In a top-down approach a Mott-insulator provides an array of qubits which can be entangled in a parallel way via controlled cold collisions [13]. However, single-site addressing and probing pose a challenge. Recently, single-atoms in two-dimensional optical lattices have been imaged single-site resolved, utilizing fluorescence detection [36] or an electron beam microscope ionizing the neutral atoms [37].

In the complementary approach, called bottom-up approach, single atoms can be prepared [38], manipulated [39], and detected [40] with large spatial resolution, ideally with single-site resolution. However, for single atoms the relatively large temperature still makes the realization of coherent interactions challenging. Entangling of single atoms has been realized by Rydberg blockades [41, 42], and is predicted to be obtained in high finesse cavities [43], where the coupling is mediated by photons of the cavity light field, or by controlled cold collisions analogous to the Mott-insulator case [13].

In our Rb-Cs experiment we will combine the two limits and extremes of single atoms and the BEC taking the advantage of each system. This is on the one hand the high control over the preparation, manipulation and detection of single atoms and on the other hand the intrinsically coherent interaction in BECs. This combined system will offer us the opportunity to study many new open questions. The numerous proposals made for problems to be studied in such a system include: Using an atom in a superposition state, the phase fluctuations of the BEC can be studied time dependently and non-destructively [34]. Another opportunity is to measure the decoherence of the BEC [33]. Here, a controlled interaction between the two species will allow us to entangle an atom in a superposition state with the BEC, while the decoherence is imprinted on the phase between the two qubit states.

Besides probing the BEC, the quantum gas can act as a bath coherently cooling the single atom, where the cooling mechanism relies on Bogoliubov excitations. This cooling scheme is proposed to reduce the temperature of the single atom without destroying its internal state, even a possibly present entanglement between different single atoms remains undisturbed [44, 45]. Furthermore, the coherent interaction of BECs can be exploited to transfer quantum information between two spatially separated atoms mediated by phonons due to Bogoliubov excitations in the BEC [46].

By continuously increasing the number of impurity atoms, their effect on the many-body system becomes more and more prominent. This will allow us to investigate a transition from the few-body to the many-body system, where the two species collectively interact.

In this thesis I present the experimental realization of the two components, single Cs atoms and a Rb BEC, and their probing. We show, in a first experiment, one single atom being applicable to probe a many-body system without disturbing it. Hereby, the inelastic cold collision rate between Rb and Cs is determined by analyzing the trapped single atoms dynamics. This way, our system provides an ideal starting point for the controlled doping of a Rb BEC with a single Cs atom.

K-Rb mixture

In Florence, we are aiming to produce deeply bound heteronuclear molecules in the rovibrational ground state from a balanced bosonic K-Rb mixture. These molecules are of broad interest, as they offer a significant permanent dipole moment due to their difference in mass. Their long-range, anisotropic dipole-dipole interaction can be of the same order of magnitude of or even exceed the contact potential interaction dominant in highly excited states. This provides a starting point for producing dipolar condensates [47], up to now only realized with atomic Cr [48], and for searching for predicted new quantum phase transitions [49, 50]. Furthermore, dipolar samples may assist in the search of fundamental constants, e.g. a permanent electric dipole moment of the electron [51, 52]. Moreover, ultracold molecules open up the possibility of high precision molecular spectroscopy, linking molecular physics to the field of ultracold chemistry. Trapped in an optical lattice, these molecules in their rovibrational ground state can provide an array of qubits. The long-range interaction of these dipolar ensemble can be used for applications in quantum information science [53].

In comparison to atoms, diatomic molecules additionally have one translational and three rotational degrees of freedom resulting in complex molecular spectra. Thus, the well-known cooling techniques investigated in atomic physics cannot be efficiently applied in molecular gases. Associating molecules directly from ultracold atoms overcomes this challenge. By using different methods, such as photoassociation [11] and magnetoassociation [54, 55, 56] ultracold molecules have been created. Different technical approaches to associate weakly bound molecules include crossing a Feshbach resonance from the attractive to the repulsive interaction side, applying a radio frequency [57, 58], and modulating the homogeneous magnetic field [59] close to the Feshbach resonance. By means of these methods, ultracold weakly bound homonuclear molecules [60, 61, 62, 63], as well as fermionic heteronuclear molecules [64, 65, 58], and bosonic heteronuclear molecules composed of two isotopes [66], have been generated. Applying stimulated Raman adiabatic passages the weakly bound molecules can be transferred into the rovibrational ground state [67, 68].

In this thesis I present the association of KRb molecules, using the technique of modulating the magnetic field close to two different *s*-wave Feshbach resonances. These ultracold weakly bound molecules are the first step to produce molecules in the rovibrational ground state. The determination of their binding energy allows to precisely extrapolate the position of the two *s*-wave Feshbach resonances used. In addition, we have performed Feshbach spectroscopy on two *d*-wave resonances. The combination of these measurements allows to optimize the models of the KRb molecular potentials, the knowledge of which is essential in order to identify a proper scheme to transfer the molecules into the rovibrational ground state.

1 Ultracold quantum gases

Already in 1925 S. Bose and A. Einstein predicted the phase transition of a thermal gas to a Bose-Einstein condensate (BEC) [69]. Seventy years later the first BEC was achieved experimentally with the alkali atoms rubidium and sodium [3, 4]. A BEC describes a state of matter in which the ground state for a system of indistinguishable bosonic particles is macroscopically populated below a critical temperature. This quantum mechanical phenomenon is based on the wave-like nature of atoms, in contrast to classical systems where atoms are treated as point-like particles. According to Louis de Broglie each particle with mass m can be represented as a wave packet characterized by the so-called de-Broglie wavelength

$$\lambda_{\text{dB}} = \frac{h}{\sqrt{2\pi m k_{\text{B}} T}}. \quad (1.1)$$

The wave-like nature becomes more and more prominent when the temperature T decreases. The phase transition to the BEC starts, when the de-Broglie wavelength becomes as large as the inter-particle distance.

1.1 BEC in ideal gases

Originally, the occurrence of a phase transition to a BEC has been predicted for an ideal gas of bosons. Here, ideal denotes the case of non-interacting particles. Bosons are particles with an integer total spin, characterized by a symmetric wave function under permutation of two identical particles. They obey the Bose-Einstein statistics, thus for non-interacting bosons the population distribution for the n -th energy eigenstate with energy E_n is given by the Bose-Einstein distribution

$$f(E_n) = \frac{1}{e^{(E_n - \mu)/k_{\text{B}} T} - 1}. \quad (1.2)$$

The chemical potential μ tends to the ground state energy E_0 , when the temperature decreases. Hence, the occupation of the lower energetic states increases for a decreasing temperature. For ultracold bosonic gases stored in a harmonic trap with trapping frequencies ω_i along the i -axis the density of states is given by [70]

$$g(E) = \frac{E^2}{2\hbar^3 \omega_x \omega_y \omega_z}, \quad (1.3)$$

where

$$V(\vec{r}) = \frac{1}{2}m(\omega_x^2 x^2 + \omega_y^2 y^2 + \omega_z^2 z^2) \quad (1.4)$$

is the harmonic oscillator potential. Hence, the atom number of the excited energy states can be calculated to be

$$N_{\text{ex}} = \int_{E_0}^{\infty} g(E) f(E) dE. \quad (1.5)$$

Equation (1.5) is only valid for an average energy much larger than the energy difference of two neighbouring energy states. Lowering the temperature for a fixed total number of atoms the chemical potential approaches the ground state energy. At a critical temperature T_c corresponding to the limit $\mu = E_0$, the number of atoms in the excited state significantly decreases below the total atom number N_{tot} leading to a macroscopic population of the ground state which is given by

$$N_0 = N_{\text{tot}} - N_{\text{ex}}. \quad (1.6)$$

Thus, for a bosonic gas stored in a harmonic trap with a mean trapping frequency of $\bar{\omega} = (\omega_x \omega_y \omega_z)^{1/3}$ the critical temperature at which the phase transition occurs can be written as [70]

$$k_B T_c = h \bar{\omega} \left(\frac{N_{\text{tot}}}{\zeta(3)} \right)^{1/3} \approx 0.94 \hbar \bar{\omega} N_{\text{tot}}^{1/3}, \quad (1.7)$$

where $\zeta(\alpha) = \sum_{n=1}^{\infty} n^{-\alpha}$ is the Riemann zeta function. In the case of a uniform gas inside a box of volume V with a density of $n = N/V$ the critical temperature is obtained to be

$$k_B T_c = \frac{2\pi \hbar^2}{m} \left(\frac{n}{\zeta(3/2)} \right)^{2/3} \approx 3.31 \frac{\hbar^2 n^{2/3}}{m}. \quad (1.8)$$

The latter equation can be rewritten in the commonly used form

$$n \lambda_{\text{dB}}^3 = \zeta(3/2) \approx 2.612, \quad (1.9)$$

where the left side of equation (1.9) is denoted as the phase space density. It determines the number of atoms located in a volume with an edge length given by the de-Broglie wavelength. Regarding this condition in the wave picture, the criterion for the phase transition (1.9) corresponds to an overlap of wavepackets with an extent of λ_{dB} . For harmonic traps the uniform density n has to be replaced by the peak density of the trap centre [71]. The number of atoms within the condensate varies for a given total number of atoms with the temperature of the atomic cloud. The condensed fraction for an atomic cloud stored in a harmonic trap is given by

$$\frac{N_0}{N_{\text{tot}}} = 1 - \left(\frac{T}{T_c} \right)^3. \quad (1.10)$$

This relation is only valid for temperatures below the critical temperature.

In addition to the temperature of the cloud, the atomic density distribution is another experimental observable which characterizes the atomic gases. In the case of a pure condensate all atoms populate the ground state. Thus, the density distribution $n_{\text{ideal}}(\vec{r})$ of a non-interacting condensate is given by the ground state wave function ϕ_0 yielding a Gaussian shape

$$n_{\text{ideal}}(\vec{r}) = N_0 |\phi_0(\vec{r})|^2 \quad (1.11)$$

$$= \frac{N_0}{\pi^{3/2} \prod_i R_i} e^{-\sum_i \frac{i^2}{R_i^2}}. \quad (1.12)$$

The magnetic trap used in Bonn for condensation of ^{87}Rb is characterized by the trapping frequencies $\omega_x = \omega_z = 2\pi \cdot 190 \text{ Hz}$ and $\omega_y = 2\pi \cdot 18 \text{ Hz}$. A typical total atom number after evaporative cooling is about $4 \cdot 10^5$ atoms yielding with equation (1.7) a critical temperature of $T_c \approx 270 \text{ nK}$.

1.2 BEC in weakly interacting gases

In real atomic systems the interaction between atoms cannot be neglected anymore. The interaction in ultracold gases can be described by a single parameter denoted as the s -wave scattering length a . This parameter is introduced in more detail in chapter 2.1. In typical ultracold atom experiments the mean distance $n^{1/3}$ between two particles is much larger than the interaction length. Atomic samples fulfilling the condition $n|a|^3 \ll 1$ are called dilute gases. The interaction of an atom belonging to such a trapped ensemble can therefore be regarded as a two-body process, as processes involving more than two atoms are unlikely due to the diluteness of the gas. Moreover, the details of the molecular potential of the interacting particles are not crucial. Thus the interaction potential can be treated as a pseudo-potential described by a delta function

$$V_{\text{int}}(\vec{r}) = g \delta(\vec{r} - \vec{r}_0). \quad (1.13)$$

The coupling constant

$$g = \frac{4\pi \hbar^2 a}{m} \quad (1.14)$$

characterized by the scattering length considers an effective interaction between one atom and the residual atoms of the sample. Based on this mean field approach explored by N.N. Bogoliubov in 1947 [72], E.P. Gross and L.P. Pitaevskii set up the non-linear Schrödinger equation for a condensate in an external potential $V(\vec{r})$ considering only an effective interaction

$$i \hbar \frac{\partial \phi(\vec{r}, t)}{\partial t} = \left(-\frac{\hbar^2 \nabla^2}{2m} + V(\vec{r}) + g |\phi(\vec{r}, t)|^2 \right) \phi(\vec{r}, t). \quad (1.15)$$

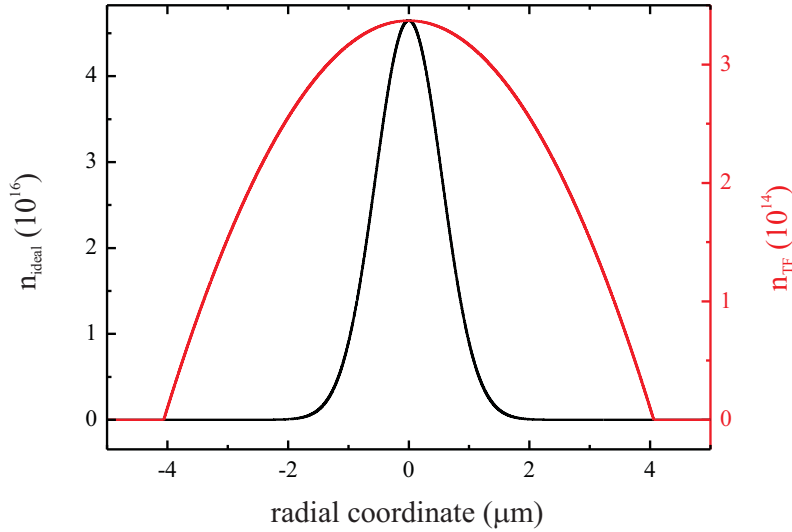


Figure 1.1: Density distribution of a BEC in a harmonic trap. The black line indicates the Gaussian density distribution of a non-interacting BEC, whereas the red line shows the typical parabola of the density distribution for a weakly interacting BEC in the Thomas-Fermi approximation. Both distributions are plotted for our trapping parameters and the Rb triplet s -wave scattering length $a = 99 a_0$, assuming $4 \cdot 10^5$ Rb atoms in the ground state. Note the different scales.

Setting the condensate wave function as $\phi(\vec{r}, t) = \phi(\vec{r}) e^{-\mu t}$ equation (1.15) yields the time-independent Gross-Pitaevskii equation [73, 74, 75]

$$\left(-\frac{\hbar^2 \nabla^2}{2m} + V(\vec{r}) + g |\phi(\vec{r})|^2 \right) \phi(\vec{r}) = \mu \phi(\vec{r}). \quad (1.16)$$

The last term of equation (1.16) is also called mean field energy. The effect of the interaction potential considered in the Gross-Pitaevskii equation depends not only on the strength of the interaction but also on the sign of the scattering length a . For attractive interaction between the atoms ($a < 0$) the density of the BEC increases and three-body recombination becomes dominant due to its cubic dependence on the density. This causes a collapse of the condensate if no counteracting force hinders the increase of the density. BECs with attractive interaction can only exist in inhomogeneous systems with a quantum pressure counteracting the attraction. This was already experimentally investigated for ^{85}Rb by Roberts et al. [29]. Repulsive interaction ($a > 0$) decreases the density in comparison with the ideal gas.

The density distribution of an interacting BEC can be written in the Thomas-Fermi approximation

$$n_{\text{TF}}(\vec{r}) = \frac{\mu}{g} \left(1 - \sum_{i=1}^3 \frac{r_i^2}{R_i^2} \right) \quad (1.17)$$

yielding a parabolic shape. The spatial extent $R_i = 2\mu/m\omega_i^2$ is called Thomas-Fermi radius along the i -th direction. Equation (1.17) is only valid within the range of the Thomas-Fermi radii. The explicit form of the chemical potential for a harmonic oscillator potential can be determined by considering the normalization condition of the condensate wave function and is obtained to be

$$\mu = \left(\frac{15 N a}{\bar{a}_{\text{ho}}} \right)^{2/5} \frac{\hbar \bar{\omega}}{2}. \quad (1.18)$$

Here, $\bar{a}_{\text{ho}} = \sqrt{\hbar/m\bar{\omega}}$ denotes the mean oscillator length. Figure 1.1 shows a cut of the condensate density distribution along the x -axis for an ideal and weakly interacting Rb gas, respectively.

2 Few-body interactions

For the investigation of few-body interactions it is essential to consider the temperature and density of the sample studied. In typical ultracold mixture experiments the temperatures of the atomic clouds are in the range of 10 nK to 10 μ K and their typical mean densities \bar{n} are on the order of $10^{10} - 10^{15} \text{ cm}^{-3}$. The interaction between the atoms for such low temperatures can be described by a single parameter, the scattering length a . This parameter strongly depends on the details of the short range molecular potential. For alkali atoms such as rubidium (Rb), caesium (Cs), and potassium (K) the intra-species scattering length is of the order of $100 a_0$. Therefore, the mean inter-atomic distance $\bar{n}^{-1/3}$ exceeds the interaction length given by a . Despite their low temperatures, the atomic clouds are therefore dilute as $\bar{n} a^3 \ll 1$. Hence, the dynamics of these samples can be described by reducing the complex scattering theory to two-body interactions. Three-body interactions are unlikely and play only a minor role.

2.1 Elastic scattering in the limit of low energies

This two-body process can be reduced to a one-body process by describing the system in the centre-of-mass frame, where $m_{\text{red}} = (m_1 m_2)/(m_1 + m_2)$ is the reduced mass of the two colliding particles. The stationary Schrödinger equation is then given by

$$\left(-\frac{\hbar^2}{2 m_{\text{red}}} \nabla^2 + V(\vec{r}) \right) \Psi(\vec{r}) = E \Psi(\vec{r}), \quad (2.1)$$

where a system of two distinguishable particles is considered. The incoming wave can be treated as a plane wave with wave vector \vec{k} . For a short range potential $V(\vec{r})$ and large distances the outgoing wave can be described by a superposition of a non-scattered part, a plane wave, and the scattered part

$$\lim_{r \rightarrow \infty} \Psi(\vec{r}) \sim e^{i\vec{k} \cdot \vec{r}} + f(k, \Theta) \frac{e^{ikr}}{r}. \quad (2.2)$$

The scattering amplitude $f(k, \Theta)$ depends on the energy via the wave number k and the angle Θ between the axis of detection and the incoming plane wave. In the experiment the differential and total cross-sections $d\sigma/d\Omega$ and σ , respectively, are important observables, both of them given by the scattering amplitude

$$\frac{d\sigma}{d\Omega} = |f(k, \Theta)|^2 \quad (2.3)$$

$$\sigma = \int_{\Omega} |f(k, \Theta)|^2 d\Omega. \quad (2.4)$$

Partial wave expansion

Usually, equation (2.1) cannot be solved analytically. As we will see, in the low energy limit, only collisions of atom pairs with low angular momentum play a significant role. Considering a spherical potential $V(r)$, the total angular momentum has to be conserved during a collision. The solution of the stationary Schrödinger equation may be expanded in terms of spherical harmonics. As the scattering process is independent of the azimuth angle, equation (2.1) can be reduced to a one-dimensional problem

$$\left(-\frac{\hbar^2}{2m_{\text{red}}} \frac{d^2}{dr^2} + V_{\text{eff}}(r) \right) u_l(r) = E u_l(r), \quad (2.5)$$

with the solution

$$\Psi(\vec{r}) = \sum_{l=0}^{\infty} P_l(\cos \Theta) \frac{u_l(r)}{r}. \quad (2.6)$$

Here, $P_l(\cos \Theta)$ are Legendre polynomials and $u_l(r)$ are the partial radial wavefunctions for the angular momentum l . The effective potential

$$V_{\text{eff}}(r) = V(r) + \frac{l(l+1)}{2m_{\text{red}}r^2} \quad (2.7)$$

consists of the spherical potential $V(r)$ and the centrifugal potential depending on the angular momentum. For $l=0$ (s -wave scattering) the effective potential is given by the spherical potential $V(r)$ only. For higher order angular momenta an additional centrifugal barrier is added to the potential. This barrier cannot be passed for low scattering energies, which means the interaction region of small internuclear distance cannot be reached. In ultracold atomic ensembles ($T \lesssim 50 \mu\text{K}$) as used in our experiments, only the s -wave scattering is relevant. For distances larger than the range of the potential, equation (2.6) can be written in the asymptotic form

$$\lim_{r \rightarrow \infty} \Psi(\vec{r}) = \frac{1}{k} \sum_{l=0}^{\infty} P_l(\cos \Theta) A_l \left((-1)^{l+1} \frac{e^{-ikr}}{r} + e^{2i\delta_l(k)} \frac{e^{ikr}}{r} \right). \quad (2.8)$$

Notation (2.2) can be obtained by expanding the plane wave of the spherical harmonics. This yields

$$\begin{aligned} \lim_{r \rightarrow \infty} \Psi(\vec{r}) = \frac{1}{2ik} \sum_{l=0}^{\infty} (2l+1) P_l(\cos \Theta) \left((-1)^{l+1} \frac{e^{-ikr}}{r} + \frac{e^{ikr}}{r} \right) \\ + f(k, \Theta) \frac{e^{ikr}}{r}. \end{aligned} \quad (2.9)$$

Comparing equation (2.8) with (2.9) gives the explicit form for the scattering amplitude

$$f(k, \Theta) = \frac{1}{2ik} \sum_{l=0}^{\infty} (2l+1) P_l(\cos \Theta) (e^{2i\delta_l(k)} - 1). \quad (2.10)$$

For elastic scattering the number of particles must be conserved. As at the same time the angular momentum is conserved, the particle conservation must be satisfied separately for each partial wave. Thus, only a phase shift may occur, whereas the modulus of the amplitude remains constant. Both conditions are fulfilled in the above equation with amplitudes A_l by introducing a phase shift $2\delta_l(k)$ between the incoming and the outgoing wave function. The resulting total cross-section is

$$\sigma_{\text{tot}}(k) = \sum_{l=0}^{\infty} \sigma_l(k) \quad (2.11)$$

$$= \sum_{l=0}^{\infty} \frac{4\pi}{k^2} (2l+1) \sin^2 \delta_l(k). \quad (2.12)$$

The maximum contribution to the total cross-section by each partial wave is given by

$$\sigma_{\text{tot},l}(k) = \frac{4\pi}{k^2} (2l+1), \quad (2.13)$$

which is called the unitarity limit.

Identical particles

In the case of identical particles the total cross section is by a factor of two larger than in the case of distinguishable particles. An exchange of the two particles must yield both a symmetric wave function and a symmetric scattering amplitude for bosons and antisymmetric ones for fermions

$$\frac{d\sigma(k)}{d\omega} = |f(k, \Theta) \pm f(k, \pi - \Theta)|^2. \quad (2.14)$$

Legendre polynomials fulfil $P_l(\cos \Theta) = (-1)^l P_l(\cos \pi - \Theta)$. Hence, only partial waves with even angular momentum contribute to the bosonic cross-section and the partial waves with odd l to the fermionic one

$$\sigma_{\text{tot}}(k) = \frac{8\pi}{k^2} \sum_{l \text{ even}} (2l+1) \sin^2 \delta_l(k) \quad \text{for bosons,} \quad (2.15)$$

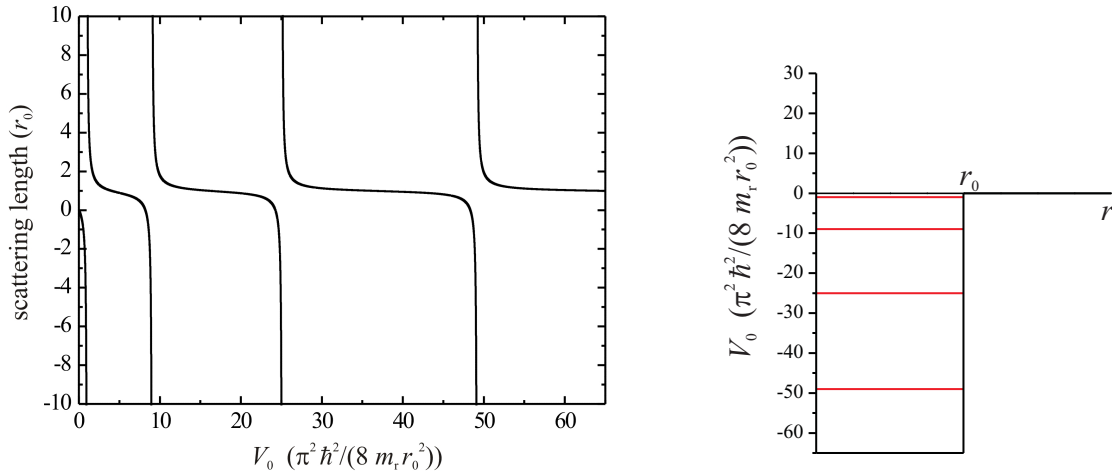
$$\sigma_{\text{tot}}(k) = \frac{8\pi}{k^2} \sum_{l \text{ odd}} (2l+1) \sin^2 \delta_l(k) \quad \text{for fermions.} \quad (2.16)$$

In the limit of low energies where only the s -wave, i.e. the wave corresponding to an angular momentum of $l=0$, has to be taken into account, the total cross-section is given by

$$\sigma_0(k) = \frac{8\pi}{k^2} \sin^2 \delta_0(k). \quad (2.17)$$

In the limit of vanishing k the scattering phase δ_0 vanishes, because $\delta_0 \propto k$, yielding

$$\sigma_0 = 8\pi a^2. \quad (2.18)$$



(a) The scattering length as a function of the potential depth V_0 of a potential well is plotted. The singularities of the scattering length coincide with the appearance of a new bound state. (b) A potential well with a range r_0 supporting four bound states is shown. The red lines indicate bound states.

Figure 2.1: Evolution of the s -wave scattering length for finite potential wells.

Here, the s -wave scattering length a is defined as

$$a = -\lim_{k \rightarrow 0} \frac{\tan \delta_0(k)}{k}. \quad (2.19)$$

For a finite but small collision energy the total cross-section is given by

$$\sigma_0(k) \simeq \frac{8\pi a^2}{(1 - \frac{1}{2} k^2 r_{\text{eff}} a)^2 + k^2 a^2}, \quad (2.20)$$

where r_{eff} denotes the effective range of the given potential.

The s -wave scattering length

Collisions in the s -wave regime can be described and characterized by a single parameter, the scattering length a , without the knowledge about the short-range interaction potential. However, the absolute value and sign, determining the strength and character of the interaction, depend strongly on the short-range potential. The asymptotic wave function in presence of a potential $V(r)$ is shifted by the amount of the scattering length a along the radial axis with respect to the incoming wave. Sign and depth of the potential determine the absolute value of a . The scattering length belonging to a potential barrier, which is a repulsive potential, is always positive corresponding to a repulsive interaction. In the case of a potential well the situation is much more complicated. A potential with a small depth not supporting a bound state yields a negative scattering length and thus an attractive interaction. If the potential depth increases until the

	Rb [76]	Cs [77]	K [78]	Rb-Cs [79]	K-Rb [80]
a_t (a_0)	99.0	2400	60.54	≥ 150	-213.6
a_s (a_0)	90.4	280	85.53	unknown	-109.6

Table 2.1: Intra- and interspecies singlet- and triplet scattering lengths for the isotopes ^{87}Rb , ^{133}Cs and ^{41}K and the mixtures ^{87}Rb - ^{133}Cs and ^{41}K - ^{87}Rb .

first bound state coincides with the dissociation energy, the scattering length diverges. Further increase of the potential depth leads to a positive scattering length resulting in an effective repulsive interaction, although the potential is attractive. This trend is repeated periodically for each additional bound state supported by the potential. The scattering length in the special case of a potential well with a finite potential depth V_0 is plotted in figure 2.1(a). Each singularity corresponds to the appearance of a new bound state in figure 2.1(b). This behaviour of the scattering length is analogous to the Feshbach resonance phenomenon described in section 2.3. The intra- and inter-species scattering lengths of the magnetic field free triplet (a_t) and singlet potential (a_s) for the bosonic species ^{87}Rb , ^{133}Cs and ^{41}K and the mixtures¹ ^{87}Rb - ^{133}Cs and ^{41}K - ^{87}Rb are listed in table 2.1.

2.2 Molecular potentials of alkali atoms

The complexity of the molecular interaction potentials does not allow ab initio predictions on the s -wave scattering length. Alkali atoms such as Rb, Cs and K, which are used in our two experiments, own only one valence electron. But even for this comparatively simple system of alkalis the accurate determination of the corresponding molecular potentials requires experimental data, e.g. the observation of Feshbach resonances, as an input for theoretical models. In this section the contributions to this molecular potential are discussed considering internal degrees of freedom.

Hyperfine interaction

All alkali atoms in the electronic ground state have one valence electron with spin \vec{s} and its projection $s = 1/2$. The nuclear spin \vec{i} depends on the atomic species. For the species used within this thesis the projections of the nuclear spins are $i = 3/2$ for the ground state $5S_{1/2}$ of ^{87}Rb , $i = 3/2$ for the $4S_{1/2}$ -state of ^{41}K and $i = 7/2$ for the $6S_{1/2}$ -state of ^{133}Cs . In the absence of any external field, the hyperfine interaction occurring due to the induced magnetic field from the valence electron at the position of the nucleus, couples the electron and nuclear spin to the total spin $\vec{f} = \vec{s} + \vec{i}$ for each single atom

¹In this thesis the following notation is used: Atomic mixtures and heteronuclear molecules are denoted with A-B and AB, respectively, where A and B are the participating atoms.

2 Few-body interactions

in the ground state. In the case of alkalis the projected quantum number f is given by $f = i \pm 1/2$. This coupling is the origin of the hyperfine splitting. For the ground states of the abovementioned species the hyperfine splittings ΔE_{hf} are $h \cdot 6.8$ GHz for ^{87}Rb , $h \cdot 9.6$ GHz for ^{133}Cs and $h \cdot 254$ MHz for ^{41}K . The hyperfine structures of the D2 line for the isotopes ^{87}Rb , ^{133}Cs and ^{41}K are shown in Appendix A.

Zeeman interaction

By applying an external magnetic field, the hyperfine states are further split into magnetic substates m_f , as the magnetic moment μ of the atom induced by the nuclear and electron spins interacts with the magnetic field. Depending on the strength of the magnetic field, different coupling regimes have to be distinguished. In the limit of small magnetic fields (m_f -splitting \ll hyperfine splitting) the total spin $\vec{f} = \vec{s} + \vec{i}$ interacts with the magnetic field and the interaction potential is given by

$$V_Z = -\vec{\mu} \cdot \vec{B} \quad (2.21)$$

$$= g_f m_f \mu_B |\vec{B}|. \quad (2.22)$$

This anomalous Zeeman effect generates a m_f state depending energy shift and removes the degeneracy of the m_f states. Regarding the species used in our experiments, equation (2.21) is valid for magnetic fields of $B \ll 2400$ G for Rb, $B \ll 90$ G for K and $B \ll 3300$ G for Cs. For large magnetic fields which induce a Zeeman splitting of the order of the hyperfine splitting, the separate interaction of the electron and nuclear spin with the magnetic field dominates the hyperfine splitting. That means f is not a good quantum number anymore. The energy shift in this region is described by the Paschen-Back effect. The region in-between is more complicated. For alkalis the Zeeman shift of the magnetic substates is well described by the Breit-Rabi formula² [81]

$$E = \frac{\Delta E_{\text{hf}}}{2(2i+1)} \pm \frac{\Delta E_{\text{hf}}}{2} \sqrt{1 + \frac{4(m_i \pm 1/2)x}{2i+1} + x^2}, \quad (2.23)$$

with $x = g_J \mu_B B / \Delta E_{\text{hf}}$. For typical magnetic fields used in our experiments equation (2.21) is valid for Rb and Cs. However, for K at a field of 100 G, the deviation is already 30%, hence the Breit-Rabi formula has to be applied. The Zeeman energy shifts of the magnetic substates are $m_f \cdot 0.7$ MHz/G for ^{87}Rb and ^{41}K and $m_f \cdot 0.35$ MHz/G for ^{133}Cs .

Molecular potential

So far only interactions of the internal degrees of freedom within one atom with external fields have been considered. For the interaction of two colliding atoms their molecular potential has to be examined. A typical molecular potential as a function of the distance

²Within this section i denotes the projection of the nuclear spin.

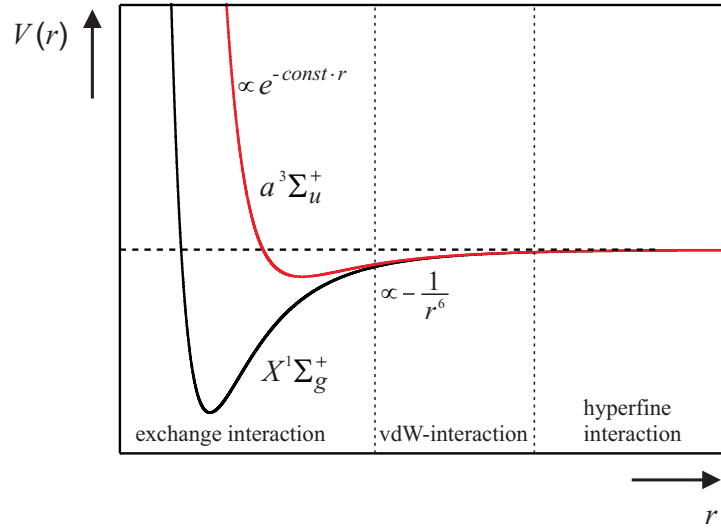


Figure 2.2: Qualitative form of a typical molecular potential for the triplet state $a^3\Sigma_u^+$ (red solid line) and the singlet state $X^1\Sigma_g^+$ (black solid line): The horizontal dashed line indicates the dissociation threshold. The vertical dashed lines divide the molecular potential into parts of different dominating interaction processes.

between two colliding atoms is qualitatively shown in figure 2.2. For different distances, different interaction mechanisms dominate in the potential

$$V = V_{\text{HF}} + V_Z + V_C + V_{\text{SS}} + V_{\text{SO}}. \quad (2.24)$$

Equation (2.24) is valid within the Born-Oppenheim approximation, in which the density distribution of the electron cloud is assumed to be given by the internuclear distance, as the light electrons instantaneously follow the motion of the heavy nucleus. The first two contributions, the hyperfine (V_{HF}) and Zeeman (V_Z) potentials, have already been discussed above.

Coulomb and spin exchange interaction

The third term, the Coulomb interaction V_C , dominates the typical shape of the molecular potential. In the limit of a vanishing atomic separation the Coulomb repulsion of the nuclei is responsible for the steep slope of the repulsive potential. If nuclear distances of the colliding atoms are larger than their mean atomic diameter, quantum fluctuations of the charge distribution yield the dispersive multipole interaction

$$V_{\text{disp}} = -\frac{C_6}{r^6} - \frac{C_8}{r^8} - \frac{C_{10}}{r^{10}}. \quad (2.25)$$

It is dominated by the van-der-Waals interaction $-C_6/r^6$ where the van-der-Waals coefficient depends on the particular atomic species. For K-Rb the van-der-Waals coefficient

2 Few-body interactions

C_6 has been determined to be $4238 E_h a_0$ [80]. The range of the van-der-Waals interaction is described by the van-der-Waals length $l_{\text{vdW}} = 0.5 (m C_6 / \hbar^2)^{1/4}$, where m denotes the atomic mass. In between these two regimes the two electron spins couple to the total spin $\vec{S} = \vec{s}_1 + \vec{s}_2$ due to the overlapping electron clouds³. The spin-exchange interaction underlies this spin coupling and leads to a potential which scales as

$$V_{\text{ex}} \propto e^{-\frac{r}{r_0}}. \quad (2.26)$$

This spin coupling splits the molecular potential into a singlet ($S = 0$) and triplet ($S = 1$) potential denoted by $a^3\Sigma_u^+$ and $X^1\Sigma_g^+$. The singlet potential is always deeper than the triplet. For small particle separation the total spins S and I are good quantum numbers, however, for large distances the interaction strength within the atom exceeds the inter-atomic interaction. Hence, for a large separation f_1 and f_2 are good quantum numbers.

Dipolar Relaxation: Magnetic dipole and second-order spin-orbit interaction

The interaction between the magnetic moments of the electrons $\vec{\mu}_1 \propto \vec{s}_1$ and $\vec{\mu}_2 \propto \vec{s}_2$ causes the spin-spin interaction V_{ss}

$$V_{\text{ss}} \propto \frac{\vec{s}_1 \cdot \vec{s}_2 - 3(\vec{s}_1 \cdot \vec{e}_{12})(\vec{s}_2 \cdot \vec{e}_{12})}{r^3}. \quad (2.27)$$

This long-range dipole-dipole interaction, which is proportional to $1/r^3$, is not spherical symmetric, hence the orbital angular momentum is not conserved anymore. Spin changes are allowed, where the selection rules for these dipolar collisions are $\Delta l = 0, \pm 2$ and $\Delta m_l + \Delta m_F = 0$. This corresponds to a redistribution of angular momentum. Also the latter contribution to equation (2.24) allows the exchange of spin and orbital angular momentum. The short range second order spin-orbit-potential V_{SO} arises when the electron clouds of the colliding atoms overlap [82]. The coupling of the ground state spins is induced via excited electronic states. The signs of the two potential contributions V_{SS} and V_{SO} are opposite. Their range differs strongly, but their selection rules are identical due to the same tensor structure.

Three-body recombination

In two-body collisions the formation of a molecule is forbidden due to momentum and energy conservation. A third atom is necessary to simultaneously fulfil both conditions. The released binding energy is shared between the molecule and the atom according to the mass ratio. The three-body recombination rate depends strongly on the s -wave

³Throughout this thesis properties of single atoms are denoted by lower case letters, whereas the properties of two coupled atoms are specified by capital letters.

scattering length and is predicted to scale with a^4 [83] in the limit of large a and ultralow collision energies

$$K_3 = \frac{3C\hbar a^4}{m}, \quad (2.28)$$

which was verified by several experimental observations [84, 85]. The dimensionless factor C is predicted to be between 0 and 70 [83, 86, 87]. As three-body recombination is the dominating process of atom loss in the vicinity of a Feshbach resonance, it is treated in more detail in section 2.3.5, when loss mechanisms are discussed.

2.3 Feshbach resonances and molecules

Considering two molecular potentials belonging to two different internal states of colliding atoms, a so called Feshbach resonance [88] can occur, if a non vanishing coupling between the different states exist. These resonances appear if the energy of a molecular bound state of the higher energetic molecular potential (closed state in figure 2.3) coincides with the energy of two colliding atoms in a scattering state which is, in figure 2.3, denoted as the entrance channel. At the position of the Feshbach resonance the s -wave scattering length diverges. Magnetic Feshbach resonances are of broad interest in physics of ultracold gases: The scattering length can be tuned in a controlled way over several orders of magnitude and even a change of the sign of the scattering length is possible by applying an external homogeneous magnetic field. They are not only used to tune the interaction between atoms of a single species or a mixture, but also as a tool for the association of weakly bound molecules as a first step towards deeply bound molecules in the rovibrational ground state, e.g. to create a molecular BEC. In addition, Feshbach resonances give an important input in order to improve the detailed description of molecular potentials. The theoretical model for a molecular potential is based on adjusting the coefficients of all terms contributing to the potential, so that the data, taken by photoassociation [89, 90] or Feshbach spectroscopy, are reproduced as well as possible. Another application is the probing of Efimov resonances which are also of broad interest for nuclear physicists [91]. These resonances thus offer a broad range of new research directions.

2.3.1 Feshbach resonance

The Feshbach resonance phenomenon is explained by means of figure 2.3 showing two molecular potentials corresponding to two different spin configurations of the colliding atom pair. The energetically lower molecular potential is called entrance channel, as we assume two asymptotically free atoms above the dissociation energy of this state to scatter. Within this chapter the nomenclature of this kind of systems is as follows: Molecular potentials, for which the dissociation energy is above the total energy of the system of the scattering atoms are called "closed channels". A molecular potential with

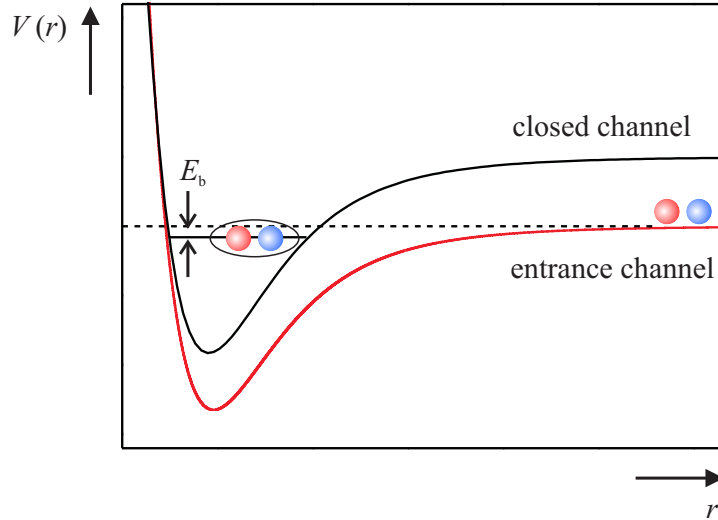


Figure 2.3: Schematic of the Feshbach resonance showing two molecular potentials corresponding to different internal states of two colliding atoms. The red solid line indicates the entrance channel. The black solid line shows the closed channel with one bound state below the dissociation threshold of the entrance channel (dashed horizontal line). The binding energy is denoted by E_b .

a dissociation threshold below the total energy is denoted as an "open channel" including the entrance channel.

To make it simple, we consider now a system composed of the entrance channel and only one closed channel. Assuming that the closed channel contains a bound state close to the dissociation threshold of the entrance channel and the coupling between the bound state and the scattering state does not vanish, the bound state can be occupied temporarily by the scattering atoms. This molecular state is not stable, as a coupling to the scattering state exists. Hence, this kind of metastable molecular state is called a quasi-bound state. If the energy of the free atoms coincides with the energy of this quasi-bound state, the occupation of this state is resonantly enhanced. The s -wave scattering length diverges. As in the well known case of an infinitely deep potential well, the sign of the scattering length depends on the position of the bound state with respect to the scattering state. For bound states above the scattering state the scattering length is negative and the energy of the bound state lies within the scattering continuum of the entrance channel. In the other case, when the molecular state is below the scattering state, the scattering length is positive.

Experimentally this behaviour is of interest if the scattering length can be adjusted controlledly by shifting the energies of the bound and the scattering state with respect to each other. Considering internal degrees of freedom as the spin configuration of atomic systems, the two molecular potentials belong to different spin systems. This results, in general, in different magnetic moments for the different potentials. By applying an

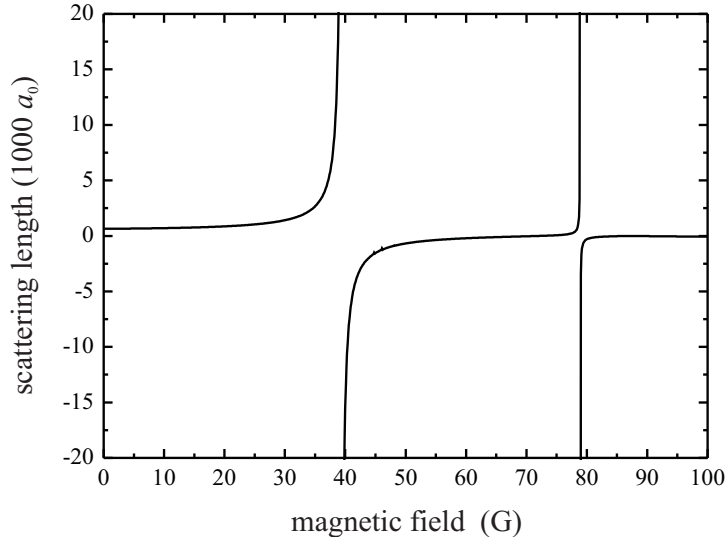


Figure 2.4: Two theoretically predicted s -wave Feshbach resonances of K-Rb in the absolute ground states at a magnetic field of 39 G and 79 G [92].

external homogeneous magnetic field the energy may be shifted due to the Zeeman effect. If the magnetic moments of the scattering and the molecular potentials differ because of their different spin configuration, the energy difference between the scattering and the bound state can be changed and thus the scattering length can be tuned continuously from minus to plus infinity. In the vicinity of a Feshbach resonance the scattering length a behaves as [93]

$$a = a_{\text{bg}} \left(1 - \frac{\Delta B}{B - B_0} \right). \quad (2.29)$$

The width of the resonance ΔB is determined by the distance of the zero crossing of the scattering length to the resonance position B_0 . It is inversely proportional to the magnetic moments and proportional to the squared matrix element describing the coupling strength of both states. The background scattering length a_{bg} is given by the scattering length far off resonance. For the system $^{41}\text{K} - ^{87}\text{Rb}$, both species in the absolute ground state $|1, 1\rangle$, two s -wave Feshbach resonances occur below 100 G, shown in figure (2.4). The corresponding background scattering length is $a_{\text{bg}} = 284 a_0$, where a_0 is the Bohr radius [92].

2.3.2 Classification and selection rules

The participating channels can be classified using different denotations. The entrance channel is described by the quantum numbers $|f_1, m_{f_1}, f_2, m_{f_2}, l, m_l\rangle$ of asymptotically free atoms with a rotational quantum momentum l within a small magnetic field, in

which f_i is a good quantum number. As we are regarding heteronuclear Feshbach resonances, no restrictions on the orbital quantum number l due to a (anti-) symmetry of the wave functions have to be considered. In general the situation changes for a molecular state as the short range potential becomes significant here. Therefore, the separated spin quantum numbers S and I are good quantum numbers. As discussed in more detail later on, Feshbach molecules are extremely weakly bound as Halo dimers. Hence, their huge spatial extent allows to characterize the molecular channel as well as the entrance channel with the separated quantum numbers of asymptotically free atoms according to the molecular potential. The spins \vec{f}_i of the separated atoms couple to \vec{F} . The molecular state can hence be described by the projected quantum numbers $|F, m_F, l, m_l\rangle$. The coupling between the entrance and the closed channel occurs mainly due to the spin exchange interaction, the relativistic magnetic dipole interaction, and the spin-orbit interaction. The specified coupling mechanisms yield different selection rules. In the case of spin exchange collisions no coupling between different partial waves occurs. Hence, the angular momentum l and its projection m_l , as well as the projection of the total angular momentum, are conserved. Therefore, the rotational quantum number must not change via the coupling of the entrance and the closed channel. Thus, for ultracold atomic ensembles the rotational quantum number of the bound state has to be $l=0$. These Feshbach resonances are called s -wave resonances. This coupling mechanism is usually the origin of broad resonances. The much weaker spin-orbit and magnetic dipole interactions cause the more narrow resonances. Here, a redistribution of the angular momenta can take place, hence l is not conserved and the selection rules are given by $\Delta l = 0, \pm 2$ and $\Delta m_l + \Delta m_F = 0$. The two Feshbach resonances of the bosonic K-Rb mixture shown in figure 2.4 are characterized as s -wave Feshbach resonances, where the bound states are attributed to states with the quantum numbers $|2, 2, 0, 0\rangle$ and $|3, 2, 0, 0\rangle$, respectively.

2.3.3 Universality

A remarkable property of Feshbach molecules is their universal behaviour. Universal means in this context, that their properties only depend on the s -wave scattering length and are independent of the details of their microscopic molecular potential [94]. However, the scattering length itself depends strongly on the short range potential. The highly excited and weakly bound molecular states close to the dissociation threshold of the entrance channel are characterized by a large spatial extent exceeding the classical turning point r_{class} . The latter one can be deduced by the van-der-Waals interaction ($\propto C_6/r^6$) to be $r_{\text{class}} = (a(2l_{\text{vdW}})^2)^{1/3}$. The scattering length in this regime is much larger than the van der Waals length l_{vdW} , which is $72 a_0$ for the K-Rb molecular potential. Therefore, the interaction is dominated by the s -wave scattering length in the case of ultracold ensembles. The universal binding energy of the weakly bound molecules is given by

$$E_b = -\frac{\hbar^2}{m a^2}. \quad (2.30)$$

The wave function of the bound state within the universal regime can be described as a spherical wave

$$\phi(r) = \frac{1}{\sqrt{2\pi a}} \frac{e^{-r/a}}{r} \quad (2.31)$$

only depending on the scattering length irrespective of the details of the short range potential. Hence, the mean distance of the atoms forming the molecule is $a/2$. Feshbach molecules are a special case of Halo dimers. The particular properties of these weakly bound molecules are also valid for other diatomic Halo systems, such as the He-dimer or the deuteron.

2.3.4 Theoretical approaches

To predict the resonance position theoretically, the details of the molecular potentials, in particular the Born-Oppenheimer potentials as well as the van-der-Waals coefficient of the participating atomic species, have to be precisely known. For an exact quantum mechanical description of the Feshbach phenomena all closed and open channels and their coupling among each other have to be included in the calculations. All theoretical calculations are based on experimental data. References [93, 95] showed that a simplified coupled channel approach considering two channels only, i.e. the entrance channel and one closed channel, describes most of the measured data quite well. Due to the usually strong coupling between the scattering state and the near threshold molecular state, a further simplification is possible in which only one molecular state in the vicinity of the dissociation threshold of the entrance channel is considered. For scattering lengths within the universal regime the spatial extent of the dimer exceeds the classical turning point as described in section 2.3.3. Hence, the closed channel admixture to the wave function of the bound state becomes negligible and vanishes on resonance [96]. Therefore, the exact properties of the resonance state need not necessarily be known to set up the wave function of the dimer, but it is rather given by the entrance channel confirming the validity of equation (2.31). Within the universal regime the resonance behaviour can be treated in a single channel approach and a contact potential can be assumed. Outside the universal regime the contribution of the admixture of the closed channel to the dimer wave function is not negligible and the binding energy becomes proportional to $(B - B_0)$. Hence, resonances can be classified to entrance ($\eta \ll 1$) and closed channel ($\eta \gg 1$) dominated resonances, where [97, 98]

$$\eta = \frac{\bar{a}}{a_{\text{bg}}} \frac{\hbar^2}{\mu_{\text{res}} \Delta B m \bar{a}^2}. \quad (2.32)$$

Here, $\bar{a} \approx 0.96 l_{\text{vdW}}$ is the mean scattering length according to Gribakin and Flambaum [99] and $\mu_{\text{res}} = \partial E / \partial B$ denotes the difference in the magnetic moment of the bound and the scattering state. The entrance channel dominated resonance, in which the admixture of the closed channels is small, is in general characterized by a large universal

regime and usually results in broad resonances. These resonances are often predestinated for investigation of Efimov resonances [91], because an easily accessible universal regime is required to prove the remarkable universal behaviour of these trimer states. In addition, broad resonances give the opportunity to control and adjust the scattering length precisely over several order of magnitudes from 0 up to several $10^4 a_0$. The closed channel dominated resonances are in general narrow leading to worse accessibility of the universal regime. The range of the universal regime for a given resonance is given by [100]:

$$\left| \frac{B - B_0}{\Delta B} \right| \ll \frac{\mu_{\text{res}} \Delta B}{2 \hbar^2 / (m a_{\text{bg}}^2)}. \quad (2.33)$$

The numerator $\mu_{\text{res}} \Delta B$ yields the information on the coupling strength. Values much larger than unity imply strong coupling and vice versa. The width of the Feshbach resonance depends on the coupling mechanism. The Coulomb interaction leads to a strong coupling and broad resonances. On the contrary dipole-dipole interactions, which are comparably weak, cause narrow resonances. In addition the background scattering length a_{bg} affects the range of the universal regime.

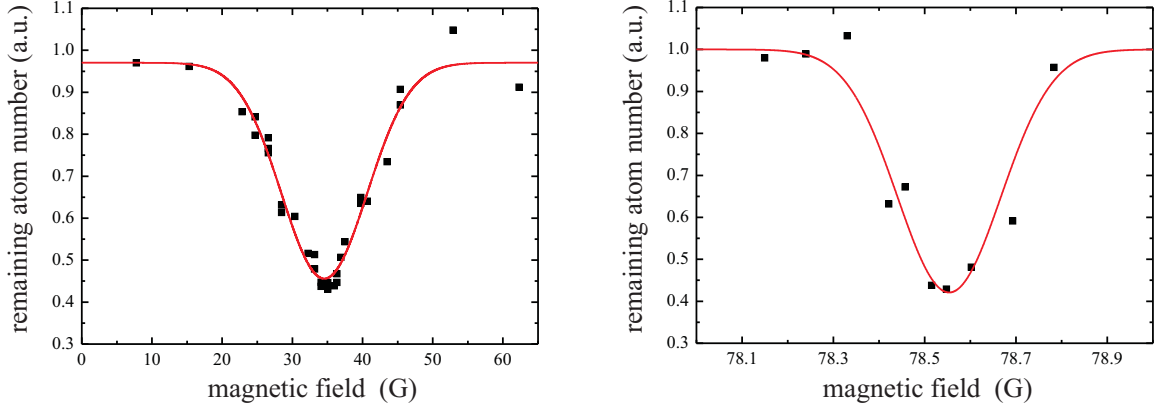
2.3.5 Loss mechanisms

Besides the elastic scattering properties the inelastic scattering processes also change dramatically in the vicinity of a Feshbach resonance. Most of the real atomic systems consist of more than one open and the closed channel. The existence of these additional channels leads to two- and three-body losses.

Two-body losses

Two-body losses occur if the populated molecular state couples to an open channel other than the entrance channel. The origin of these two-body losses are spin exchange processes ($\Delta m_F = 0$) and dipolar relaxation ($\Delta m_F + \Delta m_l = 0$) as explained in section 2.2. The atoms gain the potential difference between the entrance and the final state as kinetic energy. The amount of kinetic energy gained is of the order of the Zeeman or hyperfine splitting depending on the final state. In the case of Rb and K, the Zeeman splitting is 0.7 MHz/G and the hyperfine splitting of the ground states $h \cdot 6.8$ GHz and $h \cdot 254$ MHz, respectively. For a trap depth of several $k_B \cdot 10 \mu\text{K}$ corresponding to $h \cdot 300$ kHz, these inelastic processes results in trap losses. In the special case of magnetic traps additional losses occur if atoms in the final state cannot be trapped magnetically. Trap losses due to spin exchange interaction are forbidden for doubly polarized states ($|f = 2, m_f = \pm 2\rangle$ for Rb and K) due to the selection rule $\Delta m_F = 0$ and suppressed for maximal elongated states ($|f = 1, m_f = \pm 1\rangle$ for Rb and K), as in the low energy limit a transfer to the higher energy hyperfine state is not possible.

Dipolar relaxation includes interactions due to the exchange of spin and angular momentum, which are called dipole-dipole-interaction and spin-orbit-interaction (section



(a) Atom losses due to the Feshbach resonance: The Gaussian fit yields a Feshbach position of 37.2(2) G. The width of the broad resonance is determined to be 34 G.

(b) Atom losses due to the Feshbach resonance: The Gaussian fit yields a Feshbach position of 78.57(2) G. The width of this more narrow resonance is determined to be 1.2 G.

Figure 2.5: Enhanced three-body recombination losses at the position of two interspecies *s*-wave Feshbach resonances of ^{41}K - ^{87}Rb each in the ground state $|f = 1, m_f = 1\rangle$.

2.2). The selection rules for both of these processes are $\Delta m_F + \Delta m_l = 0$ and $l = 0, \pm 2$. The coupling strengths for these processes are usually much weaker than for spin exchange interactions. For atoms initially prepared in the energetically lowest Zeeman state ($|f = 1, m_f = 1\rangle$ for Rb and K) no further open channel exist, which excludes inelastic two-body collisions via a weakly bound molecular state. In contrast, for the energetically highest Zeeman state ($|f = 2, m_f = 2\rangle$ for Rb and K) no Feshbach resonance occurs as there is no near-threshold molecular state belonging to a closed channel.

Three-body losses

In addition to the two-body losses also three-body losses occur. In the vicinity of the Feshbach resonance the three-body loss rate is strongly enhanced due to its a^4 scaling. For large scattering lengths two interacting atoms can form a deeply bound molecule, while a third atom carries away the released binding energy for a simultaneous conservation of momentum and energy. During this three-body recombination the binding energy of the produced molecule is converted to kinetic energy and split up according to the mass ratio of the molecule and the third atom to $m_{\text{molecule}}/(m_{\text{molecule}} + m_{\text{atom}})$ to the atom and to $m_{\text{atom}}/(m_{\text{molecule}} + m_{\text{atom}})$ to the molecule. Typical binding energies of several hundred MHz result in heating of the ensemble and also in trap loss of the molecule and the third atom. Furthermore, for positive scattering lengths three-body recombination populating the weakly bound molecular state can occur. By collisions with unpaired atoms these shallow dimers decay into deeply bound dimers releasing the difference in binding energy of the two molecular states. Hence, Feshbach resonances can be detected via strongly enhanced atom loss from the trap, due to resonantly enhanced

2 *Few-body interactions*

inelastic three-body collisions. Figure 2.5 shows two typical loss measurements in the vicinity of the s -wave Feshbach resonances of the bosonic K-Rb mixture at about 37 G and 79 G. The Feshbach resonance position is determined by the centre of the loss peaks. In chapter 5 a more detailed discussion on these resonances is presented.

3 Towards an ultracold mixture

Ultracold atomic gases form a highly controllable environment to study many-body interactions. A well defined initial quantum state can be experimentally realized by producing a BEC. The phase transition from a thermal gas to a BEC occurs when the phase space density reaches a value of $\lambda_{\text{dB}}^3 n \approx 2.6$. For typical systems, compatible densities would correspond to a liquid or solid phase. In order to avoid a phase transition to a liquid or solid, the gas has to be very dilute. Usually the atomic densities are of the order of 10^{15} cm^{-3} , several orders of magnitude lower than in liquids or solids. In this regime, two-body collisions dominate, as the probability for three-body collisions leading to molecule formation scales as n^3 . In order to still increase phase space density, the temperature has to be lowered from room temperature to about 100 nK, thereby increasing the deBroglie wavelength of the atoms to be of the order of the typical inter-atomic distance.

For the investigation of inter-species interactions a well defined initial state of two atomic species is required. In our experiments we produce ultracold Rb-Cs and K-Rb mixtures, respectively. As the typical experimental steps are similar for both approaches, I will explain the detailed experimental setup and sequence using the Rb-Cs experiment. For the K-Rb experiment, minor differences will be mentioned, if necessary, in Chapter 5.

3.1 Vacuum system

The heart of the experiment is a vacuum system, in which atoms are cooled, trapped, and manipulated by means of optical and magnetic fields. The vacuum serves as an isolation from the environment to prevent collisions with hot (room temperature) background gas particles. The Rb-Cs setup in Bonn features a double magneto-optical trap system (double MOT), with the two MOTs operating in different background pressure regimes. The first MOT is designed to cool and trap a large number of atoms from a relatively large Rb partial pressure of 10^{-9} mbar, originating from a Rb vapour cell. The second MOT is running in a high quality glass cell with ultra-high vacuum. Here, a pressure of 10^{-11} mbar maximizes the lifetime of the cold atomic sample by minimizing the number of background gas collisions. In this region eventually the BEC is produced. Both pressure regimes are connected by a differential pumping tube with a diameter of 3 mm and a length of 8 mm. A near resonant laser beam is used to push atoms from the upper MOT through the differential pumping stage into the second MOT.

The pumping system maintaining the ultra-high vacuum consists of an Ion getter pump

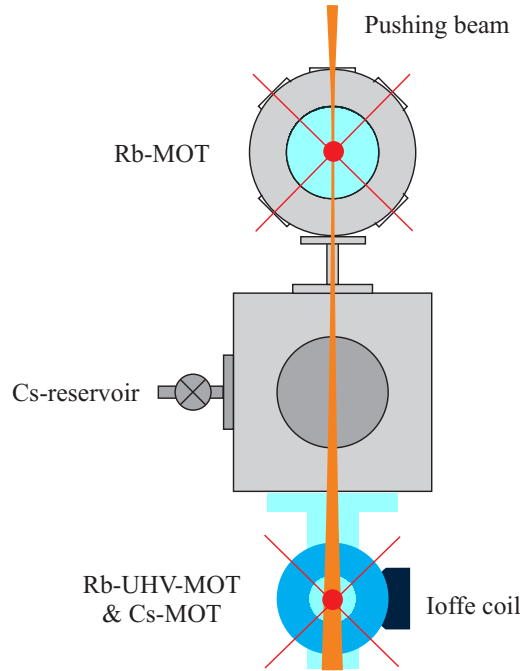


Figure 3.1: Double-MOT system: Rb atoms are loaded first in the upper vapour pressure MOT. A pushing beam (orange) transfers the precooled atoms towards the UHV-MOT in the glass cell (light blue). The Cs reservoir is attached at the UHV-part of the vacuum system. The blue toroid and the red solid lines indicate one of the quadrupole coils and the MOT beams, respectively.

with a pump speed of 230 l/s and an additional Ti-sublimation pump including a cryo-panel that can be cooled by liquid nitrogen and increases the pumping rate for hydrogen, oxygen, and water. This system replaced a turbomolecular pump with magnetic rotor suspension, which spectacularly broke down during operation. The newly constructed vacuum system has several advantages: It forms a completely closed system without any direct connection to the atmosphere and is therefore less accident-sensitive. Finally it is free from acoustic vibrations. An uninterruptible power supply protects the system against power failures to avoid a shutdown of the ion getter pump. In contrast to the previous setup the ion pump produces strong magnetic field gradients and stray fields. Therefore, the distance between the ion getter pump and the atomic sample must be sufficiently large. A large distance between pump and glass cell, however, reduces the effective pumping rate at the position of the atoms. We chose a distance of 100 cm, as a compromise between a relatively small maximum magnetic field gradient of 2 mG/cm at the position of the glass cell and an effective pumping rate of 184 l/s at the position of the turbomolecular pump¹ previously used. The residual gradient is not expected to have a noteworthy effect on the experimental sequence. In particular, it is of the same order of magnitude as typical ambient magnetic field fluctuations. An additional

¹The pumping rate of this turbomolecular pump was 180 l/s.

magnetic field shielding of μ -metal or other materials with a high permeability are thus not required.

In order to not spoil the vacuum of the main chamber including the glass cell, the new pumping section was installed and baked while a linear valve sealed the main chamber against atmosphere pressure. After establishing ultra-high vacuum in the pumping section, the valve was opened, resulting in a disappointing large final pressure of 10^{-10} mbar. In order to avoid baking out the whole chamber, which would have implied removing the existing optical setup and coil system, we cooled the cryopanel with liquid nitrogen, while the valve was open. Thus residual contaminations froze out at the walls of the cryopanel, effectively reducing the pressure in the main chamber. After closing the valve, a large fraction of the contaminations was contained in the pumping section and removed by subsequent bake out. Repeating this procedure several times, a final pressure of $1.2 \cdot 10^{-11}$ mbar was achieved.

As we aim for working with a few or single Cs atoms, only a low partial background pressure is necessary to load a Cs MOT from the background pressure, as will be explained in chapter 4. Therefore, the Cs vapour cell is directly attached to the UHV region without differential pumping stage. Most of the time this reservoir is closed by a valve, ensuring the required background pressure of 10^{-11} mbar.

3.2 Laser system for trapping and detection

The atom traps mentioned in the previous section require near-resonant laser light to drive a closed atomic transition. Such transitions exist for alkali atoms on the $S_{\frac{1}{2}} \rightarrow P_{\frac{3}{2}}$ transitions, i.e. on the D2 lines. For Rb and Cs these transitions at wavelengths of 780 nm and 852 nm, respectively, can be addressed by diode lasers. The hyperfine structure of the D2 line of both species is depicted in Appendix A. In both cases, the transition between the upper most hyperfine states of the ground and excited states are cycling transitions ($f = 2 \rightarrow f' = 3$ for ^{87}Rb and $f = 4 \rightarrow f' = 5$ for ^{133}Cs). Nevertheless, one out of every 10000 scattered photons excites the atom to the $f' = 2$ -state ($f' = 4$ -state) from where it can decay into the $f = 1$ -state ($f = 3$ -state). Thus it decouples from the cycling transition. A second laser (called repumping laser) tuned to the $f = 1 \rightarrow f' = 2$ ($f = 3 \rightarrow f' = 4$) transition is therefore necessary to transfer these atoms back to the cycling transition. In addition, laser light is needed for spin polarization (optical pumping), to probe the atoms by absorption imaging, and to transfer them from the vapour cell MOT to the UHV-MOT by radiation pressure. All lasers have to be frequency stabilized within the linewidth of the transition driven. During different stages of the experimental cycle, the detuning of the cooling laser light has to be varied by up to 70 MHz.

Cs laser system

In 2006, the experimental setup was moved to a new laboratory, and the Cs laser system had to be re-built. The frequency stabilization scheme of the old setup employed the

3 Towards an ultracold mixture

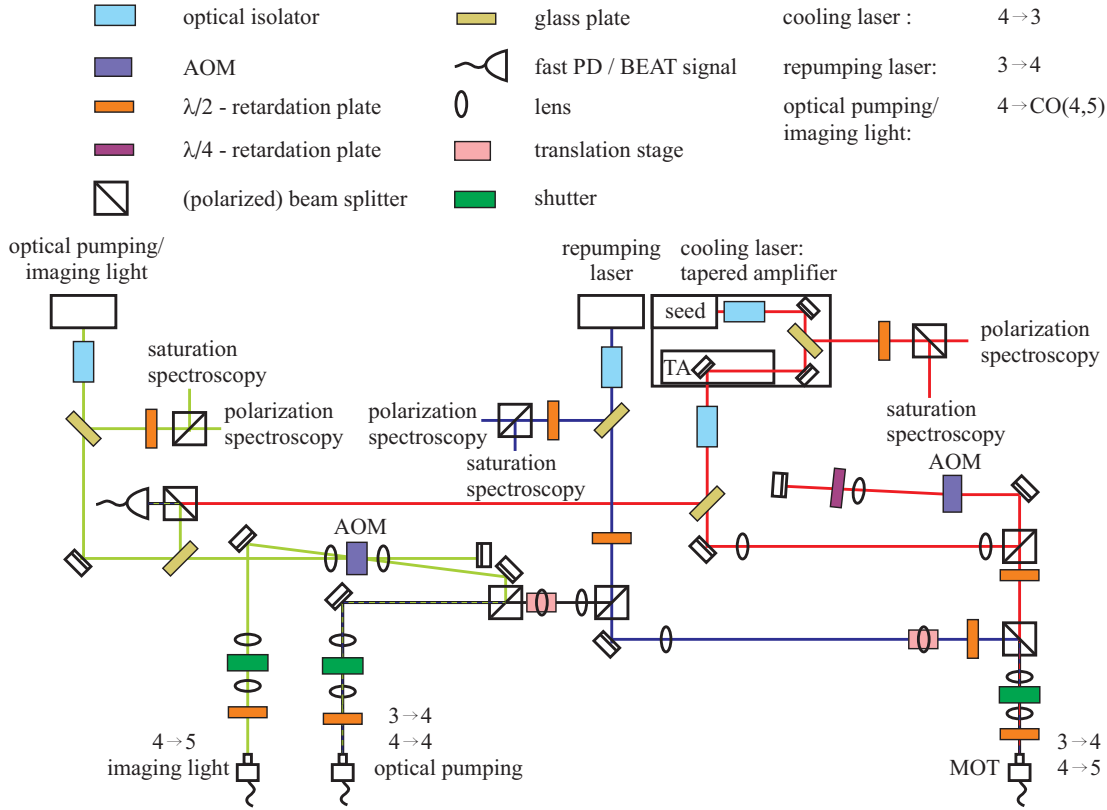


Figure 3.2: New setup of the Cs laser system: Three lasers (optical pump-
ing/probing laser, repumping laser, TA) provide the light for the MOT, the optical
pumping and the imaging. The red, green, and blue solid lines indicate the laser beam
path of the TA, repumping laser, and optical pumping/probing laser, respectively.

dichroic-atomic-vapor laser lock (DAVLL) [101]. The frequency of the laser light was changed by adjusting the external grating of the Littrow-type diode lasers used. For such mechanical processes, the bandwidth is of the order kHz, which is too low for some applications. In addition, the DAVLL-scheme is based on Doppler broadened spectroscopy and therefore not as precise as subdoppler spectroscopies. Moreover, it is very sensitive to even small changes of the polarization [102] and thus exhibits relatively large drifts in frequency. In particular correlations with changes of the room temperature could be observed. Therefore, the re-built laser system is based on a polarization spectroscopy [103] which does not suffer from the aforementioned drifts. A schematic of the new setup is shown in figure 3.2. The laser systems and the associated spectroscopies have been designed to fulfil certain requirements.

First of all, sufficiently high laser power at the experiment is needed. In practice this amounts to about 50 mW for the cooling laser. In addition, frequency fluctuations of the laser must be smaller than the linewidth of the excited state ($2\pi \cdot 5.22$ MHz). This corresponds to a relative stability of 10^{-8} . Furthermore, we need the possibility to tune the frequency of the cooling light during the experimental run by 60 MHz in $500 \mu\text{s}$.

The dispersive signal of the newly implemented polarization spectroscopy shows steep slopes, which lead to a more precise frequency stability. However, the tuning range of the frequency is limited to only a few MHz. Thus, for detuning the frequency about 60 MHz, an acousto-optical modulator (AOM) in double-pass configuration is integrated in the beam path. In this configuration, the radio frequency (RF) modulation of the AOM with a frequency ν leads to an effective change of the laser frequency by 2ν .

Typical modulation bandwidths of AOMs are about $\pm 1/4$ of their centre frequency. Hence, for our purpose a custom-made AOM with a relatively large centre frequency of 225 MHz with a bandwidth of ± 50 MHz is implemented. This centre frequency is chosen to match the frequency difference of 450 MHz between the $f = 4 \rightarrow f' = 3$ and the cycling transition $f = 4 \rightarrow f' = 5$. In addition the bandwidth allows a continuously detuning of the laser frequency over 100 MHz.

The cooling laser frequency is therefore locked on the transition $f = 4 \rightarrow f' = 3$. Due to retro-reflection of the first order of diffraction, the difference of the diffraction angle at different RFs is compensated. Thus no beam displacement occurs, and the coupling efficiency of the optical fibre for spatial filtering and guiding the laser light to the main setup remains constant. The advantage of this frequency changing method: fast switching times (160 ns) and a high precision as well as high reproducibility and stability. A further advantage is the possibility to variably choose the cooling laser power for different stages during the experimental run (see section 3.5) by varying the RF power of the AOM. The single-pass diffraction efficiency of the AOM of about 80% in the 1st diffraction order leads to a double-pass efficiency of 64%. Therefore, a tapered amplifier system (TA) consisting of a self-made seed laser and a commercial TA-unit (Sacher Lasertechnik: SYS-400-0850-0500) with an output power of 500 mW replaces the formerly used diode laser.

A further improvement compared to the former setup is the re-routing of the optical fibres used guiding the light from the laser table to the table of the vacuum system. Efficient loading and trapping of atoms in a MOT requires efficient repumping of the atoms from the hyperfine ground state $f = 3$ to the ground state of the cooling transition $f = 4$. This requires a good overlap of the spatial modes of the repumping and cooling light. In the old setup, the two beams were overlapped at the vacuum table. In contrast, both beams are now overlapped on a polarizing beam splitter cube (PBS) before they are coupled into the same optical fibre. Hence, they share the same spatial mode, but are orthogonally polarized when they leave the fibre.

The laser light for repumping, probing, and optical pumping is generated by two Littrow-type diode lasers. Their frequency is locked on the transitions $f = 3 \rightarrow f' = 4$ and $f = 4 \rightarrow f' = (4, 5)$ (cross over peak), respectively. The former is directly resonant to the repumping transition. The light of the latter passes through an AOM with a RF frequency of 130 MHz. The laser frequency of the first order diffraction is shifted close to the cooling transition, providing the imaging light. The zero order is retro-reflected and after passing through the same AOM a second time, the -1st order of diffraction is in resonance with the $f = 4 \rightarrow f' = 4$ transition. This, together with the repumping light

forms the optical pumping light. Two separate fibres for optical pumping and imaging guide the laser light to the vacuum table.

Rb laser system

The laser system of Rb has to fulfil the same requirements as the one for Cs.

Cooling light: The cooling laser system consists of a commercial TA (Toptica: TA-100) using a 1 W tapered amplifier chip (M2K), providing sufficient laser power to simultaneously operate two MOTs. Therefore, the output beam is split into two beams by a PBS. Analogous to the Cs laser system the formerly used DAVLL-scheme was replaced by the more precise subdoppler polarization spectroscopy. The laser frequency is locked on the $f = 2 \rightarrow f' = 1$ transition and shifted by 400 MHz using AOMs in double pass configuration. This yields an effective red detuning of 12 MHz with respect to the cycling transition $f = 2 \rightarrow f' = 3$. In order to obtain independent control over the frequency of both MOTs during the experimental cycle, an AOM with a RF centre frequency of 200 MHz and a bandwidth of ± 50 MHz was inserted into each beam. Each beam is then coupled into an optical fibre for spatial mode filtering, and guided to the vacuum chamber.

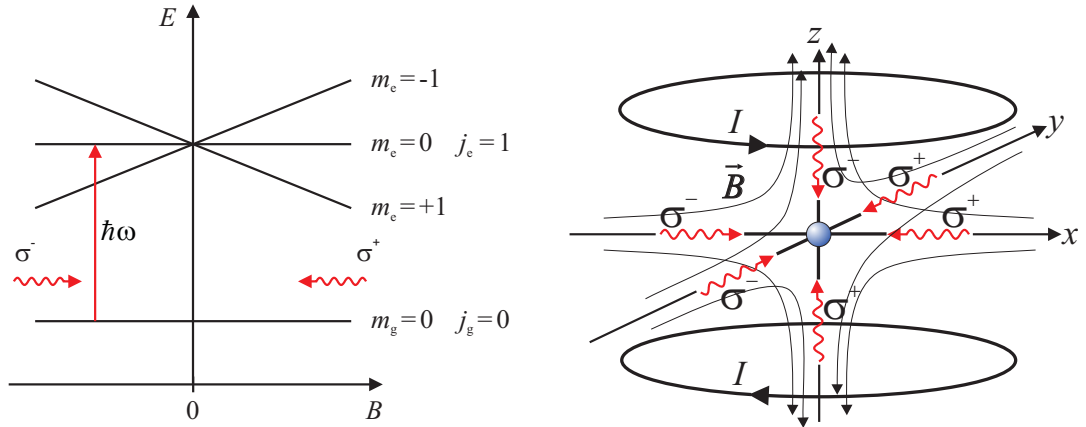
Repumping light: A home made Littrow-type diode laser produces the repumping light with an output power of about 50 mW. Its frequency is stabilized by polarization spectroscopy on the $f = 1 \rightarrow f' = 2$ transition. By means of a PBS, the repumping light is also split into two beams to operate both MOTs.

Imaging light: In order to probe the atoms on the cooling transition, a commercial diode laser (Toptica) with an output power of 25 mW is used. The laser frequency is locked on the $f = 2 \rightarrow f' = (2, 3)$ crossover peak. An AOM with a RF frequency of 130 MHz is integrated in the beam path, shifting the laser frequency in resonance with the cooling transition. This configuration offers the possibility to switch the probe beam rather fast in about 160 ns.

Pushing light: A third Littrow-type diode laser creates the laser light to transfer the atoms from the vapour cell MOT to the MOT in ultra high vacuum region. For this purpose the performance of the DAVLL scheme is sufficient, as stability is not as critical as for the other lasers. The frequency detuning with respect to the cooling transition is optimized to be about 40 MHz.

3.3 Magneto-optical trap

On the way to ultracold mixtures and BECs atoms have to be trapped, cooled and their phase space density has to be increased by about 20 orders of magnitudes. MOTs provide a widespread and relatively simple realization of laser cooling and trapping of neutral atoms, especially alkali atoms as Rb, Cs, K etc. The combination of a velocity and position dependent restoring force allows to trap 1 to 10^{10} atoms depending on the chosen trapping parameters (e.g. magnetic field gradient, light intensity, partial



(a) Schematic of a MOT in one dimension: Magnetic substates are shifted spatially in a magnetic field with a linear magnetic field gradient. The atom moves within a red detuned light field of two counter-propagating orthogonally circular polarized laser beams. A restoring force acts on the atoms toward $z = 0$.

(b) Schematic of a MOT in three dimensions: A quadrupole field is generated by two coils in anti-Helmholtz configuration. In combination with a 3D molasses, the net force exerted on the atoms is directed towards the magnetic field minimum.

Figure 3.3: Schematic of a MOT

pressure). Although MOTs are well known, I will yet present the basic mechanism in order to point out the difference between the two regimes of a many-atoms and the single-atom MOT. This will also show the challenge in setting up a single-atom MOT, which is introduced in chapter 4. A detailed description of typical MOTs can be found in [104].

Consider an atom in the light field of two counter-propagating laser beams, the frequency of which is red detuned with respect to the atomic transition. The atom absorbs preferably photons of the laser beam which counter-propagates its motion, as the Doppler effect tunes them closer to resonance. The photon momentum $\hbar k$ is transferred onto the scattered atom reducing the atomic velocity by the amount $\hbar k/m$, called recoil velocity. Thus, about 10^4 photons have to be scattered to cool the atoms down from room temperature (≈ 300 K) close to absolute zero temperature. This requires a closed optical transition. Averaging over many scattering processes, the net transfer of the following spontaneous emission in a random direction vanishes in a first approximation. The resulting force counteracts the motion of the atom and leads to damping. This corresponds to a frictional force which, in the limit of low velocities, is proportional to the velocity \vec{v} of the atom. Extension to three orthogonal pairs of counter-propagating red detuned laser beams forms a so-called three dimensional optical molasses [105], cooling atoms in all directions. Although the time averaged momentum due to spontaneous emission of photons vanishes, similar to Brownian motion, the time sequence of momentum kicks causes fluctuations of the momentum around its average value. This leads to a heating of the ensemble. The equilibrium of cooling and heating corresponds to the temperature $T_D = \hbar \gamma / 2 k_B$, referred to as Doppler limit. For Rb (Cs) T_D is $146 \mu\text{K}$ ($125 \mu\text{K}$). As

real atoms are multi-level systems, different types of subdoppler cooling schemes using polarization gradients overcome this temperature limit [106].

Overlapping the centre of a magnetic quadrupole field with the intersection of the three pairs of laser beams forms the so-called MOT. In this configuration an additional position dependent force arises from the position dependent Zeeman shift [107]. The basic mechanism is illustrated in figure 3.3(a), considering two counter-propagating orthogonally circular polarized laser beams and a linear magnetic field gradient. For an atomic transition $j_g = 0 \rightarrow j_e = 1$ the magnetic sublevels $m_e = +1$ and $m_e = -1$ of the excited state experience a Zeeman shift changing linearly with position. Atoms in the state $m_e = +1$ at positions $z > 0$ in a red detuned ($\delta < 0$) laser beam scatter more likely σ^+ polarized light than σ^- pushing the atom towards the minimum of the magnetic field.

Extending this scheme to three dimensions, atoms can be simultaneously trapped and cooled in all spatial directions. In MOTs, the density of the trapped gas is typically limited to 10^{12} cm^{-3} due to two effects: First, for large atomic densities, re-emitted and thus resonant photons are reabsorbed by the trapped atoms with a high probability before leaving the atomic cloud. This mechanism is called radiation trapping [108]. Second, light induced collisions between atoms in the ground and excited states lead to atom loss from the trap. In this process, the excited atom is de-excited, releasing large amounts of kinetic energy effectively removing the colliding atoms from the MOT. This leads to heating and trap losses as collisions for higher densities become more and more probable [109].

Experimental realization

In our experiment four different types of MOTs are operated at two different positions for the two species Rb and Cs. The MOT parameters differ depending on the regime of the number of atoms.

Producing a Rb BEC requires a large initial number of Rb atoms. Thus, a Rb double-MOT scheme is used, as mentioned in section 3.1. The first MOT, a vapour cell MOT, serves as a cold atom source providing fast loading of up to 10^{10} Rb atoms from the background. This MOT is formed by the optical molasses of three retro-reflected laser beams in combination with two coils in anti-Helmholtz configuration. A near resonant laser beam (pushing beam) with a power of $800 \mu\text{W}$ and a detuning of $\Delta = 2\pi \cdot 40 \text{ MHz}$ with respect to the cooling transition is focused into this MOT. Thus, the precooled atoms are transferred by radiation pressure to the UHV-MOT in the glass cell, which is 60 cm below the first one. The UHV-MOT is designed as a standard six-beam MOT, allowing for a careful alignment and power balancing of the counter-propagating beams. The repumping light for both MOTs propagates only along the z -axis to avoid repumping and thus accelerating the atoms in the atomic beam. This setup allows us to trap about 10^9 Rb atoms in about 25 s at a temperature of about $100 \mu\text{K}$.

The second species (Cs) is directly trapped at a vapour cell MOT in the UHV region, where the partial Cs pressure is at most 10^{-10} mbar. The partial background pressure of Cs can be increased for a short time by switching on ultra-violet light (395 nm)

	Rb		Cs	
	vapour cell MOT	UHV-MOT	standard MOT	single atom MOT
dB_{quad}/dz (G/cm)	12	10	10	300
w (mm)	10	8	8	1
P_{cool} (mW)	30	15	5	0.1
Δ	$-2.5 \Gamma_{\text{Rb}}$	$-2.5 \Gamma_{\text{Rb}}$	$-2 \Gamma_{\text{Cs}}$	$-1.5 \Gamma_{\text{Cs}}$
P_{rep} (mW)	3	3	4	0.3
number of atoms	10^{10}	10^9	10^7	1 – 10

Table 3.1: Parameters of the four different MOTs operated in our experiment. Here, P_{cool} and P_{rep} denote the cooling laser power per each beam and the total repumping laser power, respectively. The line width of the D2-lines for Rb and Cs are $\Gamma_{\text{Rb}} = 2\pi \cdot 6.07$ MHz and $\Gamma_{\text{Cs}} = 2\pi \cdot 5.22$ MHz, respectively.

which removes Cs atoms from the walls of the vacuum system by light-induced atom desorption (LIAD) [110, 111]. Depending on the particular experiment we work with either few (1...10) or many (10^7) Cs atoms. The latter one is used for experiments investigating the inter-species interaction properties. Here, the MOT parameters are similar to that of Rb (see table 3.1). In contrast to the Rb MOT, for Cs the repumping light is present in each beam.

When operating a single Cs atom MOT, the MOT parameters differ in order to reduce the mean number of trapped atoms. Atom numbers between 1 and 10 can be obtained by a 30-fold increase of the magnetic field gradient dB_{quad}/dz , and a one order of magnitude smaller MOT beam waist w , whereas the light intensity remains constant. Here, the alignment is more critical due to the much smaller beam waists resulting in a smaller intersection region of the MOT beams. In addition, the MOT performance is more sensitive to the overlap of this intersection point with the magnetic field minimum, due to the high gradient quadrupole field. Typical loading rates are thereby reduced to approximately 1 s^{-1} . Details on the operation of the single atom MOT are discussed in chapter 4.

The laser beams for the MOTs of both species are overlapped using the same optical components. Wavelengths selective $\lambda/2$ -retardation plates allow to control the power balancing for both wavelengths independently.

3.4 Magnetic trap

Atom traps based on the scattering of light are always associated with the energy scale of the recoil energy $\hbar^2 k^2 / (2m)$, which is much larger than the energy scales of degenerate quantum gases. Thus, a different kind of trap has to be used. In our case, the atomic cloud is purely magnetically trapped. Magnetic traps form conservative potentials by exploiting the interaction between the magnetic moments of the atoms with an inhomogeneous magnetic field and are thus free from photon scattering. The force exerted on the atoms is given by $\vec{F} = \nabla(\vec{\mu} \cdot \vec{B})$, where, due to the Zeeman shift, the potential for a given magnetic substate is $U = -\vec{\mu} \cdot \vec{B} = g_f m_f \mu_B |\vec{B}|$. As a consequence of the Maxwell equations, no magnetic monopoles exist in free space. Thus, only static magnetic field minima can be created. In such field configurations, atomic states with a positive magnetic moment ($g_f m_f \mu_B > 0$) are magnetically trappable, called low field seeking states [112]. Again, quadrupole fields provide such a magnetic field minimum where atoms can be trapped.

It is important to note that, while the atom moves in the trap, the magnetic moment must adiabatically follow the orientation of the magnetic field. Otherwise, the atom can lose its spin polarization and become a high field seeker which is expelled from the trap. This implies that the Larmor precession rate $\omega_L = \mu B / \hbar$ has to be larger than the change of the magnetic field $\omega_L \gg |dB/dt|/B$. At the centre of the trap, where the magnetic field vanishes, this adiabaticity condition is not satisfied anymore. At low temperatures, however, the density in the vicinity of the trap centre increases, leading to trap losses due to so-called Majorana spin flips which occur when the adiabaticity is violated [113].

In order to overcome the leakage of atoms close to the zero of the magnetic field, a potential minimum with a non-zero field value has to be realized. Different types of traps overcoming this problem have been established in quantum gas experiments [114, 4, 115, 116]. In our experiment, the so-called QUIC-trap [116] is used. Here, a third coil (Ioffe coil) is added orientated perpendicularly to the quadrupole coils. The magnetic field in the far field can be described by a magnetic dipole field

$$\vec{B}(\vec{r}') = \vec{r} - y_I \vec{e}_y = \frac{3p y' \vec{r}' - p \vec{r}'^2 \vec{e}_y}{r'^5}, \quad (3.1)$$

where the centre of the Ioffe-field is shifted by y_I with respect to the quadrupole centre and p denotes the dipole moment of the Ioffe coil. Taking into account both magnetic fields of the quadrupole and the Ioffe coils, the total potential close to the magnetic field minimum can be described in first order approximation by

$$U = \mu B \quad (3.2)$$

$$= \frac{1}{2} m (\omega_\rho^2 (x^2 + z^2) + \omega_{ax}^2 y^2) + \mu B_0, \quad (3.3)$$

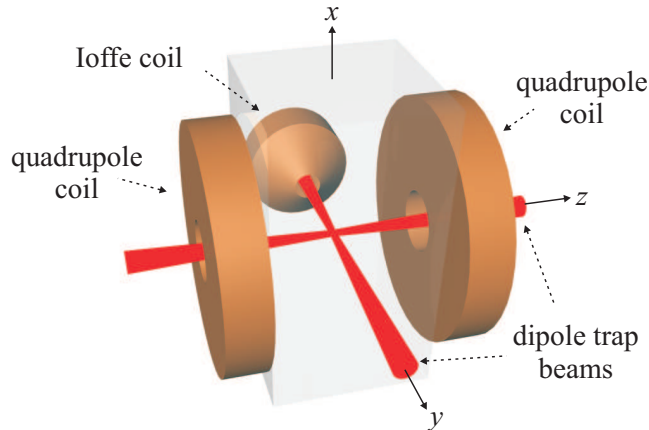


Figure 3.4: Schematic of the main part of the Rb-Cs apparatus: The two large coils (brown cylinders) provide the quadrupole field. Perpendicularly to the quadrupole coils an additional coil (brown, tapered cylinder) complements the magnetic field system to form the QUIC configuration. Within the coil system the glass cell is positioned. The beams of the crossed dipole trap (red) pass through the different coils, crossing at the centre of the quadrupole trap.

where

$$\omega_\rho = \frac{3}{2} \xi \sqrt{\frac{\mu}{m B_0}} \quad (3.4)$$

$$\omega_{ax} = \frac{2}{6^{1/8}} \sqrt{\frac{\mu \xi^{5/4}}{m p^{1/4}}}. \quad (3.5)$$

are the trap frequencies along the radial and the symmetry axes, respectively, including the quadrupole magnetic field gradient $2 \cdot \xi = dB_{\text{quad}}/dz$. Thus the trap is to a good approximation harmonic. An increasing offset field B_0 leads to decreasing trap frequencies. Too small trap frequencies, however, are unwanted as they lead to an inefficient re-thermalization during the next cooling step, the evaporative cooling described in section 3.6. Therefore, the offset field must be chosen as a compromise between the reduction of Majorana spin flips and sufficiently large trap frequencies.

The QUIC trap realized in Bonn [117] consists of two coils (208 windings each, inner radius = 14.9 mm) in anti-Helmholtz configuration, forming the quadrupole field for the MOT. The Ioffe coil (103 windings, inner radius = 3.1 mm) has a hole with a radius of 2 mm which allows optical access to the atoms for a dipole trap beam. The coils are electrically connected in series to compensate for magnetic field fluctuations due to the noise of the current supply. At a current of 16.9 A the trap frequencies are $\omega_\rho = 2\pi \cdot (190 \pm 2)$ Hz and $\omega_{ax} = 2\pi \cdot (18 \pm 1)$ Hz, where the offset field is about 1 G. The spatial overlap of the MOT and the quadrupole trap is trivially given as the same coils are used for both traps. However, the centre of the QUIC trap is shifted by 7 mm towards the Ioffe coil.

3.5 Transport of the atoms from the MOT to the QUIC trap

Efficient transfer of the atoms from the MOT to the magnetic trap without reducing the phase space density requires a dense, cold atomic sample in a well defined spin state. A combination of first a compression stage with an increased quadrupole gradient field, second a molasses stage with no magnetic field applied, and third, optical pumping ensure a transfer to the magnetic trap at constant phase space density.

After loading a sufficient number of atoms into the UHV-MOT (10^9 of Rb and 10^7 of Cs) the magnetic field gradient is ramped up from 6 G/cm to 18 G/cm in the compression stage. This leads to a larger restoring force towards the trap centre and therefore an increased atomic density. In order to avoid radiation trapping, the cooling laser is detuned further to the red. Within 10 ms the detuning is swept from -15 MHz to -25 MHz with respect to the cooling transition.

This experimental stage is followed by a three dimensional molasses stage, taking about 8 ms. This effectively reduces the temperature of the atomic cloud by subdoppler cooling to about $50 \mu\text{K}$. The cooling laser detuning of Rb (Cs) is experimentally optimized to be about -70 MHz (-60 MHz).

Subsequently, the sample is spin polarized. Both species are optically pumped into their doubly polarized states, i.e. $|f = 2, m_f = 2\rangle$ for Rb and $|4, 4\rangle$ for Cs. These states are magnetically trappable. In addition, inelastic collisions due to spin exchange (see section 2.2) are suppressed because these states cannot further increase their spin quantum number². Furthermore, doubly polarized states are ideally suited to experimentally measure the intra- and inter-species triplet scattering length, as only the triplet scattering length contributes to elastic scattering between these states. Rb (Cs) is optically pumped by means of circularly polarized laser light driving the σ^+ transitions $|f = 2\rangle \rightarrow |f' = 2\rangle$ and $|f = 1\rangle \rightarrow |f' = 2\rangle$ ($|f = 4\rangle \rightarrow |f' = 4\rangle$ and $|f = 3\rangle \rightarrow |f' = 4\rangle$). Atoms in the doubly polarized states are not resonant with the light field anymore and therefore experience no further heating. Here, the quantization axis is oriented in parallel to the laser beam propagation axis. It is given by an additional magnetic field originating from a single coil in parallel to the Ioffe coil, which creates a magnetic field of the order of 1 G at the centre of the quadrupole coils. As the Larmor frequency is much faster than the slow spatial variations of this inhomogeneous magnetic field experienced by the oscillating atoms, the atomic spin follows the changes of the quantization axis. This part of the sequence is time critical as the atoms are not trapped during this stage. The optical pumping takes 1.5 ms, while the repumping light is switched off $250 \mu\text{s}$ after the cooling laser beam, to ensure that all the atoms are pumped into the $f = 2$ ($f = 4$) state.

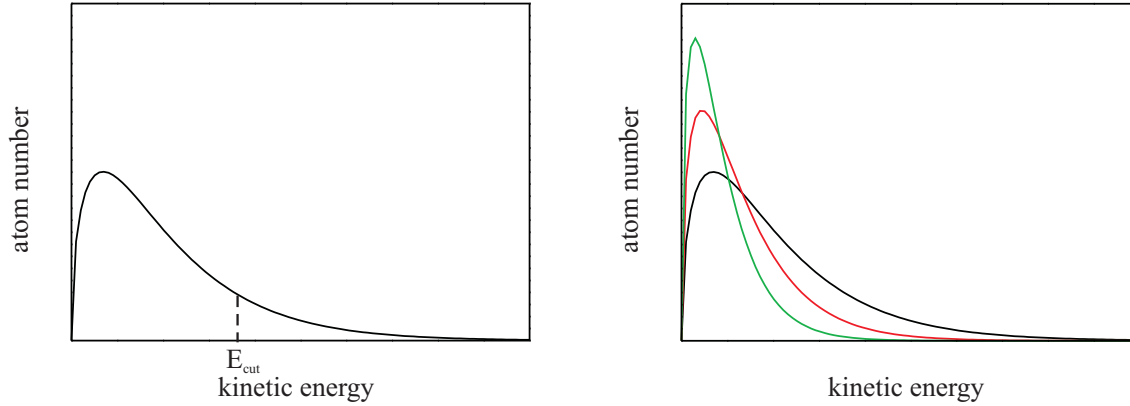
The spin polarized sample is subsequently transferred into the magnetic quadrupole trap. The magnetic field gradient must be large enough ($> 15.2 \text{ G/cm}$ ($> 23.2 \text{ G/cm}$))

²Inelastic collisions including mechanisms which do not conserve the total angular momentum, cannot be fully avoided in a magnetic trap, as the absolute ground state of both species is not magnetically trappable.

for Rb (Cs)) to hold the atoms against gravity. In order to avoid the atomic ensemble being heated due to centre-of-mass oscillations, the centre of the MOT/molasses and the magnetic quadrupole trap must coincide. As the magnetic coils used for both of the traps are the same, fine adjustments have to be done by the alignment and the power balancing of the MOT beams. Experimentally, the transfer into the quadrupole trap is performed by increasing the magnetic field gradient to 51 G/cm in 300 μ s. At this gradient the cloud size and temperature in the quadrupole trap match the ones of the cloud in the optical molasses. In order to increase the atomic density and hence the collision rate, the magnetic field is increased adiabatically to 104 G/cm. During this adiabatic process the phase space density remains constant, but the temperature of the ensemble increases, while the increased collision rates provide good starting conditions for the evaporative cooling stage. In the next experimental step, the current of the Ioffe coil is slowly ramped up to the same final value as the current of the quadrupole coils. Thus Majorana spin flips at the trap centre as well as magnetic field fluctuations due to the noise of the power supply are prevented. In this configuration the atoms are 7 mm displaced from the quadrupole coils centre towards the Ioffe coil. Typically $5 \cdot 10^8$ ($1 \cdot 10^7$) Rb (Cs) atoms at a temperature of 200 μ K are initially stored in the QUIC trap.

3.6 Evaporative cooling

The quantum phase transition to a BEC occurs at a phase space density of about $\lambda_{\text{dB}}^3 n = 2.61$. Another cooling stage of the atomic ensemble in the magnetic trap is necessary therefore. A well-known and commonly used cooling technique in quantum gas experiments is the so-called forced evaporative cooling [2], which is up to now the only cooling mechanism leading to quantum degeneracy. This technique is based on removing atoms with a kinetic energy larger than the average energy of the atomic ensemble. The remaining atoms rethermalize by elastic collisions, reaching an equilibrium with a reduced temperature. The energy distribution of the atomic cloud in the QUIC trap can be described by Maxwell-Boltzmann statistics. Removing all atoms with an energy E_{kin} larger than a preset threshold ($E_{\text{kin}} > E_{\text{cut}}$) corresponds to cutting the high energy part of the Maxwell-Boltzmann distribution. If this threshold E_{cut} is continuously lowered, the process is called "forced evaporative cooling". Assuming that during the evaporation only atoms with an energy above $\eta k_{\text{B}} T$ are evaporated, where η is a fixed ratio $E_{\text{cut}}/k_{\text{B}} T$, the efficiency of the evaporation process can in principle be arbitrarily enhanced by increasing η . However, in real experiments the efficiency and the time scale of the evaporation process are determined by the elastic and inelastic scattering properties. While the elastic collisions lead to the important thermalization of the sample, inelastic scattering leads to heating of the sample and atom loss. Therefore a compromise has to be found where, on the one hand, the evaporation process is fast enough to neglect inelastic scattering and, on the other hand, it is slow enough so that rethermalization



(a) Boltzmann distribution (solid line) of the kinetic energy for a fixed temperature T of the ensemble. The dashed line indicates the cut-off energy E_{cut} above which all atoms are removed from the trap.

(b) Boltzmann distribution for three different temperatures during the evaporation ramp. In this diagram in each step (black→red, red→green) 12% of the hottest atoms are removed. After rethermalization, the Boltzmann distribution becomes more narrow and the peak shifts to a lower energy.

Figure 3.5: Boltzmann distribution during the evaporation process

can take place. The rethermalization rate τ_{reth} is given by

$$\frac{1}{\tau_{\text{reth}}} \propto n T^{1/2} \sigma_{\text{el}}, \quad (3.6)$$

where n denotes the atomic density, T the temperature of the cloud and σ_{el} the elastic scattering cross section. Large trap frequencies, which correspond to strong confinement, increase the rethermalization rate and hence speed up the cooling process.

In magnetic traps, forced evaporative cooling is realized by applying radio frequency or microwave radiation driving Zeeman or hyperfine state transitions, respectively, to magnetically untrapped or anti-trapped states. The kinetic energy of an atom oscillating in the trap is converted to potential energy due to the position dependent Zeeman shift, while the atom moves away from the trap centre. The kinetic energy of the atom is thereby transformed into oscillation amplitude and hence into an energy dependent Zeeman splitting. This offers the possibility to remove atoms energy selectively to un- or anti-trapped states.

We use a microwave frequency of 6.83 GHz, which drives the ground state hyperfine transition of Rb. Because of the selection rules, Rb atoms in the doubly polarized state can only be transferred to the anti-trapped $|1, 1\rangle$ state. Initially, the microwave field is resonant to the outer regions of the trap, removing only atoms with relatively large kinetic energy. Subsequently, the microwave frequency is continuously decreased, removing atoms with less and less kinetic energy, thereby realizing the forced evaporation. For efficient cooling we use a microwave power in the Watt range. In this power regime, coupling between the $|2, 2\rangle$ and $|1, 1\rangle$ states is too strong to be treated as a

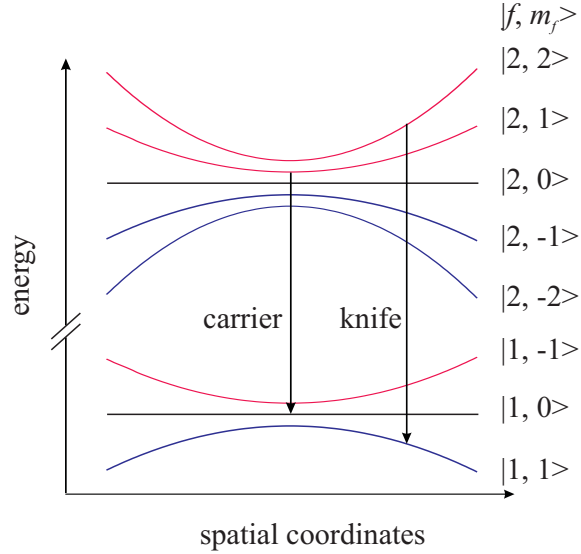


Figure 3.6: Experimental realization of the forced evaporative cooling of Rb: Spatial dependent Zeeman splitting of the two Rb hyperfine ground states in the QUIC trap are shown. The red, black, and blue lines indicate the trapped, non-trapped, and anti-trapped Zeeman states, respectively.

small perturbation. The coupled system of the atom and microwave field can then be described in the dressed atom approach [118]. The transition probability is proportional to the microwave radiation power and inversely proportional to the atomic velocity. As the microwave field approaches the resonance condition at the trap center, the effective trap frequency is reduced due to the strong coupling of the two states. At the end of the evaporation process the microwave radiation power is reduced in order to ensure a sufficiently strong confinement of the atoms.

The Cs atoms are unaffected by the microwave radiation, as the hyperfine splittings of Rb and Cs differ by 2.8 GHz. Thus, the forced microwave evaporative cooling is species selective. However, due to elastic collisions between Rb and Cs, the latter one is sympathetically cooled by the actively cooled Rb. This provides an efficient cooling of Cs without a significant loss of Cs atoms [79].

The microwave setup consists of a modular source, an amplifier, and an antenna. The heart of the source is a local oscillator (MITEQ BCO-010-06830-05), phase stabilized by a frequency generator (Rohde & Schwarz) at a frequency of 10.008 MHz, yielding a frequency of $\nu_{lo} = 10.008 \text{ MHz} \cdot 683$. In addition, a frequency generator (Tabor) is used to generate an arbitrary frequency modulation waveform in the range of 1 to 50 MHz. This frequency generator replaces two arbitrary waveform generators (Agilent 33120A and 33250A) of the former setup. Mixing the signal of the frequency generator with the local oscillator output, two sidebands with frequencies of $\nu = \nu_{lo} \pm \nu_{\text{Tabor}}$ are produced. The upper sideband is used as evaporation knife. A pin-diode attenuator (MITEQ MPAT-64072-60-20-1F/1F) with an attenuation between 10 and 60 dB allows adjusting

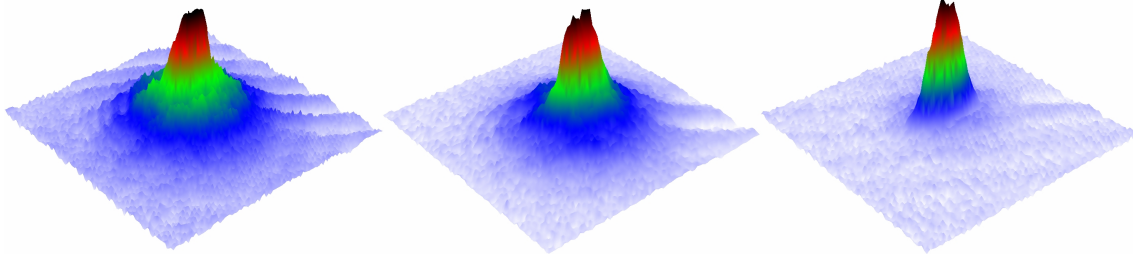


Figure 3.7: Density distribution of the atomic Rb cloud after different evaporation stages: The phase transition occurs between the left picture (thermal cloud) and the one in the centre, which shows a partially condensed cloud. Further evaporation leads to a quasi pure BEC with $4 \cdot 10^5$ atoms (right picture).

the microwave power during the sequence. The microwave radiation is amplified to about 8 W in two stages (preamplifier: MITEQ AMF-3B-040090-25P, power amplifier: Kuhne KU684XL). Finally, the microwave radiation is fed into a wave guide, which directly points to the position of the atomic cloud.

In the former setup using the two arbitrary waveform generators, the spectral width of the sideband was about 10 kHz. For comparison, the chemical potential of a BEC in a typical magnetic trap is about $h \cdot 10$ kHz. Thus, a controlled and precise evaporative cooling in the vicinity of the phase transition was not possible. For the new setup, however, the frequency spectrum of the evaporation sideband shows a sharp peak with a width of less than 10 Hz. The broad background spectrum with a width of 10 kHz is still present, but it is suppressed by 30 dBm. The final stage of the evaporation ramp can therefore be controlled much more precisely and it results in BECs of about $4 \cdot 10^5$ atoms, which are twice as many atoms as in the former setup.

Experimentally we have observed atoms in the magnetic trapped state $|2, 1\rangle$, most probably due to a transfer of the atoms from the anti-trapped state $|1, 1\rangle$ as the atoms leave the trap, thereby crossing regions where the transition to $|2, 1\rangle$ is resonant [79]. Atoms in $|2, 1\rangle$, however, have decoupled from the cooling process but still can collide with atoms in the $|2, 2\rangle$ state, resulting in heating and atom loss. In order to avoid population in $|2, 1\rangle$, we tune the carrier frequency to the $|2, 1\rangle \rightarrow |1, 1\rangle$ transition in the trap centre, efficiently depleting the $|2, 1\rangle$ state.

The theory of evaporative cooling discussed so far is also valid in optical dipole traps, in which all magnetic substates can be trapped. Optical dipole traps will be introduced in the next section. Here, forced RF or microwave evaporation is not applicable. Instead, evaporative cooling is realized by reducing the laser power which leads to a reduction of the trap depth.

3.7 Optical dipole trap

In contrast to magnetic traps, optical dipole traps allow to store all magnetic substates, in particular the absolute ground state, where inelastic collisions are strongly suppressed. The trapping mechanism relies on the electric dipole interaction. In an oscillating electric field, a dipole moment is induced in a neutral atom. The interaction of the induced dipole moment with the external electric field leads to a force on the atom.

As these traps can be operated with far-detuned light, they can feature low photon scattering rates. Hence, long storage times with low heating rates are achieved. Furthermore, an external magnetic field can be applied as a free parameter. Therefore, this trap is well suited for experiments in which magnetic Feshbach resonances are investigated or used as a tool for tuning the scattering length.

A detailed discussion of dipole traps can be found in [119]. In a simplified system of a two-level atom the electric dipole force in the classical picture can be described by considering the atom to be an oscillator in a classical light field. Hence, the dipole potential is given by

$$U = -\frac{1}{2} \langle \vec{p} \vec{E} \rangle \quad (3.7)$$

$$= -\frac{1}{2 \epsilon_0 c} \text{Re}(\alpha) I, \quad (3.8)$$

where \vec{p} and I denote the induced dipole moment of the atom and the intensity of the light field given by $I = 2 \epsilon_0 c |E|^2$, respectively. The complex polarizability α , which depends on the frequency ω of the driving field, can be written as

$$\alpha = 6 \pi \epsilon_0 c^3 \frac{\Gamma}{\omega_0^2 \left(\omega_0^2 - \omega^2 - i \frac{\omega^3}{\omega_0^2} \Gamma \right)}. \quad (3.9)$$

For two-level systems the decay rate Γ of the excited state is given by the dipole matrix element between the ground $|g\rangle$ and the excited state $|e\rangle$

$$\Gamma = \frac{\omega_0^3}{3 \pi \epsilon_0 \hbar c^3} |\langle e | \mu | g \rangle|^2. \quad (3.10)$$

The imaginary part of the polarizability corresponds to a Lorentzian absorption function. This gives rise to a scattering rate

$$\Gamma_{\text{sc}}(\vec{r}) = -\frac{1}{\hbar \epsilon_0 c} \text{Im}(\alpha) I(\vec{r}). \quad (3.11)$$

This dissipative photon-atom interaction leads to heating of the ensemble due to photon recoil and for finite trap depths even to atom loss. In typical dipole traps the detuning is small compared to the transition frequency ω_0 ($|\Delta| \equiv \omega - \omega_0 \ll \omega_0$), hence the rotating

wave approximation, where $\frac{\omega}{\omega_0} \approx 1$, can be applied and gives the simple result

$$U(\vec{r}) = \frac{3 \pi c^2}{2 \omega_0^3} \frac{\Gamma}{\Delta} I(\vec{r}) \quad (3.12)$$

$$\Gamma_{\text{sc}}(\vec{r}) = \frac{3 \pi c^2}{2 \hbar \omega_0^3} \left(\frac{\Gamma}{\Delta} \right)^2 I(\vec{r}). \quad (3.13)$$

Depending on the sign of the detuning Δ , the dipole potential of an intensity maximum can be attractive (for $\Delta < 0$) or repulsive (for $\Delta > 0$). The most simple realization of such a dipole trap is a focused, red detuned ($\Delta < 0$) Gaussian laser beam. Here, atoms are stored in the focus at maximum intensity. Long storage times require low scattering rates in order to avoid heating of the atomic cloud. To combine a sufficiently deep trap depth with low scattering rates, the detuning can be increased. For a chosen trap depth the ratio $I(\vec{r})/\Delta$ is fixed, where the scattering rate can be reduced by increasing the detuning. Blue detuned dipole traps overcome the unwanted heating due to photon scattering as the atoms are trapped in the intensity minimum of the light field. Nevertheless blue detuned traps are rarely found, as an additional confinement, e.g., a magnetic field has to be implemented.

In reality atoms are multi-level systems and substates have to be considered. In the dressed state picture the second order perturbation theory can be used to calculate the energy shift of each substate [119]. The potential for different magnetic substates depends also on the polarization of the light field. In the case of linearly polarized light the energy shifts for all substates are the same equals the one for a two-level atom

$$\Delta E = \pm \frac{3 \pi c^2}{2 \omega_0^3} \frac{\Gamma}{\Delta} I. \quad (3.14)$$

This so-called AC-Stark shift corresponds to the dipole potential of a two-level atom. For detunings larger than the hyperfine splitting of the excited state only the AC-Stark shift of the ground state plays a role.

In our experiment a crossed dipole trap at a wavelength of 1064 nm is realized to store atoms in a purely optical trap. The optical power of each dipole trap beam is about 2 W. The focal points of both beams spatially coincide and the waist is chosen to be $w_0 = 86 \mu\text{m}$, while the beams propagate perpendicularly to each other in the horizontal plane (figure 3.4). This yields a total trap depth of $U_0 = k_B \cdot 45 \mu\text{K}$. Along both axes of the two beams the trap depth decreases to half the potential depth at a distance of one waist from the trap centre. Thus the effective potential depth of the crossed dipole trap can be deduced to be $U_{\text{eff}} = U_0/2 = k_B \cdot 22.5 \mu\text{K}$. The trap frequencies

$$\omega_{y,z} = \sqrt{\frac{2 U_0}{m w_0^2}} = 2 \pi \cdot 173 \text{ Hz} \quad (3.15)$$

$$\omega_x = \sqrt{\frac{4 U_0}{m w_0^2}} = 2 \pi \cdot 244 \text{ Hz} \quad (3.16)$$

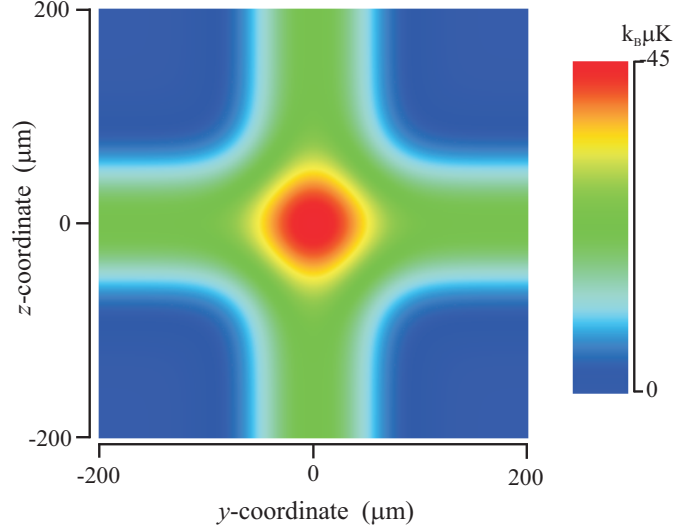


Figure 3.8: Density plot of the crossed dipole trap: Two orthogonal beams along the y - and z -axis are focused to a waist of $86 \mu\text{m}$.

are obtained by a harmonic approximation of the potential. In contrast to the weak confinement along the laser beam axis in a single beam dipole trap, they are of the same order of magnitude for each direction in the crossed dipole trap, resulting in a more isotropic atomic cloud. The strong confinement along the axis of gravitation $\omega_x = \sqrt{2}\omega_{y,z}$ increases the efficiency of evaporative cooling in the optical trap, as it maintains large elastic scattering rates and thus enables short rethermalization times. In addition, a strong confinement reduces the gravitational sag. In mixture experiments the species dependent sag can lead to a reduced or vanishing overlap of the clouds and thus the thermal contact.

Experimental setup of the dipole trap

In order to realize an optical dipole trap, we use an arc-lamp pumped Nd:YAG laser (Quantronix, model 116EF-OCW-10) with an output power of 10 W emitting a linearly polarized Gaussian beam. The longitudinal modes are reduced from more than 30 to about 4 modes by an etalon inserted within the laser cavity. The setup of the laser itself is described in more detail in the thesis of Wolfgang Alt [120]. The output beam is split into two beams for both dipole trap branches using a polarizing beam splitter cube in combination with a $\lambda/2$ -retardation plate. In each beam an AOM with a centre RF frequency of 80 MHz is used for fast switching (160 ns) and continuously adjusting the laser beam power. The frequencies of both branches are slightly detuned with respect to each other using the 1^{st} and -1^{st} diffraction order of the AOM. This destroys the fixed phase relation between the beams and thus avoids cross interference at the position of the atoms. The diffracted laser beams are guided to the experiment by high power, polarization maintaining single mode fibres and are collimated to a $1/e^2$ -radius of 1.9 mm. Two aspheric lenses (doublets) with a focal length of 500 mm each focus the

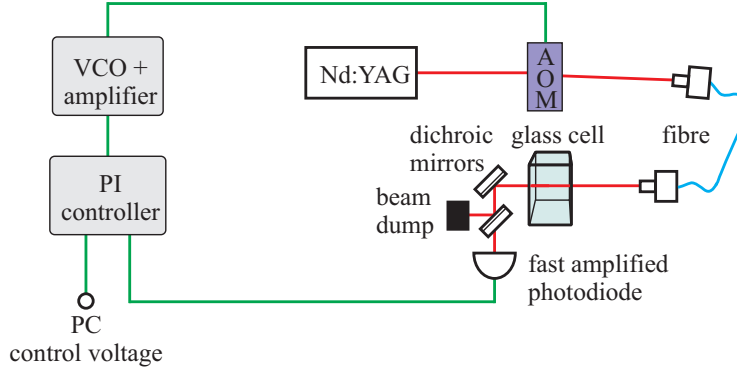


Figure 3.9: Block diagram of the servo loop to control the dipole trap laser power. The red and green solid lines indicate the laser light and the electrical connections, respectively. Details are described in the text.

beam along the Ioffe axis and the imaging axis to the centre of the quadrupole coils to a waist of $86\ \mu\text{m}$. The near infrared light is spatially overlapped with the 780 and 852 nm light used for imaging and the molasses on dichroic mirrors. At the position of the atoms, each beam has a power of about 2 W.

3.7.1 Power stabilization of the dipole trap beams

The experimental reality poses stringent requirements on the stability and control of the laser beam power for the dipole trap: During the experimental sequence, ultracold clouds are stored in the dipole trap for several seconds. In order to reach condensation, the precooled atomic cloud shall be evaporatively cooled in the optical trap by lowering the laser beam power. Furthermore, we plan to transport the atoms by 7 mm from the QUIC trap position to the centre of the quadrupole coils in Helmholtz configuration, thereby creating a homogeneous Feshbach field, and to spatially overlap the cold cloud with a single atom loaded into the MOT. During this magnetic transport the dipole trap beam along the Ioffe axis is supposed to keep the radial trapping frequencies ω_x and ω_z constant. Thus, stable and well controllable laser power is crucial for a reliable operation of the experiment. Fluctuations of the laser light power can be caused by e.g. polarization changes upon passing the fibre, resulting in a variation of power after a PBS. In addition, a non-perfect pointing stability of the laser beam in front of the fibre modifies the coupling efficiency. A power stabilization is therefore built up in order to compensate long time as well as short time fluctuations of the power. Furthermore, noise at frequencies below the bandwidth of the controller can be reduced. In our case, the constructed proportional-integral-controller (PI-controller) features a bandwidth of 30 kHz.

The servo loop is schematically drawn in figure 3.9. The controlled system consists of the abovementioned AOM allowing to adjust the power of the beam by changing the voltage controlled radio frequency power. The $\pm 1^{\text{st}}$ order diffracted beam is coupled into

a fibre and guided to the experiment. After passing through the glass cell of the vacuum chamber, a dichroic mirror (reflectivity of 99 % at 1064 nm, reflectivity of 1 % at 780 and 850 nm) separates the dipole trap beam from the optical pumping and imaging light. A second dichroic mirror with a poor reflectivity of only 90% reflects most of the dipole trap light into a beam dump. The remaining 10% of the laser light is attenuated by neutral density filters and focused on a fast photodiode (bandwidth >1 MHz), followed by a transimpedance amplifier. To minimize the noise, the transimpedance resistor R is chosen to be as low as 30 k Ω . Thermal resistor noise, also denoted as Nyquist noise and generated by the Brownian motion of the charge carriers, scales with \sqrt{R} [121, 122]. In addition, the relative shot noise of the photocurrent is proportional to \sqrt{P}/P , where P is the detected laser power. Hence, in order to minimize the noise, a low resistance value is desirable, thereby reducing the amplification and the sensitivity of the amplified photodiode. A lower limit for the resistance value is given by the output current of the used operational amplifier (OPA655). Its output signal is compared with a control signal (setpoint) given by the computer or a waveform generator using an instrumentation amplifier (AD624). The difference of these two signals is amplified by the PI-controller. A schematic of the control board is shown in Appendix B. A diode (SB 120) in combination with a voltage divider ensures the output voltage to be in the range of 0 to 1 V to drive the amplitude modulation input of the voltage controlled oscillator (VCO). Hereby, the RF power entering the AOM is regulated.

The settings of the PI-controller are optimized by measuring the transfer function of the open servo loop. A typical Bode diagram of one of our two power stabilizations is shown in figure 3.10. The 0 dB crossing of the gain of the transfer function defines the bandwidth (gain crossover frequency). The phase margin at this frequency determines the transient effect. A vanishing phase margin would lead to an undamped oscillation, a phase margin of 90 degrees corresponds to the critical damping condition. For phase margins in-between, a damped oscillation around the final value occurs. An optimal compromise between a short transient time on the one hand and a relatively small (4%) overshoot on the other hand is obtained for a phase margin of 60 degrees. In a first approach, the 0 dB crossing is chosen by the proportional amplification. In order to minimize the difference of the final value from the setpoint, an integral amplifier is added. Here, the gain for low frequencies below a cut-off frequency is increased, whereas the phase is decreased by at most -90 degrees. For a proper critical frequency the gain crossover frequency is not influenced by the integral part, if the critical frequency is much lower than the frequency of the 0 dB crossing. For frequencies approaching 0 Hz (dc) the gain tends towards infinity leading to a vanishing offset with respect to the setpoint.

Optimizing this configuration, the open-loop transfer function is measured and plotted in figure 3.10. The bandwidth is determined to be 30 kHz. As the transfer function depends on the setpoint, we have to make sure that the phase margin does not go below 60 degrees in order to ensure a stable, not oscillating servo loop for the entire controlled range. We choose a phase margin of 100 degrees, thereby shifting the compromise mentioned above to a regime where overshoots are negligible at the expense of larger transient times. As

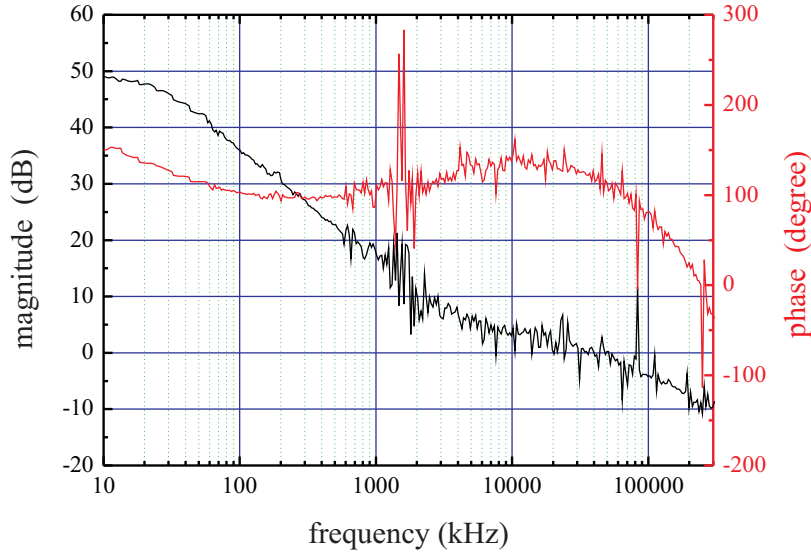


Figure 3.10: Bode-diagram for a power stabilized Nd:YAG laser: The black and red lines indicate the measured magnitude and phase of the open servo loop, respectively. The 0 dB crossing of the magnitude defines the bandwidth, which is about 30 kHz. The phase margin given by the phase at the bandwidth is determined to be about 100 degrees.

a higher bandwidth is not required for our purpose, we renounce the implementation of a derivative part, which would increase the phase and gain for high frequencies. For comparison, the trap frequencies of the dipole trap are $2\pi \cdot 173$ Hz and $2\pi \cdot 244$ Hz. Thus, noise at these frequencies and their first harmonics are suppressed by the servo loop, which could otherwise lead to parametric heating and/or atom loss.

As a final analysis of the locking scheme and also to show the importance of such PI-controllers, the noise of the locked system is compared to the one of the unlocked system. Figure 3.11 shows these noise measurements. The noise of the fast amplified photodiode is measured (black graph) by blocking the laser beam. Here, the $1/f$ -noise as well as the power line resonance at 50 Hz and all its higher harmonics are visible. The blue graph shows the noise of the laser light along with the photodiode. In particular for low frequencies, the noise level has grown by 60 dB. A resonance at 1.5 kHz can be observed. We attribute this resonance to relaxation oscillations of the Nd:YAG-laser. They occur in laser systems in which the lifetime of the excited state of the active medium is much larger than the damping time of the cavity. Variations of the pump power lead to oscillations around the equilibrium, when the system relaxes. Typical oscillation frequencies of a Nd:YAG-laser are in the range of 1 to 10 kHz depending on the cavity and the present pumping rate [123].

When the servo loop is closed and thus the laser beam power stabilized, the noise is clearly reduced within the bandwidth of the circuit. The amount of this decrease corresponds to the gain measured in the Bode-diagram. Particularly for low frequencies

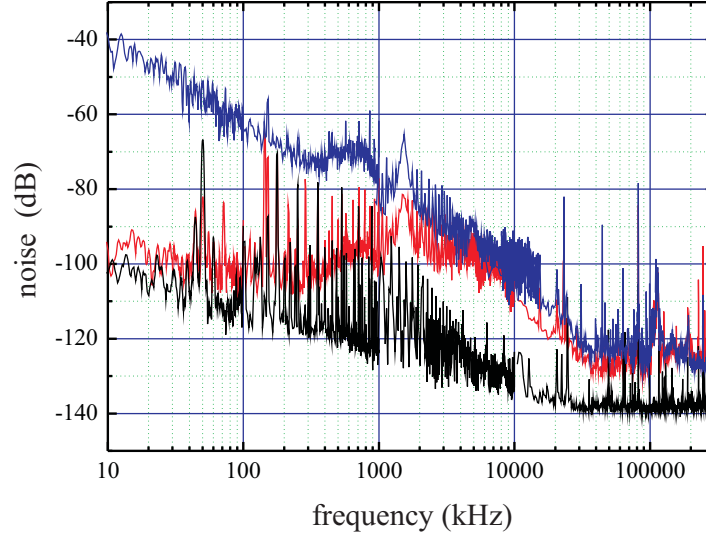


Figure 3.11: Noise measurement for a power stabilized Nd:YAG laser: The black, blue, and red lines indicate the noise of the amplified photodiode, the noise of the open loop system (photodiode and laser) and the noise of the closed servo loop, where the power is stabilized by the PI-controller, respectively.

the noise is considerably reduced, e.g. by 60 dB at 10 Hz. Above the bandwidth the unlocked and locked systems behave the same way. The resonance at 1.5 kHz is also suppressed but still visible. In the Bode-diagram it manifests itself as increased phase fluctuations at the resonance frequency. Two other dominant noise features in the Bode-diagram at 82 kHz and 240 kHz can be measured in the noise spectra. The origin of these resonances are unknown, we even detect them by an open BNC cable, however.

3.8 Absorption imaging

We obtain all information about the atomic system at the end of the experimental run by the well-known technique of absorption imaging [124]. This kind of imaging is based on Beer's law for light absorption and yields information about the number of atoms, the temperature of the cloud as well as the atomic density distribution at the time of imaging. A resonant laser beam passes through the atomic cloud casting a shadow of the cloud onto the chip of a CCD camera, thereby measuring the intensity distribution $I_T(x, y)$, integrated along the line-of-sight z . In order to determine the optical density, a second picture ($I_{\text{laser}}(x, y)$) of the laser beam without the cloud is required. Additionally, to eliminate ambient background light, a third picture ($I_b(x, y)$) without the laser beam is taken. From these images the column density distribution of the atomic cloud along

the line-of-sight can be obtained

$$n_z(x, y) = \frac{1}{\sigma} \frac{I_{\text{laser}}(x, y) - I_b(x, y)}{I_T(x, y) - I_b(x, y)}, \quad (3.17)$$

where σ denotes the scattering cross-section. Hence, for a CCD chip with $i \times j$ pixel and a surface A of each pixel the atom number is given by

$$N = \int \int n_z(x, y) dx dy \quad (3.18)$$

$$= \sum_{\text{Pixel}(i,j)} \frac{A}{f_m^2} n_z(i, j) \quad (3.19)$$

where f_m denotes the magnification of the imaging system.

Thermal cloud

The temperature of the thermal atomic cloud can be determined by a time-of-flight (TOF) measurement. Switching off the magnetic or dipole trap, the atomic cloud falls down due to gravity and expands ballistically. The density distribution after an expansion time t is given by

$$n(x, y, z, t) = \frac{1}{\lambda_{\text{dB}}^3} \prod_{i=1}^3 \sqrt{\frac{1}{1 + \omega_i^2 t^2}} g_{3/2} \left(e^{\left(\mu - \frac{m}{2} \sum_{i=1}^3 \left(\frac{x_i \omega_i}{1 + \omega_i^2 t^2} \right) \right) / k_B T} \right). \quad (3.20)$$

For $t \ll \omega_i^{-1}$, equation (3.20) describes the spatial density distribution inside the trap. When the TOF exceeds the inverse trap frequencies ω_i , the thermal cloud expands isotropically and mirrors the momentum distribution in the trap. For thermal clouds much larger than the critical temperature the density distribution is Gaussian and the temperature of the thermal cloud is given by

$$T = \frac{m}{2 k_B} \frac{\sigma_i^2 \omega_i^2}{1 + \omega_i^2 t^2}, \quad (3.21)$$

where σ_i denotes the $1/e^2$ -width of the Gaussian distribution along axis i .

Bose-Einstein condensate

The density distribution of a weakly interacting BEC trapped in a harmonic potential is described by the Thomas-Fermi distribution, explicitly given in equation (1.17) in section 1.2. The expansion during TOF of the BEC is independent of the temperature, as all condensed atoms occupy the motional ground state of the trap, but rather given by the mean field energy in a specific direction. Thus, the expansion is anisotropically for non-isotropic trap geometries ($\omega_{x,z} \gg \omega_y$), because the repulsive interaction between two atoms counteracts the force due to the trapping potential. Hence, the stronger the

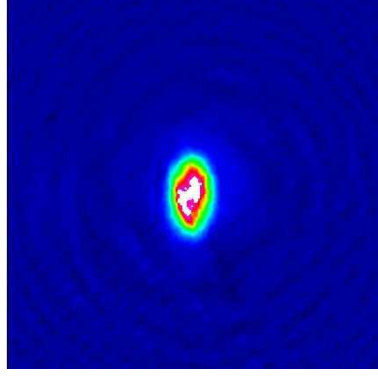


Figure 3.12: Absorption image of a BEC after a TOF of 25 ms. The horizontal axis corresponds to the axial direction of the QUIC trap. The vertical axis corresponds to the direction of gravity and to one of the radial directions of the trap.

confinement the larger the mean field energy. Therefore, the expansion along the radial axis with frequencies $\omega_{x,z}$ exceeds the axial one for TOFs larger than the inverse radial trap frequency. The Thomas-Fermi radii after a TOF time t are

$$R_{x,z}(t) = R_{x,z}(0) \sqrt{1 + (\omega_{x,z} t)^2} \quad (3.22)$$

$$R_y(t) = R_y(0) \left(1 + \left(\frac{\omega_y}{\omega_{x,z}} \right)^2 \left(\omega_{x,z} t \arctan(\omega_{x,z} t) - \frac{1}{2} \ln(1 + \omega_{x,z}^2 t^2) \right) \right) \quad (3.23)$$

Thus, the aspect ratio for times larger than the inverse radial trap frequency is reversed with respect to the cloud geometry inside the trap.

In our experiment a CCD camera from Apogee with a chip of 512×768 pixels and a pixel size of $9 \times 9 \mu\text{m}^2$ is employed. A $200 \mu\text{s}$ circular polarized, resonant laser pulse with a power of $200 \mu\text{W}$ images the atomic cloud through a lens system with a magnification of $f_m = 1.8$. A typical false-colour absorption image of a BEC after a TOF of 25 ms is shown in figure 3.12.

4 Single Cs atoms in a cold cloud of Rb atoms

Single Cs atoms immersed in a BEC can be used to resolve the dynamics of the quantum degenerated gas. This kind of experiment requires a controlled loading and trapping of single atoms as well as their detection. In most of the ultracold atoms and mixture experiments, a MOT is used to load between 10^7 to 10^9 atoms. The number of atoms can be determined by a simple fluorescence detection setup or by absorption imaging. For a single atom, the absorption image technique is not applicable, as intensity fluctuations of the probing laser exceed the absorption of one atom [125]. However, detecting the fluorescence of a single atom is possible [126], if several requirements are fulfilled. In the next two sections trapping of a single atom in a MOT and detecting its fluorescence are discussed. In the last section of this chapter we present our first imbalanced mixture experiment in which the dynamics of single Cs atoms in a MOT interacting with cold Rb atoms is investigated. The single Cs atom probe allows determining a precise value of the cold collision rate between Rb and Cs in a MOT.

4.1 Single Cs atom MOT

The total number of trapped atoms in a MOT depends on the loading rate, on the collision rate with atoms from the background gas and on the cold collision rate of trapped atoms. Hence, to trap only single atoms, the loading rate of the MOT has to be reduced significantly from about 10^9 /s of a standard MOT to about 1/s. The loading and collision rates are determined by the magnetic field gradient dB/dz , the partial background pressure n_i , and parameters of the laser beams, such as beam waist r_i , detuning Δ_i from the resonance, and intensity.

The dependence of the loading rate R_i on the abovementioned parameters is given by [127, 126]

$$R_i \propto n_i S_i \bar{v}_i \left(\frac{v_{\text{cap},i}}{\bar{v}_i} \right)^4, \quad (4.1)$$

where S_i , \bar{v}_i , and $v_{\text{cap},i}$ denote the surface of the irradiated volume, the mean velocity of species i in the background gas, and the capture velocity, respectively. The maximum capture radius $r_{\text{cap,max}} \propto |\Delta_i/(dB/dz)|$ determines the upper limit of the surface to be $S_i = 4\pi r_{\text{cap,max}}^2$. If $r_i < r_{\text{cap,max}}$ the surface of the capture volume $S_i \propto r_i^2$ increases

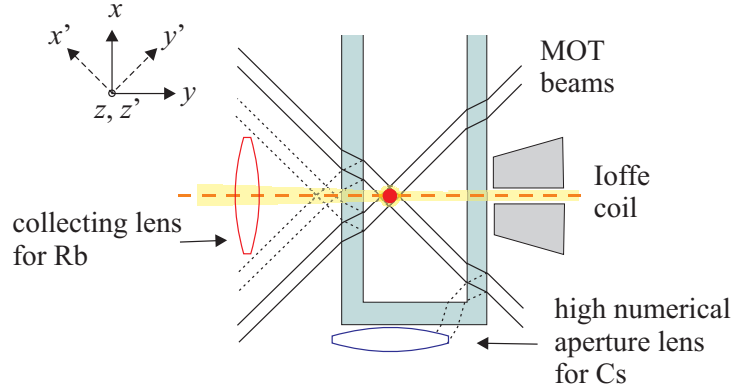


Figure 4.1: Schematic of the experimental setup to trap and detect single atoms: The MOT position in the glass cell (light blue) is marked by a red dot. Two MOT beams along the x' - and y' -axis are indicated with black solid lines. Additionally, some critical first order reflections (dotted black lines) on the glass cell are drawn. The third MOT beam is aligned along the z -axis. The high numerical aperture objective for Cs (blue lens) and the collecting lens for Rb (red lens) are located below and on the Ioffe axis, respectively. The Ioffe coil is indicated in grey. The dipole trap beam runs along the y - and z -axes.

quadratically with the beam waist. Since in the limit of $r_i > r_{\text{cap,max}}$ we have $v_{\text{cap},i} \propto (dB/dz)^{-2/3}$ and $S_i \propto (dB/dz)^{-2}$, the strongest dependence of R_i is on the magnetic field gradient and it scales as [128]

$$R_i \propto \left(\frac{dB}{dz} \right)^{-14/3}. \quad (4.2)$$

Hence, a high magnetic field gradient of 300 G/cm, which is one order of magnitude larger than in a standard MOT (10 G/cm), is chosen for our measurements, reducing the loading rate by seven orders of magnitude with respect to common traps. This is supplemented by a low partial Cs background pressure. Standard MOTs are operated either as vapour cell MOTs with a partial background pressure of about 10^{-9} mbar or as UHV-MOTs loaded from an atomic beam. In our experiment, a low partial Cs background pressure of much less than 10^{-11} mbar is achieved by a MOT loading from the background of the UHV region. The third parameter differing from the standard MOT is the laser beam radius. It is chosen to be about 1 mm which is one order of magnitude lower than in the standard MOT setup in order to reduce the capture range and therefore the loading rate. Additionally, the laser beam power is reduced to $100 \mu\text{W}$ per beam corresponding to an intensity of 4.5 mW/cm^2 which is comparable to the intensity in a standard MOT. Combining all these parameters results in a loading rate of about 1 atom/s.

During the experimental run a single Cs atom will be loaded when a BEC is already present. In the doubly polarized state the lifetime of the BEC is about 1 s. Thus, in the aforementioned trapping configuration the loading time of single atoms is of the same

order of magnitude, which is not favourable to work with. To overcome this challenge, the loading sequence is optimized and composed of a short low gradient loading and high gradient storage stage [129]. In the first stage, the magnetic quadrupole field is ramped up to a gradient of 110 G/cm. Once the magnetic field has reached this relatively low gradient value, the laser light is switched on. Here, the loading rate is 170-fold increased compared to the rate at the final magnetic field gradient of 300 G/cm. After 20 ms the magnetic field is ramped up to its final value in about 20 ms in order to enhance the confinement and prevent further loading. The mean number of atoms stored after this sequence can be chosen by adjusting the loading time at the low magnetic field gradient. Besides, the large magnetic field gradient also reduces the maximum diameter of the MOT volume to about $30 \mu\text{m}$. In comparison, the extension of a BEC in the dipole trap configuration used in our experiment is about $(7 \times 10 \times 10) \mu\text{m}^3$. To investigate the interaction of a Rb BEC with a Cs atom, the spatial overlap of the MOT volume with the Rb BEC volume is supposed to be as large as possible. Hence, a better localization of the single atom, e.g. by reducing the MOT volume, is advantageous.

4.2 Fluorescence of single Cs atoms

The challenge of detecting a single neutral atom in a MOT becomes apparent if the photon scattering rate Γ_{sc} of the atom trapped in a MOT is considered. For typical single atom MOT parameters, see above, each Cs atom scatters about $1.6 \cdot 10^7$ photons/s corresponding to an optical power of 3.8 pW. For comparison the power of each MOT laser beam used in our trap is about $100 \mu\text{W}$. Even reflections of 4% of the MOT beams at the glass cell walls exceed the fluorescence power of one atom by 6 orders of magnitude.

To probe this extremely low fluorescence level, a very sensitive avalanche photodiode (SPCM-AQRH-12FC from PerkinElmer) with a quantum efficiency of 42% at 852 nm and a low dark count rate of 500 Hz is used. The damage threshold of the so-called Single-Photon-Counting-Module (SPCM) is specified to be at a photon count rate of 30 MHz. This shows the importance of removing any stray and ambient light to ensure a reliable operation of the SPCM even for more than one atom loaded. Thus, our demand on the detection system is to concurrently collect a maximum amount of the atomic fluorescence and as few background light as possible, thereby optimizing the signal to noise ratio. This ratio is mainly limited by a small solid angle from which the fluorescence light can be detected. Our fluorescence detection setup is positioned below the glass cell (figure 4.1). This position offers a good optical access and it is at the same time compatible with the already existing experimental setup. The MOT centre is 3 cm above the bottom of the cell. The fluorescence light is collected by a high numerical aperture objective (NA=0.29) at a working distance of 42 mm with respect to the MOT position. This results in a solid angle of 0.084π .

Figure 4.2 shows a schematic of the detection setup including all different components. The task of this optical setup is to efficiently collect the atomic fluorescence and to guide it to the SPCM, while stray light is suppressed by several orders of magnitude

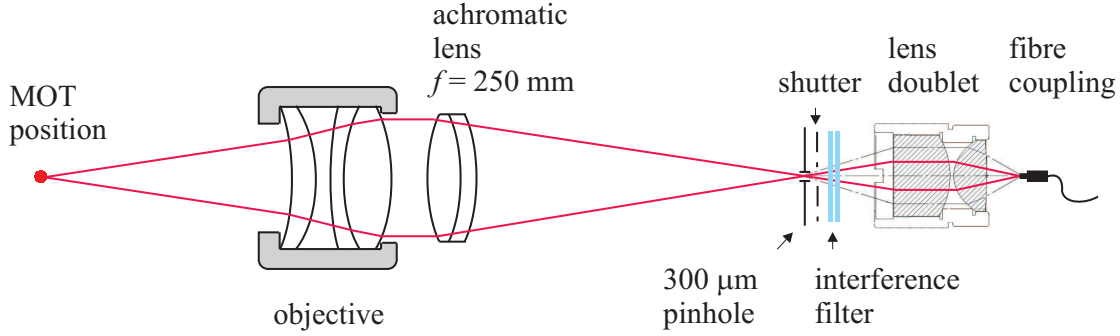
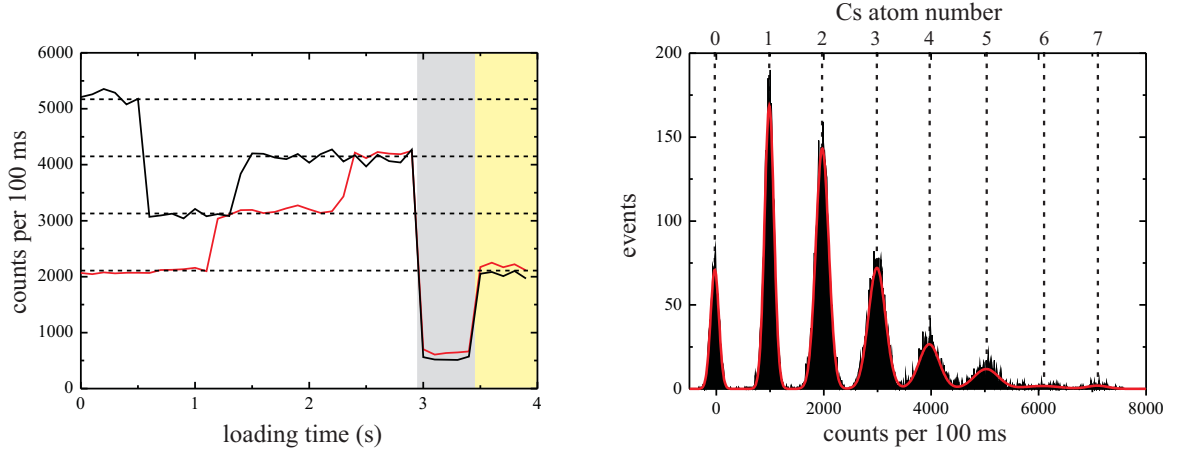


Figure 4.2: Fluorescence detection setup to probe single Cs atoms. A high numerical aperture objective collects 2.1% of the Cs fluorescence light. A pinhole and two interference filters remove the stray and ambient light from the detected signal.

using a combination of spatial and spectral filters. Details and analysis of the optical properties of each component used in the setup can be found in the diploma thesis of Tatjana Weikum [130]. The collected fluorescence light is focused by an achromatic lens ($f = 250$ mm) into a $300 \mu\text{m}$ pinhole to spatially filter stray light, occurring, e.g., due to back reflections at the glass cell, which is not propagating on the optical axis of the imaging system. Small MOT beams as used for single atom MOTs support the suppression of stray light by reflections. Behind the pinhole two interference filters (FF01-832/37-25 from Semrock: transmission $T \geq 93\%$ at 852 nm and an optical density of 10^7 (10^6) at 780 nm (1064 nm) each) remove the Rb laser and fluorescence light, as well as residual ambient light and the stray light of the dipole trap beams propagating along the optical axis, from the spectrum. As the Rb-Pusher beam with a power of $700 \mu\text{W}$ propagates along the imaging axis, two edge filters are necessary to protect the SPCM by suppressing the Rb photon count rate by 14 orders of magnitude from initially about 10^{15} photons/s. In addition, a small shutter from a common digital camera is inserted to mechanically interrupt the optical path in the sequence during the preparation of the BEC. Behind the interference filters, the divergent fluorescence light is focused using an aspherical lens doublet (C230260P-B) into a multimode fibre ($50 \mu\text{m}$ core radius) guiding the fluorescence light to the fibre coupled SPCM. The entire optical setup is surrounded by a tube system to shield the detection system from any kind of stray and ambient light. About 60% of the initially collected fluorescence light reach the SPCM after passing through all components. Due to the quantum efficiency of 42% of the SPCM the estimated detected photon rate for one atom is about 80 kHz. In the SPCM, each detected photon produces a TTL pulse. These pulses are detected by a counter card (NI 6023 E from National Instruments) and are binned in time intervals of 10 to 100 ms depending on the measurement.

Figure 4.3(a) shows two typical fluorescence signals recorded by our detection system. A step function can be observed in which each step corresponds to one atom. As each atom scatters, on average, the same amount of photons, the step size is constant. Here, the four equidistant dashed lines indicate the discrete steps corresponding to zero to



(a) Two typical fluorescence signals of single atoms loaded in a high gradient MOT. The detected pulses are binned in time intervals of 100 ms. After a detection time of 3 s the cooling light is switched off, followed by ramping down the magnetic field 100 ms later (grey range). During the last 500 ms all MOT beams are switched on again to determine the background light (yellow range). The horizontal dashed lines indicate the fluorescence step belonging to (from bottom to top) background, one, two and three atoms. After a detection time of 500 ms the black trace shows a two-atom loss event.

(b) Histogram of 499 fluorescence traces shown in (a). The red lines are Gaussian fits to the 8 peaks belonging to Cs atom numbers from 0 to 7, respectively. The vertical dashed lines indicate the Cs atom number assigned to the peaks.

Figure 4.3: Detection of single atoms in a MOT.

three atoms, where a binning time of 100 ms is chosen. Therefore, the count rate per atom can be deduced to be 10 kHz. The discrepancy between the theoretically expected count rates and the measured ones can be mainly attributed to a non perfect alignment of the imaging optic, including the fibre coupling. In particular, the position of the high numerical objective along the optical axis is critical. A deviation of its position from the optimal working distance results in an increased spot size at the position of the pinhole.

The experimental sequence for the traces as shown in figure 4.3(a) starts with loading atoms in a shallow MOT for 20 ms, followed by ramping up the magnetic field gradient in 20 ms to 300 G/cm, as described in section 4.1. After a 3 s high gradient magnetic field stage the cooling light is switched off by an AOM, followed by switching off the magnetic field 10 ms later. The background scattering light due to the MOT laser (cooling and repumping laser) in addition to the dark count rate is inferred from the last 500 ms of the detected traces, when both lasers are on again. This yields a typical background light level of about 20 kHz.

Besides the loading of atoms also a two-atom loss event is observed in figure 4.3(a). This loss process is attributed to a cold collision, dealt with in the next section.

Figure 4.3(b) shows a histogram of 499 traces as shown in figure 4.3(a). For each data

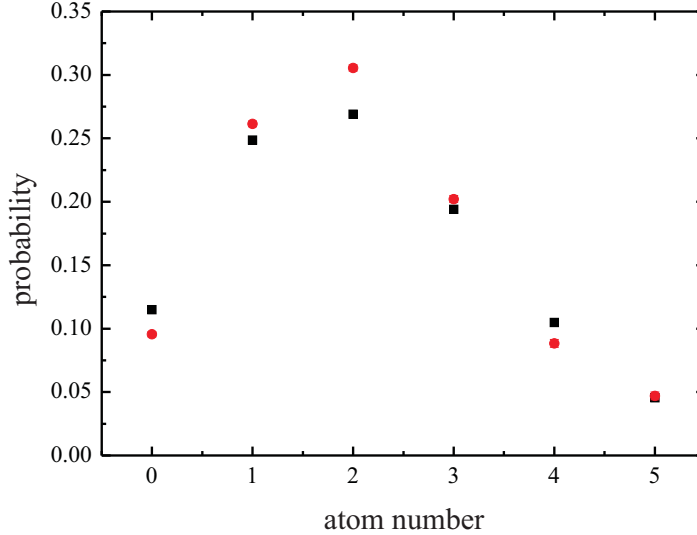


Figure 4.4: Poissonian distribution corresponding to the histogram of figure 4.3(b): The experimentally measured probability distribution (red dots) is compared with the theoretical Poissonian distribution (black squares) for an expectation value of 2.15 ± 0.09 . The statistical error for the measured probability is below the resolution of the graph.

set the background rate has been subtracted separately to eliminate long time drifts. Each peak can be attributed to an atom number N indicated by the vertical dashed lines. Up to 6 peaks can be clearly distinguished. The probability distribution of the detected number of atoms is described by a Poissonian function

$$P(N) = \frac{\lambda^N}{N!} e^{-\lambda}, \quad (4.3)$$

describing a distribution with discrete events N and large repetition rates. The Poissonian distribution for the histogram in figure 4.3(b) is plotted in figure 4.4. The expectation value λ is calculated to be 2.15 ± 0.09 and the corresponding theoretical distribution is plotted for comparison. The desired expectation value of the Poissonian can be experimentally adjusted by changing the loading time and the magnetic field gradient of the shallow trap stage. Additionally, the detuning of the cooling laser light during the shallow trap stage as well as during the high gradient trap stage affects the distribution. However, the detuning during the detection time also has an effect on the count rate per atom. Hence, the detuning is optimized to yield a large scattering rate, whereas the first stage of the experimental run (shallow trap) is used to adjust the expectation value.

Shot noise limit

The count rate for each peak is Poissonian distributed, too. However, for the large expectation values of the Poissonian of the order of 2000 counts/100 ms, it can be well

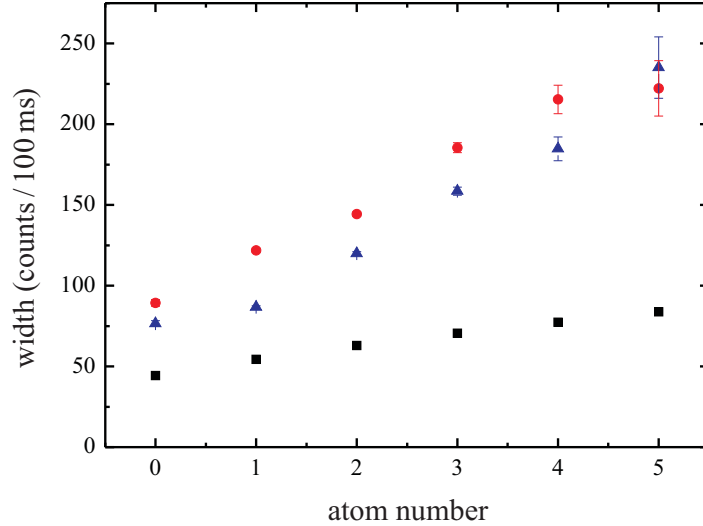


Figure 4.5: Width of the count rate distribution in comparison with the shot noise as a function of the atom number: The shot noise limit is plotted as black squares. The red dots indicate the measured standard deviation of the raw data. The blue triangles correspond to the width of the peak after subtracting the background from each trace, independently.

described by a Gaussian function. The width of the peak should be as small as possible to ensure that neighbouring peaks do not overlap, and thus to enable the distinction of the number of trapped atoms. The lower limit is given by the shot noise occurring due to statistical fluctuations of the light field. The shot noise is proportional to $\sqrt{N_{\text{Photon}}}$, where N_{Photon} is the average count rate of the considered peak. In figure 4.5 the shot noise and the standard deviation for each peak of the histogram are plotted. A clear deviation of the experimentally measured widths and the theoretical lower limit can be observed. To distinguish between short- and long-term drifts the noise of the raw data is compared to the background adjusted values. For zero and for a low number of atoms the measured width is thereby reduced by about 25%. This fraction of the noise is caused by long-term instabilities of the laser power. The measured background fluctuations are about 5% within 5 min, whereas a measurement of 500 experimental runs including the cooling time for the magnetic coils takes 30 min. This drift of the background light can also be observed in figure 4.3(a) between the two traces during the last 500 ms. It arises because of polarization changes of the MOT light while passing through the fibre resulting in power fluctuations due to a PBS after the fibre. The residual deviation from the shot noise limit for no atoms loaded can be attributed to short time power instabilities changing the amount of stray light. For an increasing number of atoms, the discrepancy between the measured noise and the shot noise limit grows as the power instabilities result not only in stray light variations but also in a fluctuating photon scattering rate per atom.

The main contribution (45%) to the background light is given by the stray light of beam $-x'$ (figure 4.1). Each beam separately shows the same fraction of noise as the measured width of the peak corresponding to no atoms (figure 4.3(b)). In order to approach the shot noise limit, the power of the cooling and the repumping light can be actively stabilized using the power stabilization setup of the dipole trap beams explained in section 3.7.1. This would allow to shorten the binning time without losing information about the trapped atom number. In addition, interferences between counter-propagating or orthogonally oriented beams can occur in each MOT. Even if in one dimension there are no interferences, due to the orthogonal polarization of the counter-propagating MOT-beams, the situation changes in the complex case of three dimensions [131]. Then atoms can jump between the maxima of the interference pattern. The interference can be omitted by wiggling one mirror in each beam with different modulation frequencies using piezoelectric stacks. Thereby, the fixed phase relation of the MOT beams is disturbed. This decreases the standard deviation of each peak by about 5%.

Furthermore, the fluctuations in the count rate can be reduced by a stronger confinement of the single atom in the MOT: The constructed detection setup offers a field of view of $60\ \mu\text{m}$ given by the magnification factor of 5 of the imaging system in combination with the $300\ \mu\text{m}$ pinhole. In comparison, the maximum MOT diameter was determined in section 4.1 to be $30\ \mu\text{m}$. Thus the alignment of the detection setup with respect to the MOT is critical. Short-time or day-to-day variations of the MOT beam power balancing, resulting in position changes of the trap centre, may lead to a non-centred image of the MOT at the pinhole. Thereby, the atom oscillating in the trap may temporarily leave the field of view causing count rate fluctuations. Decreasing the MOT volume the detection setup is less prone to the MOT alignment and the count rate is more stable. To reduce the MOT volume the magnetic field gradient can be increased. In our setup the maximum magnetic field of 300 G which can be applied is limited by the power consumption of approximately 300 W of the coil system.

4.3 Cold collisions

The lifetime of a single atom in a MOT is determined by the collision rate with the background gas. For a background pressure of 10^{-11} mbar the lifetime is up to 100 s. For more than one atom, inelastic collisions can take place, where two atoms simultaneously leave the trap. The black graph in figure 4.3(a) shows such a two atom loss after a detection time of 500 ms. The rate of these inelastic collisions depends quadratically on the number of trapped Cs atoms. These so-called cold collisions are discussed in detail in several review articles [132, 133] and have already been analyzed in a single Cs atom MOT in reference [134]. However, this kind of inelastic collisions can also take place as heteronuclear collisions. In the next section, the inter-species collision rate of Rb and Cs is investigated in a strongly imbalanced Rb-Cs mixture. Before, I will introduce the origin of inelastic cold collisions in a MOT.

These inelastic cold collisions can be differentiated into ground state and light-induced

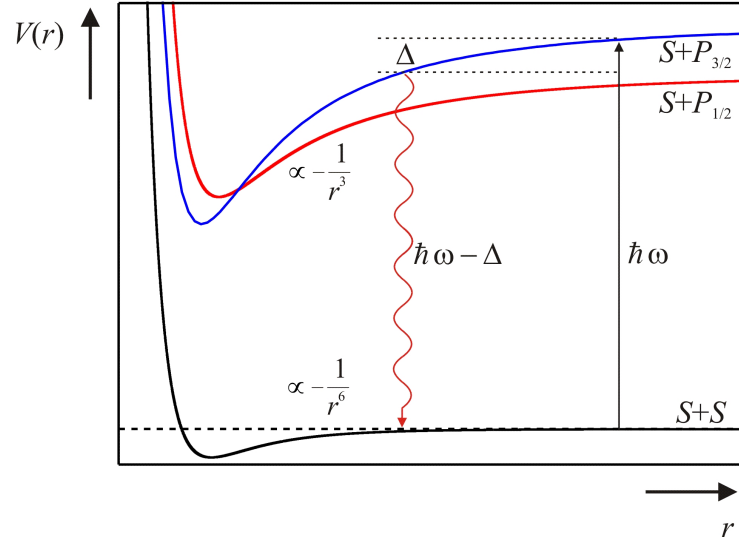


Figure 4.6: Schematic of the molecular potentials corresponding to ground state and light-induced collisions for alkalis.

collisions. The first class of collisions is not limited to MOTs but is also present in pure magnetic traps. Here, the dominating processes are hyperfine state changing collisions occurring due to the spin exchange or dipolar relaxation interactions. Both of them are explained in detail in chapter 2. Therefore, only light-induced collisions are discussed here.

We assume two colliding alkali atoms such as Rb and Cs trapped in a MOT. Figure 4.6 schematically shows three molecular potentials corresponding to ground state collisions ($S + S$) and light-induced collisions ($S + P_{1/2}$ and $S + P_{3/2}$), where the ground state and the two excited states of the D1- and D2-lines are denoted with S , $P_{1/2}$ and $P_{3/2}$, respectively. Driving the D2-transition by resonant laser light with a frequency ω , an atom can be excited to the $P_{3/2}$ -state. Simultaneously, a collision between this atom and a ground state atom can take place. The homonuclear molecular potential for these excited states is characterized by a long-range interaction potential scaling with $-C_3/r^3$ occurring due to dipole-dipole interaction. The quasi-molecules are accelerated by this attractive potential towards the potential minimum leading to a decreasing internuclear distance of the atom pair.

If the collision time exceeds the spontaneous decay time, the quasi-molecule can relax to the $S + S$ ground state by emitting a photon with energy $\hbar\omega - \Delta$, which is red detuned with respect to the excitation photon. Here Δ denotes the potential difference between the potential energy during the excitation and the one during the de-excitation. The amount of Δ is converted to kinetic energy and shared between the colliding atoms according to their mass ratio. This exoergic process is called radiative escape [135]. Depending on the absolute value of Δ , it results either in heating, if the capture velocity is larger than the velocity of the atoms, or in trap loss.

Quasi-molecules can reach the short range potential, if they do not relax into the ground state during the collision time. Here they can undergo a change in fine structure due to the intersection of the molecular potentials $S + P_{1/2}$ and $S + P_{3/2}$, and leave the short-range interaction region. The energy difference corresponding to the fine splitting is also converted into kinetic energy. For Cs (Rb) the D1 and D2-lines differ by 17 THz (7 THz) in frequency corresponding to a kinetic energy of $k_B \cdot 800$ K ($k_B \cdot 340$ K), shared between the colliding atoms according to their mass ratio. In any event, this collision process changing the fine structure results in a loss of atoms. These cold collisions were theoretically modelled for the first time by [136]. The homonuclear loss rate constants for Rb and Cs are determined to be $\beta_{\text{Rb}} = 1.2 \cdot 10^{-11}$ cm³/s and $\beta_{\text{Cs}} = 5 \cdot 10^{-12}$ cm³/s, respectively [137].

4.4 Single Cs atoms in the presence of Rb

In a first experiment we use single Cs atoms in a MOT to probe a Rb MOT. Information is deduced from the dynamics of the Cs atoms detected through the fluorescence signal. I have determined the inter-species coefficient for heteronuclear cold collisions in an imbalanced Rb-Cs-MOT thereof.

For these experiments both species have to be trapped simultaneously. To ensure a low loading rate and trapping of only single Cs atoms, a high gradient MOT is required as explained in section 4.1. This implies that also Rb has to be stored in a high gradient magnetic field. Hence, the number of Rb atoms is reduced with respect to standard MOTs. However, the number of trapped atoms of the two species can differ by one to three orders of magnitude, the final magnetic field gradient being the same, though.

Using equation (4.1) the following parameters are adjusted to operate the Rb and Cs high gradient MOTs in two different regimes of the atom number: For the Rb MOT the radius r_{Rb} is 7 times larger than in the case of a single Cs atom MOT, increasing the loading rate by a factor of about 50. In addition, the Rb-UHV MOT is loaded by transferring atoms from a vapour cell MOT (chapter 3). This atomic beam provides precooled Rb atoms ($\bar{v}_{\text{Rb}} < \bar{v}_{\text{Cs}}$) and a local enhancement of the Rb atomic density ($n_{\text{Rb}} > n_{\text{Cs}}$). Hence, the loading rate as well as the equilibrium Rb atom number can be adjusted by changing the atomic flux. Experimentally, it can be realized by changing the power and detuning of the MOT beams of the vapour cell MOT. As a trade-off, during the experimental run, the final magnetic field gradient is chosen to be 270 G/cm, which allows trapping and probing single atoms by adjusting the detuning of the cooling laser light with respect to the cycling transition, but at the same time increases the loading rate of the Rb atoms.

4.4.1 Determination of the number of Rb atoms

Detection of atom numbers down to several tens of atoms cannot be realized by standard photodiodes. Instead, we use an APD (C30902EH from PerkinElmer, responsivity $Res_{APD} = 40 \text{ A/W}$) operated below the breakdown voltage. Assuming 50 Rb atoms, trapped in the MOT, the fluorescence power can be estimated to be approximately 240 pW. The only optical access available for detection of the atoms is along the Ioffe axis (y -axis in figure 4.1), as for these experiments neither optical pumping light nor the dipole trap beams are used. A convex lens with a focal length of 40 mm is chosen to collect the fluorescence light. The resulting solid angle Ω is calculated to be 0.056π reducing the detected fluorescence of 50 atoms to 3.4 pW. This corresponds to 1.4% of the entire fluorescence power. An interference filter for 780 nm (transmission $T_{IF}=90\%$ at 780 nm) removes the ambient light as well as the Cs fluorescence light. A lens doublet (F810FC-780 from Thorlabs) with a focal length of 35.9 mm couples the fluorescence light into a multi-mode fibre with a numerical aperture of $NA=0.29$. Afterwards, the light is focused by an aspheric lens pair (C230220P-B from Thorlabs) on a 0.2 mm^2 chip of the APD, followed by a transimpedance amplifier. The quantum efficiency QE of the APD is specified to be 77%. In order to increase the output voltage a transimpedance resistor R_{TI} of as large as $10 \text{ M}\Omega$ is chosen. Afterwards the signal is again amplified by a factor of $G = 22$. To suppress high-frequency noise caused by the electronics used, the signal is low-pass filtered by inserting a RC-filter with a cutoff-frequency of 10 Hz which considerably improves the signal to noise ratio.

The number N_{Rb} of Rb atoms is given by

$$N_{Rb} = \frac{P_{MOT}}{P_{Rb}}, \quad (4.4)$$

where P_{MOT} denotes the fluorescence light of a MOT with N_{Rb} atoms and $P_{Rb} = \hbar\omega \Gamma_{Rb}/2$ is the fluorescence power of one atom, assuming a saturation parameter much larger than unity, which can be assumed for MOTs [138]. The MOT fluorescence P_{MOT} is proportional to the detected voltage U_{det} taking into account the following corrections

$$P_{MOT} = \frac{U_{det}}{\Omega_{eff} \cdot T_{IF} \cdot T_{fibre} \cdot G \cdot R_{TI} \cdot Res_{APD} \cdot QE \cdot (1 - L)}. \quad (4.5)$$

Here, Ω_{eff} is defined as the effective solid angle considering the numerical apertures of the lenses and the fibre, and L denotes the entire loss at the optics used. The correction factor L includes the reflectivity of the optical surfaces and the absorption. Thus, an

Ω_{eff}	T_{IF}	T_{fibre}	G	R_{TI}	Res_{APD}	QE	L
8‰	90 %	60 %	22	10 M Ω	40 A/W	77 %	33 %

Table 4.1: The correction factors included in equation (4.5) are listed.

4 Single Cs atoms in a cold cloud of Rb atoms

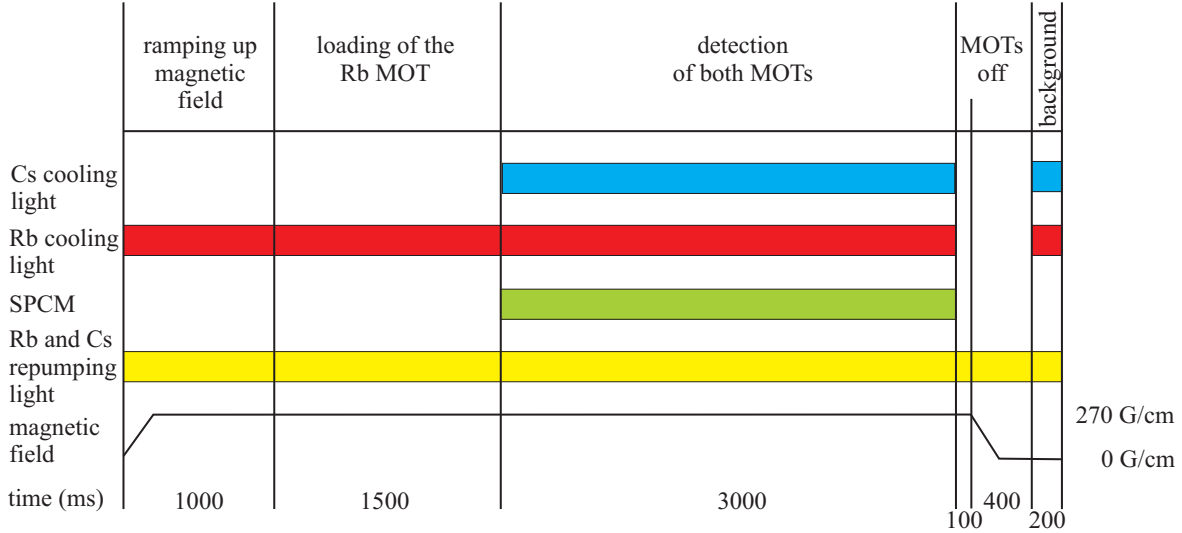


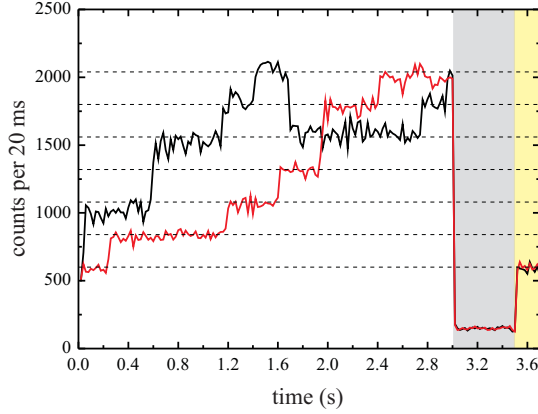
Figure 4.7: Experimental sequence to load an imbalanced Rb-Cs-MOT. The blue, red, yellow, and green bars indicate the Cs and Rb cooling light, the repumping light of both MOTs, and the SPCM detection time, respectively. The black solid line shows the time evolution of the magnetic field.

output voltage $U_{\text{det}} = 1 \text{ V}$ corresponds to an atom number of $N_{\text{Rb}} = 11000$. The main uncertainty of this relation is given by the responsivity of the APD, which depends non-linearly on the operating voltage and on the fibre coupling efficiency T_{fibre} , which is only estimated to be 60%. Therefore, the total atom number is only precise to a factor of 2, however, the fluctuation of the *relative* atom number is less than 2%.

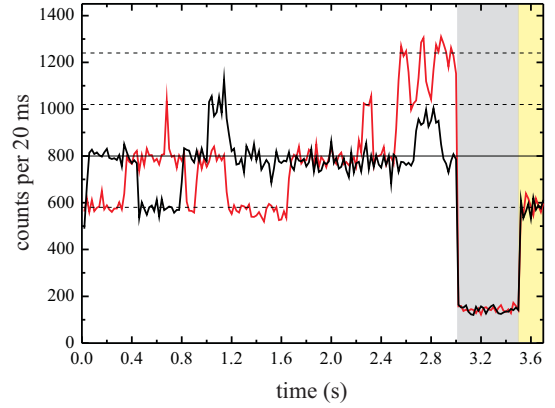
4.4.2 Experimental sequence

The detailed experimental sequence to load an imbalanced Rb-Cs-MOT is schematically drawn in figure 4.7. Initially, the magnetic field is ramped up within 8 ms to the final gradient of 270 G/cm. The Rb-MOT is loaded for 2.5 s by the atomic beam from the vapour cell MOT. Afterwards the Cs cooling laser light is switched on by means of an AOM. Simultaneously, the detection of the single Cs atoms by the SPCM is started and the fluorescence is recorded for 3 s. Then, the cooling light of both MOTs is switched off and 100 ms later the magnetic field is lowered to zero. Here, all atoms are lost. Switching on the cooling light at the end of the sequence allows to determine the background light (stray and ambient light) for each trace separately. The repumping light for both MOTs and the Rb atomic beam is present during the entire sequence. The latter one ensures a constant number of trapped Rb atoms.

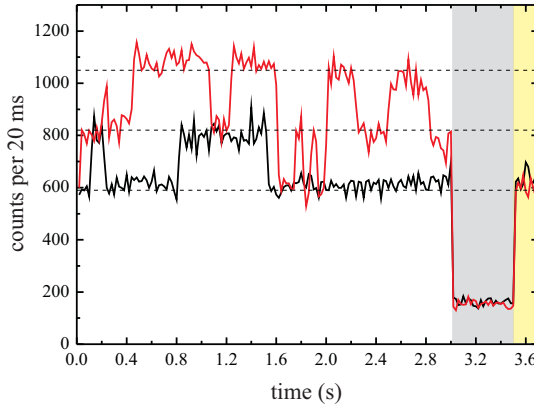
The D2-lines of the two species are separated by 72 nm. Investigating the influence of the laser beams on the non-resonant species we have observed that the laser light does not affect the non-resonant species.



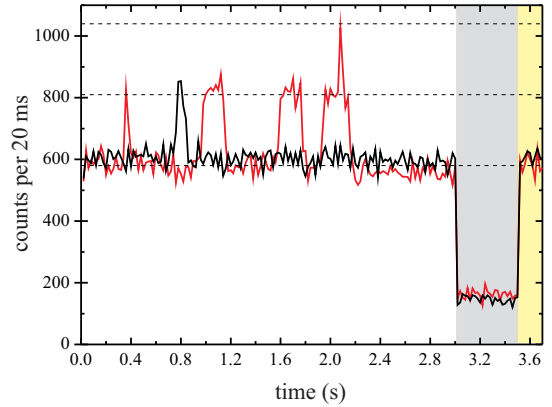
(a) Two typical Cs fluorescence signals (red and black solid lines) in the presence of about 110 Rb atoms.



(b) Two typical Cs fluorescence signals (red and black solid lines) in the presence of about 1200 Rb atoms.



(c) Two typical Cs fluorescence signals (red and black solid lines) in the presence of about 2300 Rb atoms.



(d) Two typical Cs fluorescence signals (red and black solid lines) in the presence of about 3000 Rb atoms.

Figure 4.8: Fluorescence signals of single atoms loaded in a high gradient MOT for four different numbers of Rb atoms: The detected pulses are binned in time intervals of 20 ms. Within the grey region, the cooling light and the magnetic field are switched off. During the last 200 ms all MOT beams are switched on again to determine the background light level (yellow range). The horizontal dashed lines indicate the fluorescence steps, each corresponding to one additional atom. Note the different scale.

4.4.3 Dynamics in the single Cs atom MOT in the presence of Rb

Cs fluorescence traces have been recorded for Rb atom numbers in the range of 0 and 3300 Rb atoms, where the Rb atom number was determined by equation (4.4) and (4.5). All data are sorted by N_{Rb} , which is binned in steps of 220 Rb atoms. Different dynamics of the single Cs atom MOT can already be seen in the single recorded traces. An example of two typical traces for four different Rb atom numbers is plotted in figure 4.8. For an

4 Single Cs atoms in a cold cloud of Rb atoms

almost negligible Rb atom number (figure 4.8(a)) a fast loading of Cs can be observed with only few loss features. In contrast, only a few loading events can be found for large Rb atom numbers (figure 4.8(d)). Moreover, loss processes are much more frequent and dominated by single-Cs collisions. All the loading events are followed, within 100 ms, by an atom loss. Within this range of the Rb atom number many traces do not show an event at all. The dynamics of the single Cs atom MOT in the presence of Rb can be described by the following rate equation

$$\frac{dN_{\text{Cs}}}{dt} = R(N_{\text{Rb}}) - \gamma N_{\text{Cs}} - \beta_{\text{RbCs}} \int n_{\text{Rb}}(r, t) n_{\text{Cs}}(r, t) d^3r, \quad (4.6)$$

where γ , β_{RbCs} and $R(N_{\text{Rb}})$ denote the background collision rate of Cs, the inelastic inter-species collision rate constant, and the loading rate of Cs as a function of the Rb atom number, respectively. Cs-Cs collisions leading to a simultaneous loss of two Cs atoms rarely occur due to the low Cs density. In particular, the probability of Cs-Cs collisions is proportional to N_{Cs}^2 . Thus, the more Rb atoms the less Cs-Cs collision events, as the Cs atom number decreases with the number of Rb atoms increasing. An event as shown in figure 4.8(a) is one of the very few observed ones. Therefore, Cs-Cs collisions can be neglected. The density distributions of the two clouds are given by

$$n_{\text{Cs}}(r, t) = n_{\text{Cs}}^0(t) \cdot e^{-\frac{r^2}{w^2}}, \quad (4.7)$$

$$n_{\text{Rb}}(r, t) = n_{\text{Rb}}^0(t) \cdot e^{-\frac{r^2}{(4w)^2}}, \quad (4.8)$$

here, w being defined as the $1/e$ -radius of the Cs-cloud. For Rb the size of the cloud is four times larger, mainly due to the larger MOT beam size and the different cooling light detuning. The peak densities can be calculated to be

$$n_{\text{Cs}}^0(t) = \frac{N_{\text{Cs}}(t)}{\pi^{3/2} w^3}, \quad (4.9)$$

$$n_{\text{Rb}}^0(t) = \frac{N_{\text{Rb}}}{64 \pi^{3/2} w^3}. \quad (4.10)$$

Here, the Rb atom number is assumed to be time-independent. Single Cs atoms do not affect the Rb cloud with several hundred Rb atoms. However, Rb-Rb cold collisions and collisions with background particles limit the lifetime of the Rb MOT, thereby reducing the Rb atom number, if there is no reloading. Experimentally an equilibrium between the loading and the loss rate is achieved by continuously loading the Rb-MOT using the atomic beam from the vapour-cell MOT, to make the total Rb atom number to remain constant. After integrating the last term in equation (4.6) the rate equation can be rewritten as

$$\frac{dN_{\text{Cs}}}{dt} = R(N_{\text{Rb}}) - \gamma N_{\text{Cs}}(t) - \beta_{\text{RbCs}} \frac{N_{\text{Rb}} N_{\text{Cs}}(t)}{(17 \pi)^{3/2} w^3}. \quad (4.11)$$

In order to determine the first term, the loading rate of the detected traces is plotted as a function of the Rb atom number. Figure 4.9 shows a linearly decreasing loading

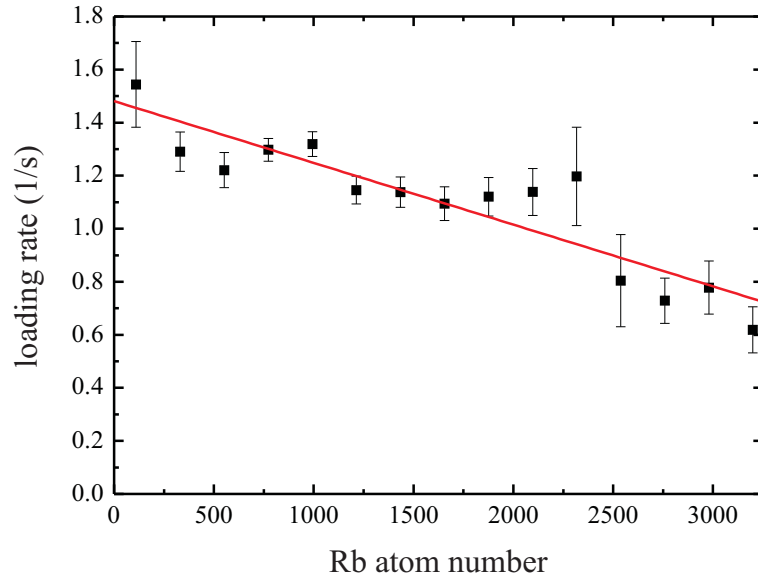


Figure 4.9: The loading rate of Cs as a function of the Rb atom number. The red line is a linear fit to the data yielding $R_0 = (1.48 \pm 0.06) \text{ s}^{-1}$ and $\alpha = (2.3 \pm 0.3) \cdot 10^{-4} \text{ s}^{-1}$ corresponding to equation (4.12).

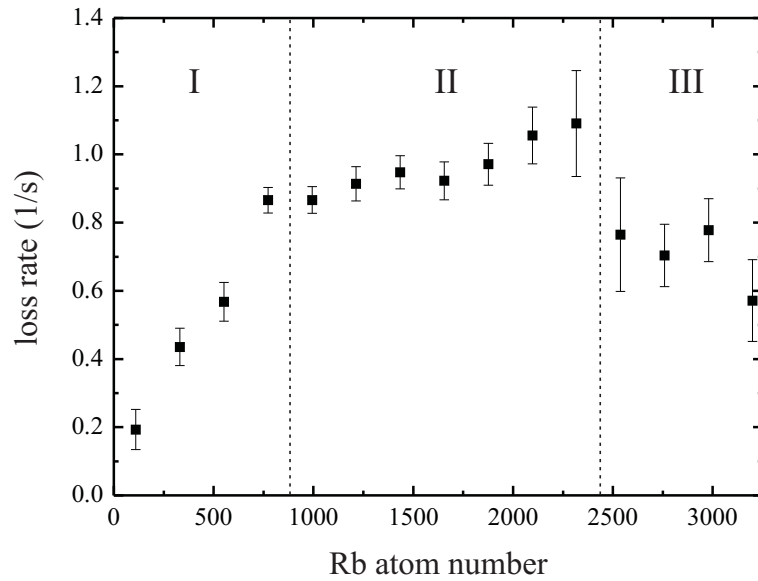


Figure 4.10: The loss rate of Cs as a function of the Rb atom number. The vertical dashed lines divide the graph into three sections. Section I, II and III denote the regions with increasing, constant and decreasing loss rate. Details are explained in the text.

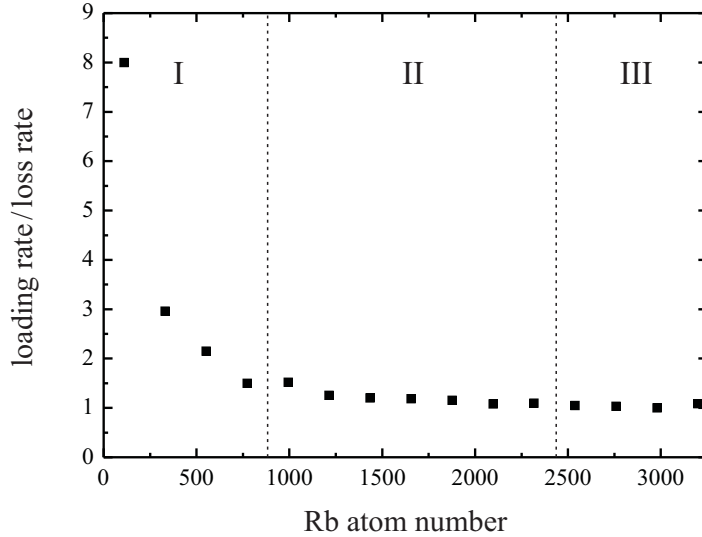


Figure 4.11: The ratio of the loading and loss rate of Cs as a function of the Rb atom number. According to figure 4.10 the vertical dashed lines divide the graph in three sections.

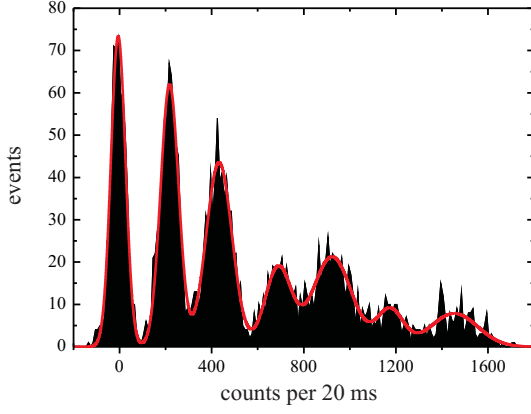
rate for an increasing number of Rb atoms. Hence, the loading rate R can be written as a function of the Rb atom number

$$R(N_{\text{Rb}}) = R_0 - \alpha N_{\text{Rb}}. \quad (4.12)$$

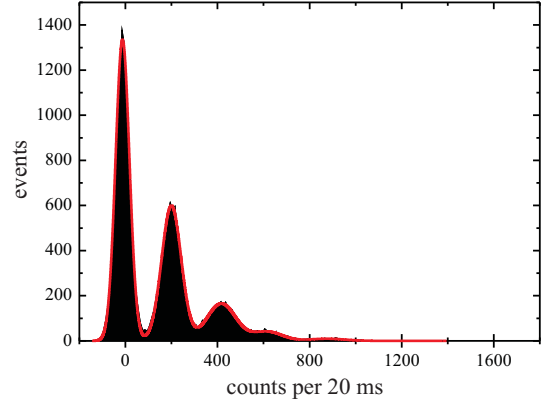
Here, R_0 denotes the loading rate of Cs without Rb and α is the proportionality factor. The parameters can be determined from a fit to be $R_0 = (1.48 \pm 0.06) \text{ s}^{-1}$ and $\alpha = (2.3 \pm 0.3) \cdot 10^{-4} \text{ s}^{-1}$.

In contrast, the loss rate, plotted in figure 4.10, does not show a monotonic behaviour, but it can be divided into three sections: Within the first section (I) covering the range of zero to 1000 Rb atoms, the loss rate increases with a rising number of Rb atoms. A constant loss rate of 1.9 atoms/s follows for higher Rb atom numbers up to 2300 Rb atoms (section II). For even larger Rb atom numbers the loss rate decreases (section III).

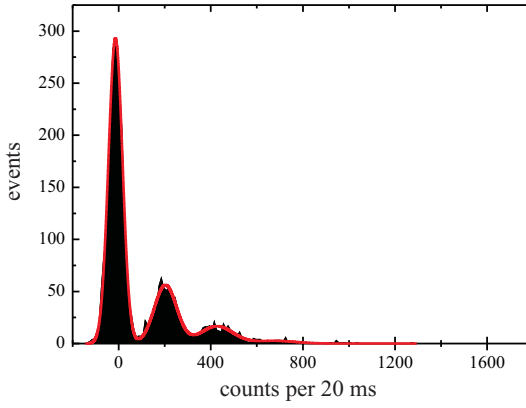
The evolution of the loss rate depending on the number of Rb atoms can be explained by regarding the ratio of the loading to the loss rate presented in figure 4.11. Here, within section I the loading rate dominates the dynamics of the single Cs atom MOT. However, although the loading rate decreases, leading to less captured Cs atoms, the loss rate is seen to increase. Hence, the enhancement of losses has to be a two species effect and can probably be attributed to cold collisions between Cs and Rb discussed in section 4.3. In this range of Rb atom numbers, where the loading rate exceeds the loss rate, the mean Cs atom number depends on the loading and detection time, which can also be seen in the fluorescence traces of figure 4.8(a). The Cs atom number increases continuously with time until the MOT is switched off.



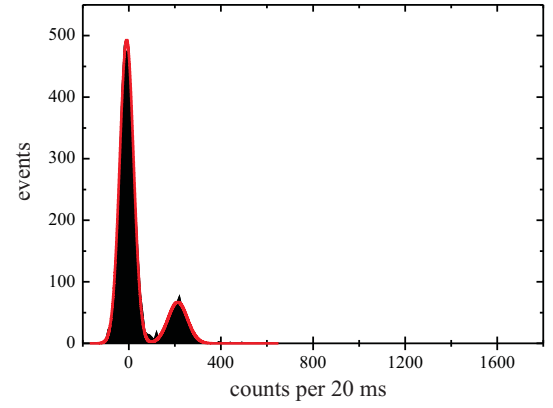
(a) Histogram of the single Cs atoms fluorescence signal in the presence of about 110 Rb atoms.



(b) Histogram of the single Cs atoms fluorescence signal in the presence of about 1200 Rb atoms.



(c) Histogram of the single Cs atoms fluorescence signal in the presence of about 2300 Rb atoms.



(d) Histogram of the single Cs atoms fluorescence signal in the presence of about 3000 Rb atoms.

Figure 4.12: Histogram of the single Cs atoms fluorescence signal for four different Rb atom numbers: The detected pulses are binned in time intervals of 20 ms each. The red lines are Gaussian fits to the peaks.

For higher Rb atom numbers, entering section II and III, the ratio between loading and loss rate tends to unity as shown in figure 4.11. Therefore, the evolution of the loss rate is determined by the loading rate. Within these two sections each loaded atom leaves the MOT again during the detection time. Thus, the loading and loss rates are identical in this region. In this regime the Cs system is in steady state. Steady state implies that the average Cs atom number does not change with an increasing loading and detection time.

Thus, for a Rb atom number larger than 1000, the time derivative of N_{Cs} can be set to zero and the steady state number of Cs atoms is given by a simplified version of

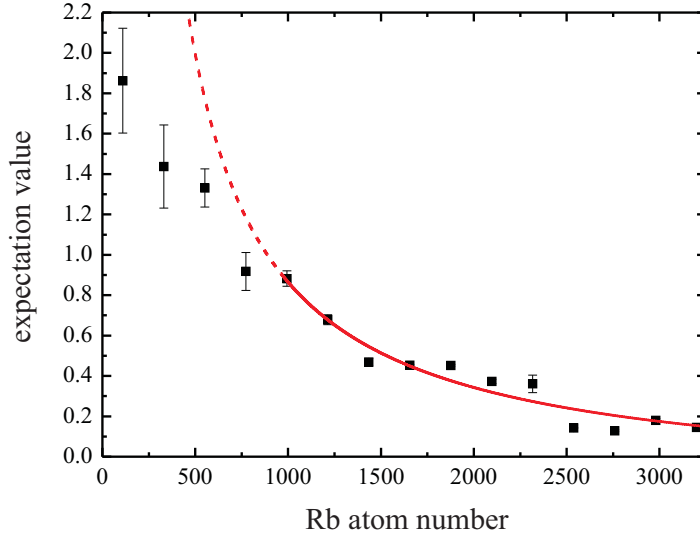


Figure 4.13: Expectation value of the Cs Poissonian distribution as a function of the Rb atom number. The red solid line is a fit of equation 4.13 to the data within the steady state regime. The red dashed line is the extrapolation to the non-steady state regime of the Cs MOT.

equation (4.11) as

$$N_{\text{Cs}} = \frac{R_0 - \alpha N_{\text{Rb}}}{\gamma + \beta_{\text{RbCs}} \frac{N_{\text{Rb}}}{(17\pi)^{3/2} w^3}}. \quad (4.13)$$

The steady state Cs atom number corresponds to the expectation value of Poissonian distributed Cs atom numbers measured for one set of experimental parameters. From the change of the mean Cs number as a function of the number of trapped Rb atoms, the inter-species collision rate constant β_{RbCs} can be deduced.

Four histograms of Cs are shown in figure 4.12 for a different amount of Rb present. The Cs atom number decreases obviously for an increasing N_{Rb} . In figure 4.12(a) for about $N_{\text{Rb}} = 110$ seven peaks corresponding to up to six atoms can be observed, whereas in figure 4.12(d) at most one atom is detected. The expectation values of these Poissonian distributions as a function of the Rb atom number are plotted in figure (4.13). A strong decay of the expectation value with increasing N_{Rb} is observed. The red solid line shows the fit of equation (4.13) to the data, where only γ and β_{RbCs} are free parameters and the others are fixed from the results of equation (4.12). Following [104] and averaging about all Zeeman states, the mean radius of the Cs cloud is calculated to be $w = 6.6 \mu\text{m}$ considering the magnetic field gradient and the laser beam parameters, such as intensity, waist, and detuning. Within the steady state regime the fit well reproduces the data. Extrapolating the fit to the region below 1000 Rb atoms, where the Cs system is not in steady state, the data and the fit deviate. Here, the equilibrium Cs atom number given by the extrapolation exceeds the measured expectation value, as the measured Cs

atom number is limited by the detection time. The inelastic inter-species collision rate constant is determined to be $\beta_{\text{RbCs}} = (1.7 \pm 0.6) \cdot 10^{-10} \text{ cm}^3/\text{s}$. It includes all mechanisms of inelastic cold collisions summarized as ground state and light-induced collisions. Our measured value is in good agreement with measurements of the Rb-Cs collision rate constant done in a balanced Rb-Cs MOT by [139]. The main uncertainty of the collision rate constant is given by the determination of the absolute value of the Rb atom number, which is only precise to a factor of 2. Thus, the systematic error of β_{RbCs} is obtained to be $\begin{pmatrix} +1.7 \\ -0.85 \end{pmatrix} \cdot 10^{-10} \text{ cm}^3/\text{s}$.

This measurement represents a significant step towards controlled doping of a BEC and already illustrates the use of single neutral atoms as a non-destructive probe to investigate many-body systems, where the overall state of the Rb cloud remains unmodified. The dynamics of the single atoms has enabled us to extract the inelastic inter-species collision rate constant. As both species are stored in presence of near resonant light, these cold collisions are dominated by light-induced interactions. In further experiments we aim on constraining the interaction to ground state collisions by storing both species in far-off resonant dipole traps. The ground state collisions are of interest in, e.g., applications for quantum information processing.

5 KRb molecules

5.1 Ultracold heteronuclear molecules

Associations of ultracold molecules in the vicinity of a Feshbach resonance are of broad interest as these weakly bound molecules can be used as a first step to produce molecules in the rovibrational ground state. In particular, heteronuclear molecules in the rovibrational ground state offer new research perspectives due to their relatively large permanent dipole moment. These polar molecules are characterized by strong long-range dipole-dipole interactions. Hence, they provide a basis for many further experiments, e.g. the investigation of new quantum phases [49] or the production of dipolar BECs [47]. The permanent dipole moment of the bosonic $^{41}\text{K}^{87}\text{Rb}$ molecule is predicted to be about 0.8 Debye [140]. In addition, spectroscopy measurements of these Feshbach molecules yield new information to improve the molecular potential, which is of particular importance in order to transfer these molecules to the rovibrational ground state. A remarkable property of these near-threshold molecules is their universal behaviour, which has been discussed in section 2.3.3.

So far a number of different homonuclear shallow dimers have been produced as ^{133}Cs [60, 61], Na [62], ^{87}Rb [63] and also fermionic heteronuclear $^{40}\text{K}^{87}\text{Rb}$ molecules [64, 65, 58]. The only bosonic heteronuclear molecules have been generated by the two isotopes ^{85}Rb and ^{87}Rb [66]. Due to their small difference in mass the dipolar moment of these molecules is negligibly small.

Different kinds of association techniques have already been developed in the field of ultracold gases. The most common technique is to produce the molecules by ramping the homogeneous magnetic field across a Feshbach resonance from the negative to the positive scattering length side [54]. The strong coupling between the atomic and molecular state leads, in the dressed atom picture, to an avoided level crossing. Sweeping the magnetic field adiabatically across the resonance allows the efficient conversion of atoms to weakly bound molecules. Remaining atoms are removed by a resonant laser pulse. Afterwards the pure molecular ensemble is dissociated to atoms by rapidly sweeping the magnetic field across the resonance to the negative scattering length side. The number of atoms after this experimental procedure gives information on the number of associated molecules. The disadvantage of this method is a heating of the ensemble which occurs due to three-body recombination losses close to the resonance. This can be avoided using alternative methods which either couple the entrance and molecular state by applying a radio frequency [57, 58] or modulate the homogeneous magnetic field [59]. As the latter association method is used in our experiment, this method will be introduced in more

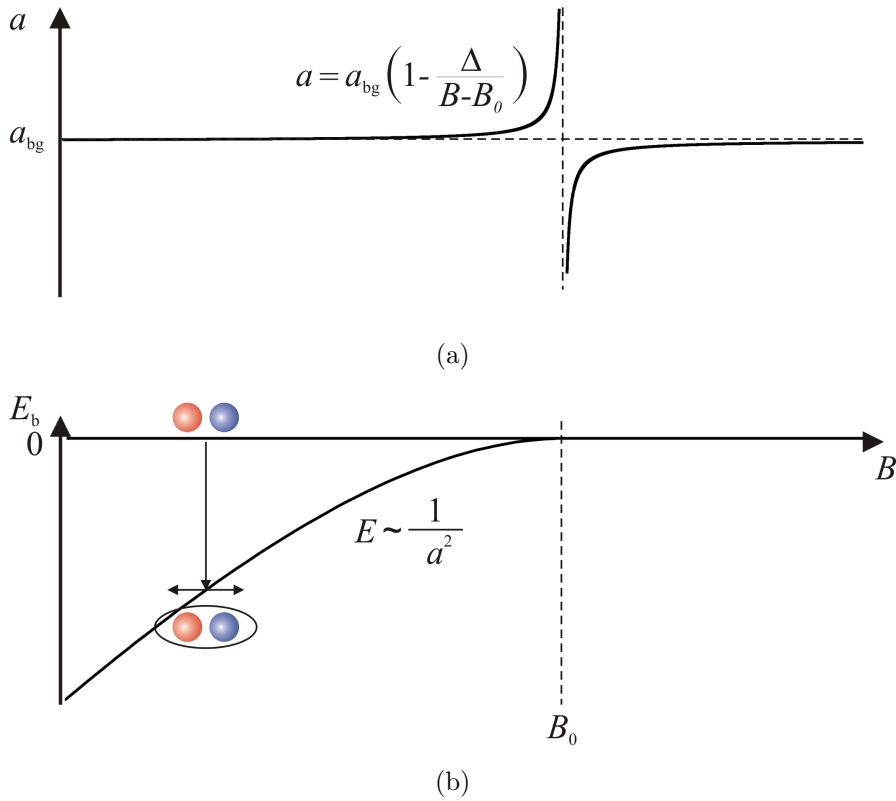


Figure 5.1: (a) Scattering length in the vicinity of a Feshbach resonance. (b) Binding energy of Feshbach molecules. The dashed vertical line indicates the Feshbach resonance position. The dashed horizontal line marks the background scattering length. The dissociation threshold of the two colliding atoms is indicated by the solid horizontal line.

detail.

In the universal regime, for positive scattering lengths the binding energy of the weakly bound molecules depends quadratically on the magnetic field (figure 5.1). An additional sinusoidal magnetic field modulates the Feshbach field and hence the binding energy with the corresponding modulation frequency. Feshbach molecules can be created when the modulation frequency is resonant to the binding energy of the molecules at the chosen background magnetic field. This assumption is only valid for zero temperature atomic clouds. For a finite temperature the atoms populate different continuum states. The population of the continuum states follows the Boltzmann distribution. The resonance frequency for an atomic ensemble of temperature T at a magnetic field B is modified to be

$$\omega = \frac{E_b(B)}{\hbar} + \frac{k_B T}{\hbar}. \quad (5.1)$$

The technique of molecule association by modulation of a dc-magnetic field allows not

only for the production of molecules, but at the same time provides a spectroscopy measurement of the binding energy which gives important information on the form of the molecular potential. Furthermore, short association times without crossing the resonance reduce the heating effect due to minimizing three-body recombination losses. Equation (5.1) directly shows different properties. Inside the universal regime the resonance modulation frequency is proportional to the square magnetic field due to the quadratic dependence of the binding energy on the magnetic field. For a fixed magnetic field the resonance frequency is shifted to larger values for increasing temperature. More precisely, a finite temperature results in a kinetic energy distribution which is described by the Boltzmann distribution and discussed in the next section. The higher the temperature the broader the energy distribution. The resonant behaviour of the modulation frequency is washed out and the association efficiency decreases for a fixed frequency with increasing temperature. Hence, ultracold ensembles with temperatures as low as possible are required to efficiently produce molecules.

5.2 Association of ultracold bosonic KRb molecules

As described above, the association of weakly bound molecules requires low temperatures and an accessible and sufficiently broad Feshbach resonance. In the following section the preparation of an ultracold ^{41}K - ^{87}Rb mixture is introduced. This experimental setup is similar to the Rb-Cs experiment described in more detail in chapter 3. Hence, only a short overview of the experimental sequence and some specific characteristics are given. The detailed description of the bosonic K-Rb experiment in Florence can be found in the thesis of Jacopo Catani [141].

5.2.1 Experimental preparation of an ultracold K-Rb mixture

Both bosonic species Rb and K are initially trapped in two separated two-dimensional magneto-optical (2D-MOT) traps [142] and transferred, by radiation pressure, to a common three-dimensional MOT (3D-MOT) in the main chamber of the ultra high vacuum system. The 2D-MOTs present atom sources of high flux of the order of 10^{11} atoms/s and thereby facilitate short loading times of the two-species 3D-MOT of about 10 s. The laser setup of Rb is similar to the one in chapter 3 consisting of a tapered amplifier (Toptica: TA-100) and a diode laser in Littrow configuration to provide the cooling and repumping light. In the case of ^{41}K the cooling scheme is more complicated as a differentiation between a cooling and repumping transition is not possible due to the marginal hyperfine splitting of the excited electronic state¹, which is at most 13 MHz [143]. Hence, cooling and repumping light are of the same significance. However, during this thesis the same notation for the transitions is used as for Rb. The laser light is provided by a high power laser diode with an external cavity (DLX110 from Toptica) delivering an output

¹The hyperfine structure of K is depicted in Appendix A.

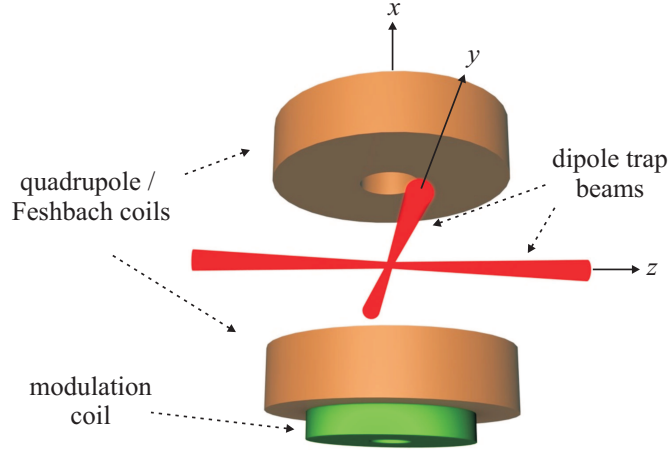


Figure 5.2: Simplified schematic of the experimental setup: Atoms are trapped in the centre of the crossed dipole trap beams (red). Two coils in Helmholtz configuration (brown cylinders) provide the homogeneous offset field. An additional coil (green cylinder) produces the magnetic field modulation.

power of 800 mW. An array of AOMs generate the required frequencies. The cooling laser frequency is detuned by $-1 \Gamma_K$, whereas the repumping light is detuned by $-4 \Gamma_K$ with respect to the corresponding transition². For both wavelengths (780 nm and 767 nm) the same optics and polarization maintaining fibres are used. Special dichroic retardation plates allow to independently adjust the polarization. As in the Rb-Cs-system, both species are optically pumped into the doubly polarized states $|f = 2, m_f = 2\rangle$ after a compression and molasses stage. The spin-polarized mixture is transferred into a purely magnetic trap. A unique feature of this experimental setup is the millimetric Ioffe trap, which is a kind of Ioffe-Pritchard trap on the scale of $1 \times 2 \text{ cm}^2$ implemented directly in the vacuum [144]. Large trap frequencies as obtained by the millimetric trap, which are $\omega_\rho = 2\pi \cdot 204 \text{ Hz}$ and $\omega_{ax} = 2\pi \cdot 16.5 \text{ Hz}$ for ^{87}Rb in the doubly polarized state, ensure strong confinement and evaporation times as low as 15 s. According to their mass ratio the trap frequencies of ^{41}K are given by $\omega_K = \sqrt{87/41} \omega_{\text{Rb}} \approx 1.4 \omega_{\text{Rb}}$. The trap centres of the quadrupole and the millimetric trap are separated by 27 mm. The two quadrupole coils of the MOT system mounted on a translation stage move the atomic clouds towards the millimetric trap. Further reduction of the temperature and increase of the phase space density are achieved by species selective forced evaporative microwave cooling acting on Rb. Due to the difference in the hyperfine splitting of more than 6 GHz no atomic transitions of K are driven. However, K is simultaneously cooled sympathetically via elastic collisions with the cold bath of Rb. Due to a large inter-species *s*-wave scattering length of $164 a_0$ the K temperature decreases efficiently. The evaporation process is manually stopped at about $1.5 \mu\text{K}$ and the atomic mixture is transferred to a crossed

²The natural linewidth and the wavelength of the D2-transition of K are $\Gamma_K = 2\pi \cdot 6.2 \text{ MHz}$ and $\lambda_K = 766.5 \text{ nm}$, respectively.

far-detuned optical dipole trap, as in this kind of trap all magnetic substates can be trapped. In addition, it provides the possibility of using an external magnetic field as a free parameter. A Yb-fiber laser with a wavelength of 1064 nm and an output power of 20 W provides a far detuned dipole trap with respect to the D1 and D2 lines of Rb and K. Using a PBS the output beam is split up for both dipole trap branches. After passing AOMs, both laser beams, with an initial power of 3 W each, are focused to the centre of the millimetric trap to a waist of 90 μm resulting in a total effective initial trap depth of 30 μK with a trap frequency of $2\pi \cdot 270$ Hz along the gravitational axis. The power of the dipole trap beams is ramped up by increasing the RF power of the AOMs within 250 ms. After a short overlapping time, in which both, optical and magnetic, traps are present, the magnetic field is switched off.

Subsequently an adiabatic passage transfers both species to the magnetically anti-trapped absolute ground state $|f = 1, m_f = 1\rangle$ to enable the access of Feshbach resonances, absent in the $|2, 2\rangle$ state and to additionally reduce inelastic collisions. Spin-exchange collisions are suppressed, as for atomic ensembles at a temperature of 1.5 μK the kinetic energy of the order of several kHz is not sufficient to change the hyperfine state: the hyperfine splitting of Rb (K) being $h \cdot 6.8$ GHz ($h \cdot 254$ MHz). At a magnetic field of about 7 G the Rb sample is transferred adiabatically to the ground state $|1, 1\rangle$ by microwave radiation. Remaining Rb atoms in the doubly polarized state are removed by a resonant light pulse to avoid atom loss due to K-Rb collisions. Afterwards K is transferred by radio frequency radiation to the $|1, 1\rangle$ state. For K atoms no cleaning light pulse is required.

Further evaporative cooling by lowering the trap depth of the crossed dipole trap reduces the temperature to about 200 nK. Although the purely optical trap depth for K is smaller than for Rb, if gravity is included, the combined potential for K is deeper than for Rb due to their different masses. Therefore, efficient cooling of K is achieved by thermal contact with Rb. The evaporation process was optimized by tuning the inter-species scattering length to about 200 a_0 applying a homogeneous magnetic field of about 78 G, next to a K-Rb *s*-wave Feshbach resonance [30]. This increases the elastic collision and thus the thermalization rate. The magnetic field is produced using the former quadrupole coils in Helmholtz configuration.

With this configuration at a temperature of 200 nK about $4 \cdot 10^4$ Rb atoms and $3 \cdot 10^4$ K atoms are stored. Further cooling is not successful as, due to the species-dependent gravitational sag, the spatial overlap of the mixture components vanishes and K is not in thermal contact with the Rb cloud anymore. Atom number and temperature are determined after a time-of-flight between 5 and 15 ms by absorption imaging.

5.2.2 Association and detection of KRb molecules

To produce ultracold shallow KRb-dimers two *s*-wave Feshbach resonances are accessible below 100 G. A broad resonance can be observed at about 37 G with a width of 34 G and a more narrow one at 79 G with a width of 1.2 G. The weakly bound molecules are

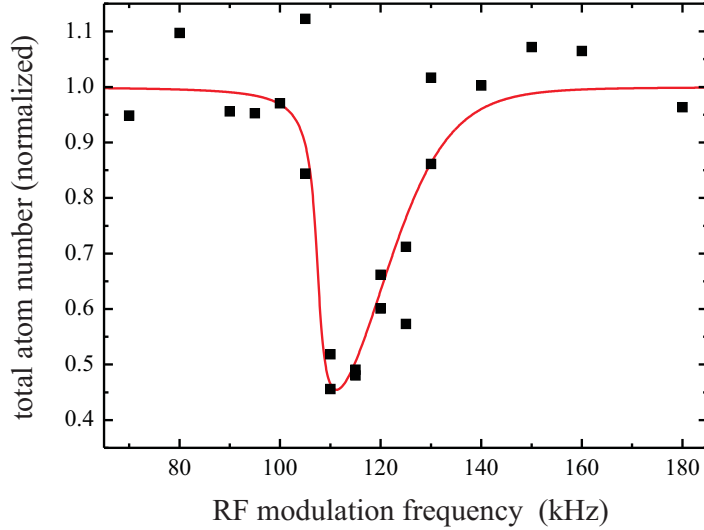


Figure 5.3: A typical molecule association spectrum at a magnetic offset field $B_{\text{dc}}=78.25$ G is shown. A RF modulation pulse of 30 ms was applied. The data are fitted (red solid line) by the analysis described in section 5.2.

associated by sinusoidally modulating an external homogeneous field. After preparation of an ultracold mixture in the crossed optical dipole trap the homogeneous magnetic field is set to a value next to one of the Feshbach resonances at the positive scattering length side, where weakly bound molecular states exist. Parallel to the Helmholtz coils a third coil of only eight windings is assembled as shown in figure 5.2. A sinusoidal signal in the frequency range of 50 to 200 kHz produced by a frequency generator is amplified using a 200 W audio operation amplifier. This leads to a typical modulation amplitude of 130 mG. The pulse has a square envelope and its duration to measure the lineshapes shown in the following figures varies in the range of 10 to 30 ms for the narrow resonance and up to 1 s for the broad resonance. Throughout this thesis the modulation is referred to as RF modulation. After this RF pulse and subsequently ramping down the magnetic field, the remaining atoms are released from the dipole trap. After a time-of-flight of 5 ms and 10 ms for K and Rb, respectively, the remaining atom number is determined separately by absorption imaging. The association of the heteronuclear molecules is indirectly proved by observing significant atom losses of both species. As the molecules are associated inside the two thermal clouds of Rb and K, the dimers may decay into deeper molecular bound states by collisions with unpaired Rb or K atoms. The difference in binding energy of the shallow and deeply bound molecular states, which is typically in the range of 100 MHz to 10 GHz is released and converted to kinetic energy of the colliding particles. According to the mass ratio of the atom and molecule, the KRb molecule gains 1/4 or 2/5 of the released energy depending on the species of the scattered single atom. In general, the trap depth of the crossed dipole trap, which is about $k_{\text{B}} \cdot 10 \mu\text{K}$, is not sufficient to hold the deeply bound molecule and the scattered atom. Both of them are lost from the trap. Additionally

dimer-dimer collisions can take place, but due to the low molecular density atom-dimer collisions are more probable. Hence, atom loss is a signature of molecule production. The intrinsic lifetime of Feshbach molecules and the apparent atom loss are discussed in more detail in the next section. The remaining number of atoms determined after the modulation pulse at a fixed dc-homogeneous magnetic field depends on the modulation frequency and yields information on the molecule association efficiency, the lifetime and the binding energy. Figure 5.3 shows a typical loss feature measured for a dc-magnetic field of 78.25 G and a RF modulation time of 30 ms. A broad, asymmetric loss signal can be observed. The strong asymmetry is attributed to the kinetic energy distribution of the two thermal atomic clouds. The binding energy is measured for different magnetic fields for both *s*-wave Feshbach resonances. The magnetic field calibration is done by microwave spectroscopy with a resolution limited to about 20 mG. In the next section the analysis of the measured loss features will be described in detail.

5.3 Experimental results and analysis

5.3.1 Association spectrum

For a precise determination of the binding energy the asymmetric lineshape of the measured loss features has to be analyzed. Quantum mechanically, the association of molecules can be described by a time-dependent Hamiltonian

$$H(t) = H_0 + H_I(t), \quad (5.2)$$

consisting of the unperturbed part H_0 and the interaction part $H_I(t)$. The first term describes the kinetic energy of the atoms and molecules with mass m_i separately. The interaction part $H_I(t)$ considers the coupling between the scattering and the molecular state by RF modulation. It is time-dependent as a time-dependent sinusoidal modulation is applied. Assuming two non-interacting atomic species K and Rb and the corresponding heteronuclear molecules KRb, the undisturbed Hamiltonian of this system reads

$$H_0 = \frac{\hbar^2 k^2}{2m_K} \hat{a}_K^\dagger \hat{a}_K + \frac{\hbar^2 k^2}{2m_{\text{Rb}}} \hat{a}_{\text{Rb}}^\dagger \hat{a}_{\text{Rb}} - \left(E_b(t) - i \frac{\gamma}{2} \right) \hat{a}_{\text{KRb}}^\dagger \hat{a}_{\text{KRb}}, \quad (5.3)$$

where $\hat{a}_K^\dagger, \hat{a}_K, \hat{a}_{\text{Rb}}^\dagger, \hat{a}_{\text{Rb}}, \hat{a}_{\text{KRb}}^\dagger$ and \hat{a}_{KRb} are the creation and annihilation operators for a K or Rb atom and a KRb molecule, respectively. Setting the energy level of the scattering channel to zero, only the kinetic energy of the incoming colliding atoms contribute to the Hamiltonian, which corresponds to the centre-of-mass frame of the two colliding atoms with momentum $\hbar \vec{k}$ and $-\hbar \vec{k}$. The last term of equation (5.3) accounts for the finite lifetime of the molecules by inserting the decay constant γ . The coupling between the entrance and closed channel is induced by a sinusoidal modulation with frequency ω of the applied dc external magnetic field

$$B(t) = B_{\text{dc}} + b \sin(\omega t). \quad (5.4)$$

Taking this into account the time-dependent interaction Hamiltonian $H_I(t)$ becomes

$$H_I(t) = \Omega(B(t)) \left(\hat{a}_K \hat{a}_{Rb} \hat{a}_{KRb}^\dagger + \hat{a}_K^\dagger \hat{a}_{Rb}^\dagger \hat{a}_{KRb} \right) \quad (5.5)$$

using the definition of [145] for the coupling strength $\Omega(B(t))$. Considering equation (5.4) together with the time-dependent Schrödinger equation, coupled amplitude equations are obtained in [145]. These yield the coupling strength given by the derivative of the projected eigenstates with respect to the magnetic field

$$\Omega(B(t)) = b\omega \frac{\partial}{\partial B'} \langle \Psi_{K-Rb}(B) | \Psi_{KRb}(B) \rangle \cos(\omega t), \quad (5.6)$$

where the time-independent part of equation (5.6) $\Omega_0(B) = b\omega \frac{\partial}{\partial B'} \langle \Psi_{K-Rb}(B) | \Psi_{KRb}(B) \rangle$ is called Rabi frequency. If the amplitude b of the magnetic field modulation is small compared to the width of the Feshbach resonance, the time dependence of the coupling strength is negligible. Furthermore, the time-dependent modulation of the binding energy E_b of the shallow molecule in equation (5.3), induced by the oscillating magnetic field, can be neglected. Equation (5.2) can be rewritten in the Heisenberg form

$$\frac{d\hat{a}_i}{dt} = \frac{i}{\hbar} [H, \hat{a}_i], \quad (5.7)$$

which gives differential equations for the annihilation operators \hat{a}_i . As the operators for different species commute and $[\hat{a}_K^\dagger, \hat{a}_K] = [\hat{a}_{Rb}^\dagger, \hat{a}_{Rb}] = [\hat{a}_{KRb}^\dagger, \hat{a}_{KRb}] = 1$, three coupled differential equations can be obtained. Substituting the operators by complex-numbers ($\hat{a}_i \rightarrow \alpha_i$) the following non-linear Bloch equations are found

$$i \frac{d\alpha_{KRb}}{dt} = \left(-\frac{E_b}{\hbar} - i\frac{\gamma}{2} \right) \alpha_{KRb} + \Omega_0 \cos(\omega t) \alpha_K \alpha_{Rb}, \quad (5.8)$$

$$i \frac{d\alpha_K}{dt} = \frac{p^2}{2\hbar m_K} \alpha_K + \Omega_0 \cos(\omega t) \alpha_{KRb} \alpha_{Rb}^*, \quad (5.9)$$

$$i \frac{d\alpha_{Rb}}{dt} = \frac{p^2}{2\hbar m_{Rb}} \alpha_{Rb} + \Omega_0 \cos(\omega t) \alpha_{KRb} \alpha_K^*. \quad (5.10)$$

The experimental observable is the remaining atom number of the two species after a chosen interaction time. Theoretically, the total remaining atom number at time t is given by $N_{\text{tot}}(t) = N_K(t) + N_{Rb}(t) = \alpha_K(t) \alpha_K^*(t) + \alpha_{Rb}(t) \alpha_{Rb}^*(t)$. For solving equation (5.8) the slowly varying amplitude functions $\alpha_K = \tilde{\alpha}_K \exp(-i\hbar k^2/(2m_K)t)$, $\alpha_{Rb} = \tilde{\alpha}_{Rb} \exp(-i\hbar k^2/(2m_{Rb})t)$ and $\alpha_{KRb} = \tilde{\alpha}_{KRb} \exp(i(\omega - E_{\text{kin}}/\hbar)t)$ are introduced, with $E_{\text{kin}} = p^2/(2m_{Rb}) + p^2/(2m_K)$. The time derivative of the atom number N_i can then be written as

$$\dot{N}_i(t) = \alpha_i \dot{\alpha}_i^* + \alpha_i^* \dot{\alpha}_i = \tilde{\alpha}_i \dot{\tilde{\alpha}}_i^* + \tilde{\alpha}_i^* \dot{\tilde{\alpha}}_i. \quad (5.11)$$

Assuming a fast molecular decay the amplitude $\tilde{\alpha}_{KRb}$ follows adiabatically the evolution dictated by the slower RF coupling. In the limit of $d\tilde{\alpha}_{KRb}/dt = 0$ and applying the

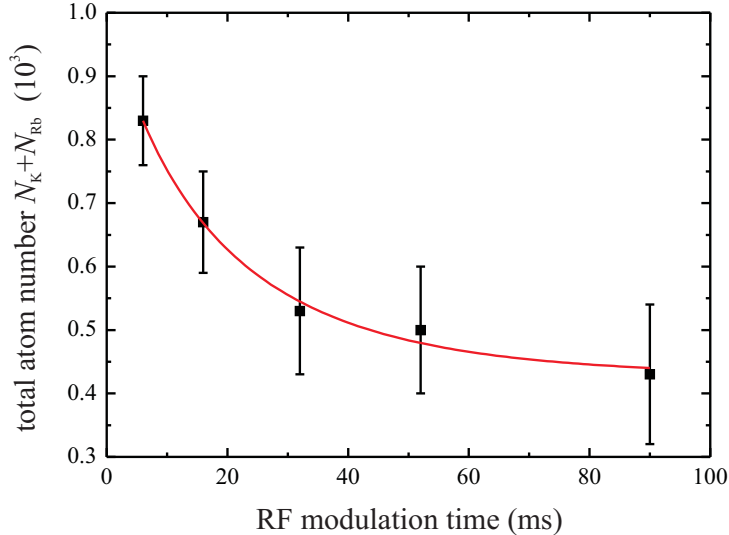


Figure 5.4: Total remaining number of atoms as a function of the RF modulation time. The solid line is a fit of equation (5.13) to the data, confirming the non-exponential decay.

rotating wave approximation which neglects all fast oscillating terms, the time derivative of the total atom number can be written in the simple form

$$\dot{N}_{\text{tot}}(t) = -\Gamma N_{\text{tot}}^2(t), \quad (5.12)$$

where an equal number of atoms for both species, K and Rb, is assumed. Equation (5.12) is equivalent to the well-known rate equation describing two-body loss. Solving equation (5.12) gives the time evolution of the total number of atoms

$$N_{\text{tot}}(t) = \frac{N_0}{N_0 \Gamma t + 1}, \quad (5.13)$$

where N_0 is the total initial atom number and the loss coefficient Γ is defined as

$$\Gamma = \frac{\frac{\gamma}{2} \Omega_0^2}{4 \left(\omega - \frac{E_b}{\hbar} - \frac{E_{\text{kin}}}{\hbar} \right)^2 + \gamma^2}. \quad (5.14)$$

The non-exponential decay of the total atom number is experimentally confirmed. Figure 5.4 shows the remaining total atom number as a function of the RF time described by equation (5.13).

So far only a fixed value for the relative kinetic energy of the participating particles was assumed. In real systems the kinetic energy of an atomic ensemble with a non-zero temperature T is Boltzman-distributed. Therefore, different continuum states of the scattering channel are populated. In theory, this kinetic energy distribution is taken into account by convolving the loss rate by the energy distribution $((\Gamma * g)(E))$. The

energy distribution can be obtained by rewriting the well-known Boltzmann velocity distribution for a temperature T as

$$g(E) dE = \frac{2\sqrt{E}}{\sqrt{\pi}(k_B T)^{3/2}} e^{-\frac{E}{k_B T}} dE. \quad (5.15)$$

Hence, for a finite temperature the resonance condition is not sharp anymore and the resonance behaviour is washed out. Including this fact in the calculations by convolving the effective decay rate with the kinetic energy Boltzmann distribution, the observed asymmetric line shape is well described. The larger the temperature the broader the distribution. This fact strengthens the importance of working with ultracold atomic clouds for efficient molecule association. The lifetime γ , the coupling strength Ω and the binding energy are chosen as free parameters to fit the remaining atom number to the observed loss feature. To optimize these parameters, the function

$$\chi^2 = \sum_i \frac{(N_{\text{meas},i}(t) - N_{\text{theo},i}(t))^2}{N_{\text{theo},i}(t)} \quad (5.16)$$

is minimized (solid lines in figure 5.5). To emphasize the effect of the decay constant γ , figure 5.5 shows, in addition, a fit (red dashed line) to the measured data where the molecules are assumed to be stable. The smooth low frequency part of the loss feature is well described by including the finite lifetime. The sharp step-like behaviour of the energy distribution can, in addition, be washed out by technical instabilities such as fluctuations of the magnetic field.

5.3.2 Spatial overlap

It is favourable to further reduce the temperature in order to more efficiently produce molecules. However, storing two species with different masses in an optical dipole trap implies different gravitational sags. This leads to a partial overlap of the clouds. As the gravitational sag is proportional to g/ω_x^2 , the overlap fraction depends on the trapping frequencies along the gravitational axis and the temperature of the cloud, which determines, together with ω_x , the size of the cloud. Figure 5.6 shows the overlapping fraction depending on the temperature of the Rb and K cloud for five different effective trap depths U_{eff} of the dipole trap. The overlapping fraction can be determined by

$$n_{\text{KRb}} = \frac{\int_V n_{\text{K}}(r) n_{\text{Rb}}(r) dr}{\int_V n_{\text{Rb}}^2 dr}, \quad (5.17)$$

assuming a similar density for Rb and K. The density distribution $n_j(r)$ of the atomic clouds in a harmonic potential with trap frequencies ω_i is given by

$$n_j(r) = \frac{N_j m}{\pi^{3/2} d_x d_y d_z} e^{-\left(\frac{y^2}{d_y^2} + \frac{z^2}{d_z^2} + \frac{(x-g/\omega_x^2)^2}{d_x^2}\right)}, \quad (5.18)$$

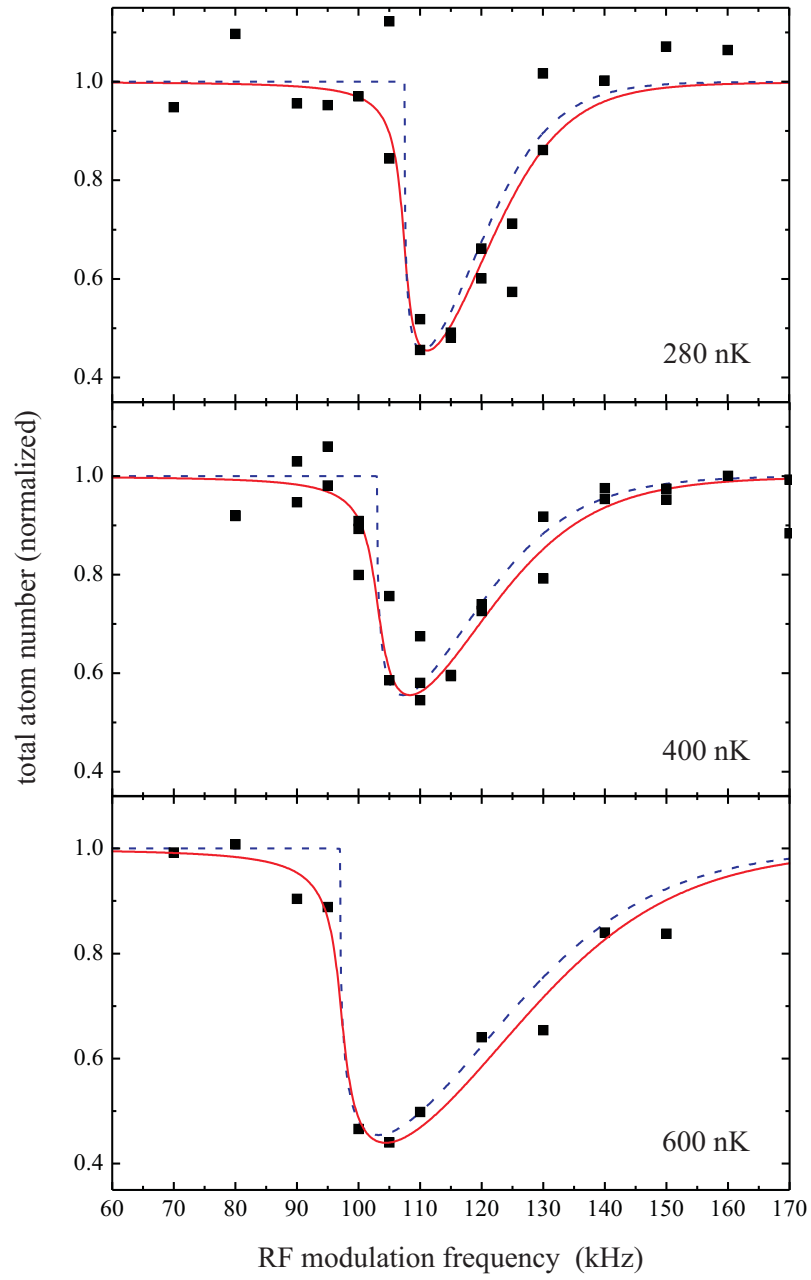


Figure 5.5: Measured atom loss signals for three different atomic cloud temperatures in the range of 280 to 600 nK. The remaining atom numbers are measured after a fixed modulation time of 30 ms around a dc magnetic field of 78.2 G. The asymmetric lineshapes are well reproduced by the analysis (red solid line). The blue dashed lines indicate a fit with $\gamma = 0$.

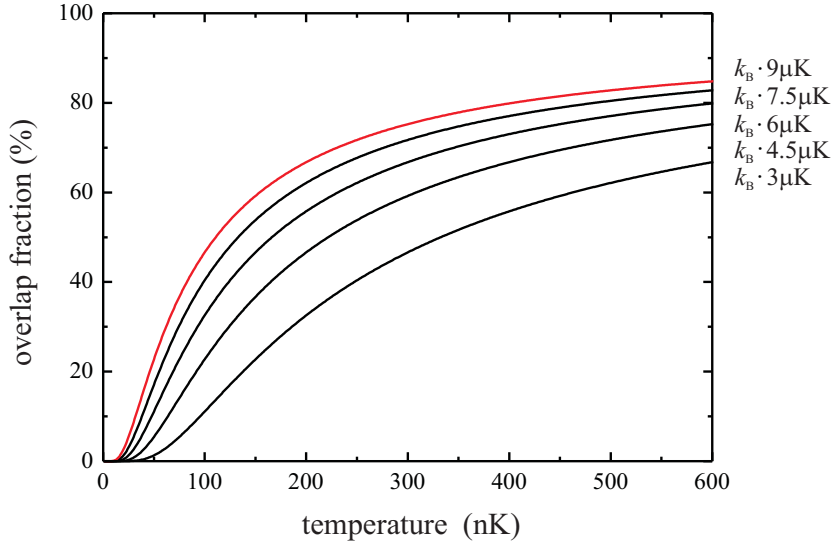


Figure 5.6: The overlapping fraction of two thermal clouds as a function of the cloud temperature is plotted for five different trap depths, which corresponds to different trapping frequencies. The experimental data have been taken for a trap depth of about $k_B \cdot 9 \mu\text{K}$ corresponding to an overlap fraction indicated by the red solid line.

where the characteristic length d_i is defined by

$$d_i = \sqrt{\frac{2 k_B T}{m_{\text{Rb}} \omega_i^2}}. \quad (5.19)$$

The molecular association data have been taken for an effective trap depth of about $9 \mu\text{K}$, which corresponds to the red line in figure 5.6. The minimum temperature in our dataset is about 150 nK corresponding to an overlapping fraction of 60% . The higher the temperature the larger the overlap fraction. During the experiment the temperature of the ensemble is adjusted by stopping the evaporation in the dipole trap. Hence, larger cloud temperatures correspond also to deeper trapping potentials and larger trap frequencies, resulting in a better overlap. The densest part of the cloud is in the centre where also the coldest atoms are located. Hence, spatial separation of the atomic clouds reduces effectively the efficiency of the molecule production. During the data analysis this is taken into account by adjusting the coupling strength Ω_0 .

The association efficiency can be optimized by increasing the spatial overlap, e.g., by increasing the trap frequencies. Another perspective is to add a dipole trap using an appropriate wavelength which compensates the gravitational sag [146]. This occurs when the ratio of the potential depths is the same as the inverse ratio of their masses.

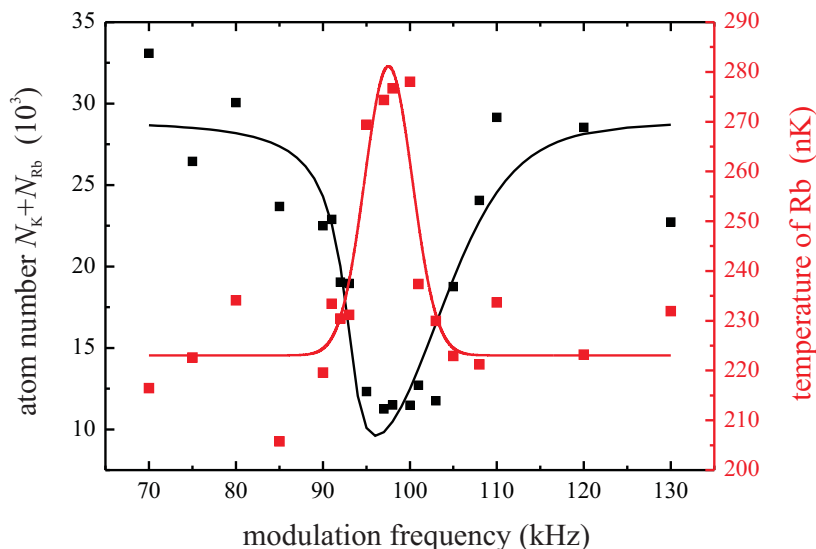


Figure 5.7: Remaining atom number and corresponding temperature of Rb for a molecular association spectrum. An increase of the Rb temperature on resonance of the association peak is observed. The Gaussian fit to the temperature data is only a guide to the eye.

5.3.3 Lifetime of the KRb dimers

The lifetime of weakly bound molecules depends strongly on the specific loss mechanisms dominating in a particular experimental system. Neglecting collisional decay of molecules, the typical intrinsic lifetime of the dimers ranges between several tens of microseconds up to tens of milliseconds. The limited lifetime is a result of the molecule's coupling to the entrance channel as well as to a spontaneous decay into energetically lower open channels. The latter decay process occurs due to inelastic spin relaxation and scales within the universal regime with a^{-3} [147]. This is a direct consequence of the large spatial extension of the wave function ($r_{\text{mean}}=a/2$) caused by universality. The increasing stability when approaching the Feshbach resonance was experimentally shown for ^{85}Rb [148]. For molecules associated from atomic ensembles in the lowest energy state as done in our case, an inelastic decay of the molecular state into an open channel other than the entrance channel is not possible, as the entrance channel is the only open channel in such systems. Therefore, the intrinsic lifetime of dimers created by ground state atoms is given by the decay in their entrance channel. As in our system molecules are not directly imaged, this kind of decay cannot be observed, as no atom losses are induced. Much longer lifetimes are observed in systems with high rotational molecular states ($l > 0$). For a non-zero orbital quantum number the centrifugal barrier arises, which is proportional to $l(l+1)$. This barrier suppresses the decay into the entrance channel in the same way, as for ultracold atoms only s -wave scattering occurs. Metastable molecules with lifetimes up to 1 s were recently observed for ^{133}Cs dimers in

a l -wave state ($l=8$) [149].

In our experiment, in which the dimers are produced inside an atomic cloud, the predominant decay process is caused by collisions with further dimers or unpaired atoms. The molecules associated in the vicinity of the two s -wave Feshbach resonances used, are in high vibrational states of the rotational ground state. The abovementioned collisions lead to relaxation into energetically lower vibrational states. This process is referred to as vibrational quenching [150, 151]. The time derivative of the dimer number n_d is then given by the rate equation

$$\dot{n}_d = -K_{ad} n_a n_d - K_{dd} n_d^2. \quad (5.20)$$

Here, K_{ad} and K_{dd} denote the loss rates of the atom-dimer and dimer-dimer collisions, respectively. The dimer density n_d during our experimental sequence is much lower than the atomic density n_a , which is about $5 \cdot 10^{11} \text{ cm}^{-3}$ for each species. Hence, the first term dominates the loss process. The molecules inside the cloud of unpaired atoms undergo dimer-atom collisions thereby decaying into deeply bound states as explained in section 5.2.2. The released difference in binding energy is converted to kinetic energy and the colliding particles leave the trap. In addition, secondary elastic and inelastic collisions with further trapped atoms may occur before the colliding particles leave the trap. Kinetic energy which is transferred to these additional scattered atoms will heat up the atomic clouds and therefore leads to additional trap loss. The atom-dimer loss rate scales with the scattering length a [152, 153], which leads to increasing inelastic atom-dimer collision rates when approaching the Feshbach resonance. A heating of the remaining atomic ensemble is experimentally observed as shown in figure 5.7. This heating can originate from inelastic collisions as described above. It proves that a significant decay of molecules takes already place during the RF pulse of 10 ms due to vibrational quenching.

Experimentally the decay was investigated by measuring the total number of atoms as a function of the storage time after the molecule association. A K-Rb mixture with a temperature of 500 nK was produced in the crossed dipole trap for both atomic species in the $|1, 1\rangle$ -state. At a fixed magnetic field of 78.02 G, the association peak is determined. Molecules are associated at a radio-frequency of 225 kHz using a RF pulse of 32 ms. After switching off the radio-frequency the storage time is varied. Figure 5.8 shows a fast decay of the atomic mixture with a time constant of $(220 \pm 40) \mu\text{s}$. This value is only a lower limit of the intrinsic lifetime of the shallow dimer, as this graph describes the molecular decay in presence of unpaired atoms, which by collisions can lead to an enhanced decay of the molecules. Therefore, the decay rate apparent in figure 5.8 strongly depends on the density of the unpaired atoms. Hence, most of the KRb dimers associated within the 32 ms RF pulse may decay due to the above discussed collisions and their coupling to the entrance channel already during the RF pulse. The remaining molecules at time 0 s of the storage time in figure 5.8 decay with the time constant of $(220 \pm 40) \mu\text{s}$. Atom loss due to the Feshbach resonance can be neglected on this timescale, as the decay measurement is taken at 78.02 G outside the loss feature of the Feshbach resonance, which is plotted in figure 2.5(b). This Feshbach loss measurement is taken after a storage time of 500 ms. The molecular decay rate can be reduced by lowering the atomic densities, which can be

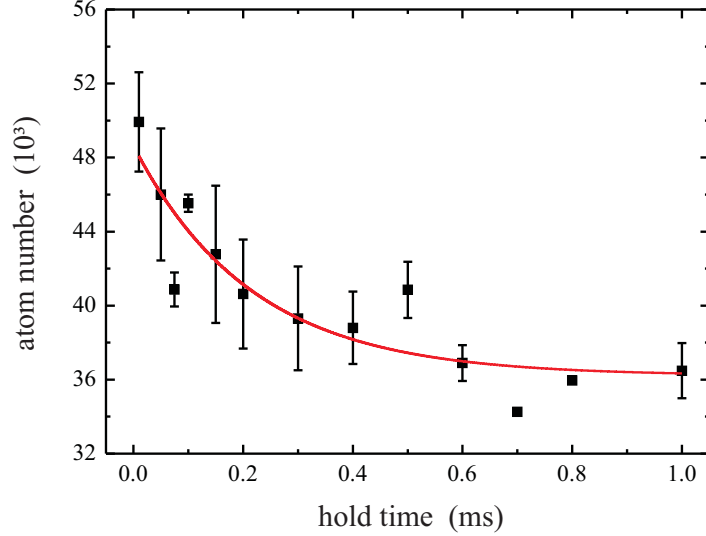


Figure 5.8: Decay of the total atom number after association of molecules. At a magnetic field of 78.02 G molecules are associated by a radio frequency pulse of 32 ms. The cloud temperature is about 500 nK. After switching off the RF-modulation the atom number is measured varying the storage time.

achieved by shallow traps or by association of molecules after switching off the trap. A further method exploits the Stern-Gerlach effect by applying a magnetic field gradient after the association [63, 60]. The molecular and atomic clouds are separated due to their different magnetic moments and the decay rate decreases. However, the last method needs an effective association as well as a sufficiently low decay time. In our case, with a decay time of about 200 μ s, it is not applicable. Almost complete suppression of inelastic collisions could be achieved in principle in three-dimensional lattices with a filling factor of one atom per each species [154, 155]. Atom-dimer collisions are reduced as well as dimer-dimer collisions due to the finite potential barrier between two neighbouring potential wells. In such systems the intrinsic lifetime can be measured directly.

5.3.4 Modulation amplitude dependence

As shown in section 5.1, Feshbach molecules are associated when the modulation frequency ω is resonant to the binding energy $E_b = \hbar\omega$ of the molecules assuming an atomic cloud with zero temperature. However, the measured binding energy for a fixed dc-magnetic field shows a dependence on the modulation amplitude shown in figure 5.9. This can be easily understood by regarding the quadratic behaviour of the binding energy in the universal regime, which is $E_b = \kappa(B - B_0)^2$ with curvature κ . The time-dependent magnetic field including a sinusoidal modulation around the dc-magnetic field B_{dc} is given by $B(t) = B_{dc} + b \sin \omega t$ according to equation (5.4). The effective binding energy is given by the time average of the binding energy considering the modulated

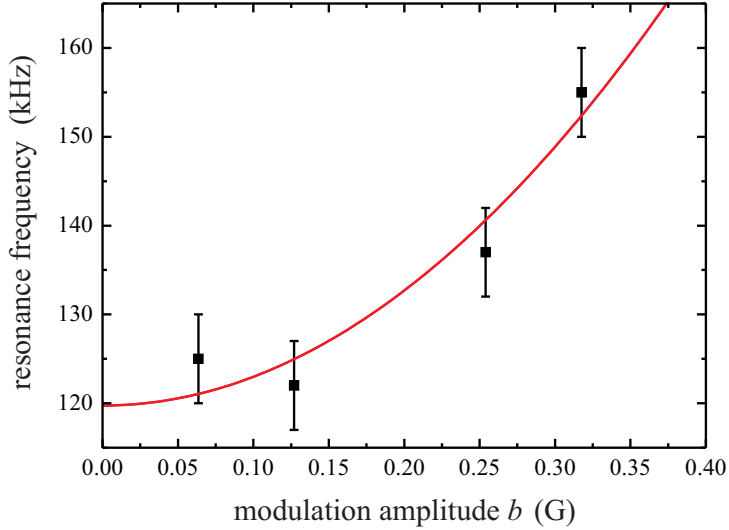


Figure 5.9: Resonance frequency for a fixed dc-magnetic field B_{dc} of 78.30 G in dependence on the amplitude b of the magnetic field modulation. A quadratic behaviour is observed due to the quadratic dependence of the binding energy on the magnetic field in the universal regime. The red solid line represents a parabolic fit.

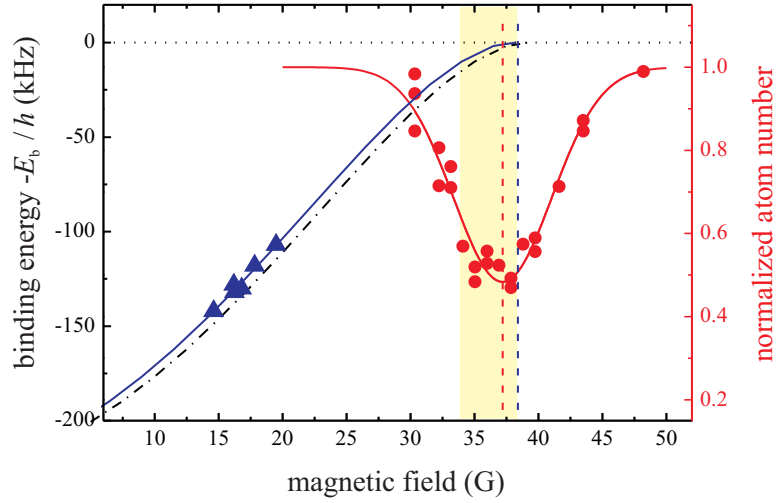
magnetic field

$$\langle E_b \rangle = E_b(B_{\text{dc}}) + \kappa b^2/2. \quad (5.21)$$

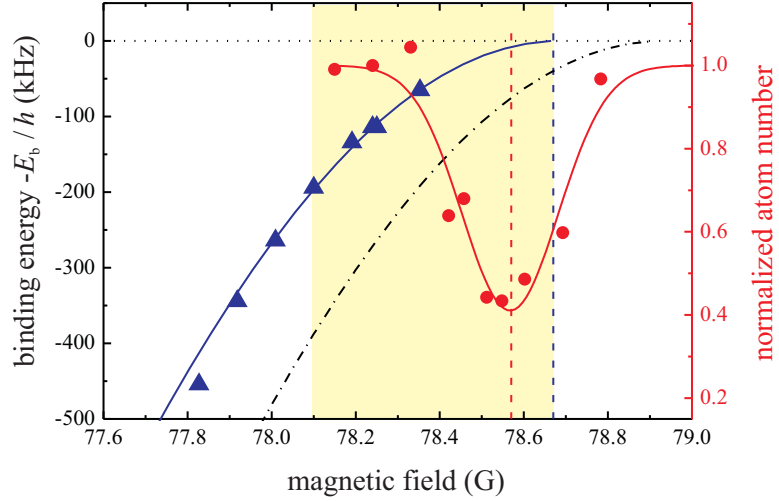
The frequency shift induced by the modulation is proportional to the square of the modulation amplitude b . Experimentally the quadratic dependence of the binding energy on the modulation amplitude is proved. Figure 5.9 shows the resonance position for the same magnetic field depending on the modulation amplitude. Hence, to determine and plot the binding energy depending on the magnetic field in figure 5.10(a), the measured binding energy of each dataset is extrapolated to a zero modulation amplitude.

5.3.5 Binding energy and Feshbach position

Taking into account all the different corrections and systematic effects affecting the binding energy, it can be determined for different magnetic fields. The result is plotted in figure 5.10(a) and 5.10(b) as blue triangles for both of the s -wave Feshbach resonances [156]. In the experiment we also observe loss features at half the resonance frequency. Numerical integration of equation (5.8) confirms the observed occurrence of molecule association at fractional resonance frequencies. This effect is used to extend the accessible association range to frequencies above the bandwidth of the modulation coil. In addition to the measured binding energy values, the theoretically predicted binding energy is plotted in figure 5.10(a) and 5.10(b). The black dashed line corresponds to the results of the collisional model published in [92]. The measured binding energies



(a) Binding energy of the KRb dimers in the vicinity of the broad Feshbach resonance at 38 G



(b) Binding energy of the KRb dimers in the vicinity of the narrow Feshbach resonance at 79 G

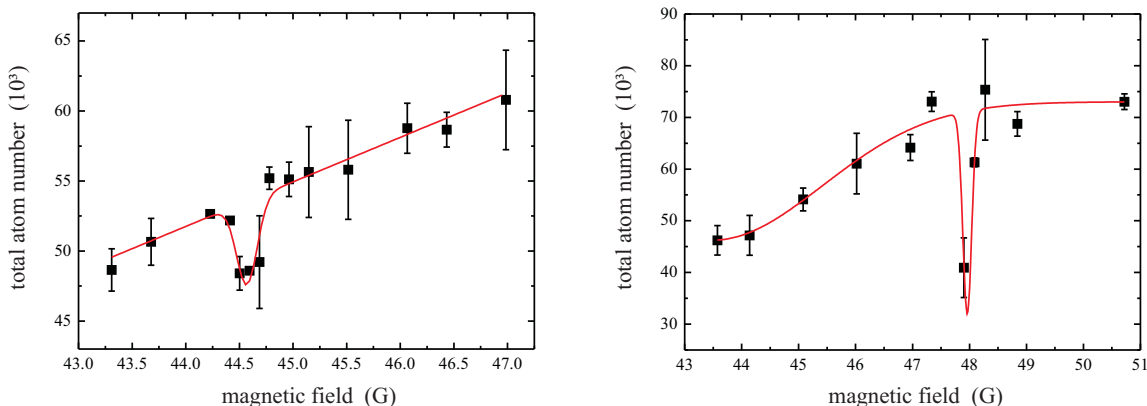
Figure 5.10: Binding energy of the KRb dimers in the vicinity of two Feshbach resonances at around 38 G and 79 G, respectively: The blue triangles are the measured binding energies and the red dots the remaining number of atoms of a three-body loss measurement. The black dot-dashed line and the blue solid line show the theoretically predicted binding energy and the same line shifted by -1 G for the FR at 38 G and by -0.24 G for the FR at 79 G, respectively. The solid red line represents a Gaussian fit to the remaining number of atoms. The Feshbach positions, determined by the loss and binding energy measurement, are indicated with the vertical red and blue dashed lines, respectively. The yellow region marks the universal regime for $a > 0$.

deviate obviously from the theoretically predicted ones. Shifting the theoretically predicted resonance position by -1 G for the broad Feshbach resonance and by -240 mG for the narrow resonance without changing the shape of the binding energy curve, the measured data are well described by the theory. Extrapolating the binding energy to its zero crossing, the Feshbach resonance positions are determined to be 38.4 G and 78.67 G, respectively, with an uncertainty of ± 30 mG. In addition, the two graphs show the three-body loss measurements according to the Feshbach resonances. The resonance positions resulting from the centre of a Gaussian fit deviate by 1 G and 100 mG, respectively, from the binding energy measurements. The latter one is in-between the three-body recombination and the theoretical predictions. We have not systematically analyzed the dependence of the Feshbach resonance position on an AC-Stark shift [157]. However, assuming an almost perfect linear polarization of the dipole trap beams, the differential AC-Stark shift is of the order of several tens of Hz and thus may be neglected.

Considering the measured binding energy evolution as a function of the magnetic field, the Feshbach resonances can be characterized more precisely. As discussed in chapter 2.3, Feshbach resonances are divided into entrance and closed channel dominated resonances. Applying equation (2.32), the dimensionless parameter η is about 15 for the broad resonance at $B_0 = 38.4$ G and about 5 for the narrow resonance at 78.7 G. Hence, none of the two resonances can be unambiguously attributed to one of the classes, but tend to be closed channel dominated. Although the width of the resonance at 38.4 G exceeds the one at 78.67 G by one order of magnitude, the parameter η is even larger in the first case due to the small magnetic moment $\mu_{\text{res}} = 4.4 \cdot 10^{-3} \mu_B$ compared to $\mu_{\text{res}} = 0.53 \mu_B$ for the narrow resonance. This information already gives a hint at the coupling strength of both resonances. The smaller η and the larger μ_{res} the stronger the coupling between the entrance and the closed channel will be. Experimentally, the RF modulation time for the broad resonance was about two orders of magnitude larger than for the narrow one, in addition to a three times larger modulation amplitude. For verification we calculate the universal regime of both resonances which is estimated by equation (2.33) of section 2.3.4. Here, the universal regime of the positive scattering length side is approximately limited to the magnetic field region from 33.9 G to 38.4 G and 78.1 G to 78.67 G respectively. Hence, all data taken for the broad resonance are obviously outside the universal regime, whereas the data points of the narrow resonance are within or close to the universal regime. Regarding figure 5.10(a) and 5.10(b), this fact is confirmed as the data points of the narrow resonance are located within the region of the quadratic dependence of the binding energy on the magnetic field, whereas the other data set is taken in the linear regime, in which the closed channel admixture becomes significant and the coupling strength decreases.

5.3.6 Conclusion

A precise knowledge of the molecular potentials is required to produce rovibrational ground state molecules. Information and input to theoretical calculations are usually given by Feshbach spectroscopy measurements. Additionally, also the binding energy



(a) Atom losses due to the d -wave Feshbach resonance: The fit of a Gaussian line shape on a linear pedestal yields a Feshbach resonance position of 44.58 G with a FWHM of 100 mG.

(b) Atom losses due to the d -wave Feshbach resonance: The fit of a narrow Gaussian line shape on a broad Gaussian pedestal yields a resonance position of 47.96 G with a FWHM of 80 mG.

Figure 5.11: Enhanced three-body recombination losses at the position of two inter-species d -wave Feshbach resonances of K-Rb each in the ground state $|f = 1, m_f = 1\rangle$.

measurements of weakly bound dimers in the vicinity of these Feshbach resonances give important information on the resonance position. As discussed above, the Feshbach resonance position can be extrapolated by the zero crossing of the vanishing binding energy. This measurement method is much more precise as systematic shifts can be neglected. In particular, for broad Feshbach resonances, loss measurements are inaccurate. For large scattering lengths the unitarity limit comes into play, which corresponds to a constant scattering length above a threshold value. In addition, a temperature dependent shift of the Feshbach resonance has to be considered. Shallow dimers produced on the positive scattering length side by three body recombination can undergo elastic collisions in the presence of a large potential trapping depth before they leave the trap. During this process the kinetic energy gained due to the binding energy difference is shared to the colliding particles. This leads to a heating of the ensemble and due to the finite trap depth to evaporation and additional atom losses. An asymmetric loss feature results, which hampers a precise determination of the resonance position. Hence, the results from associating KRb molecules can be used to improve the collisional model. Additional information can be obtained by including further resonances belonging to different closed channels as well as by including higher order Feshbach resonances.

5.4 Higher order Feshbach resonances

In the experiment we observe two narrow loss features at magnetic fields of 44.58(0.05) G and 47.96(0.02) G [80]. At these magnetic fields, no s -wave Feshbach resonances are expected. These resonances are measured at temperatures of about 400 nK and 450 nK

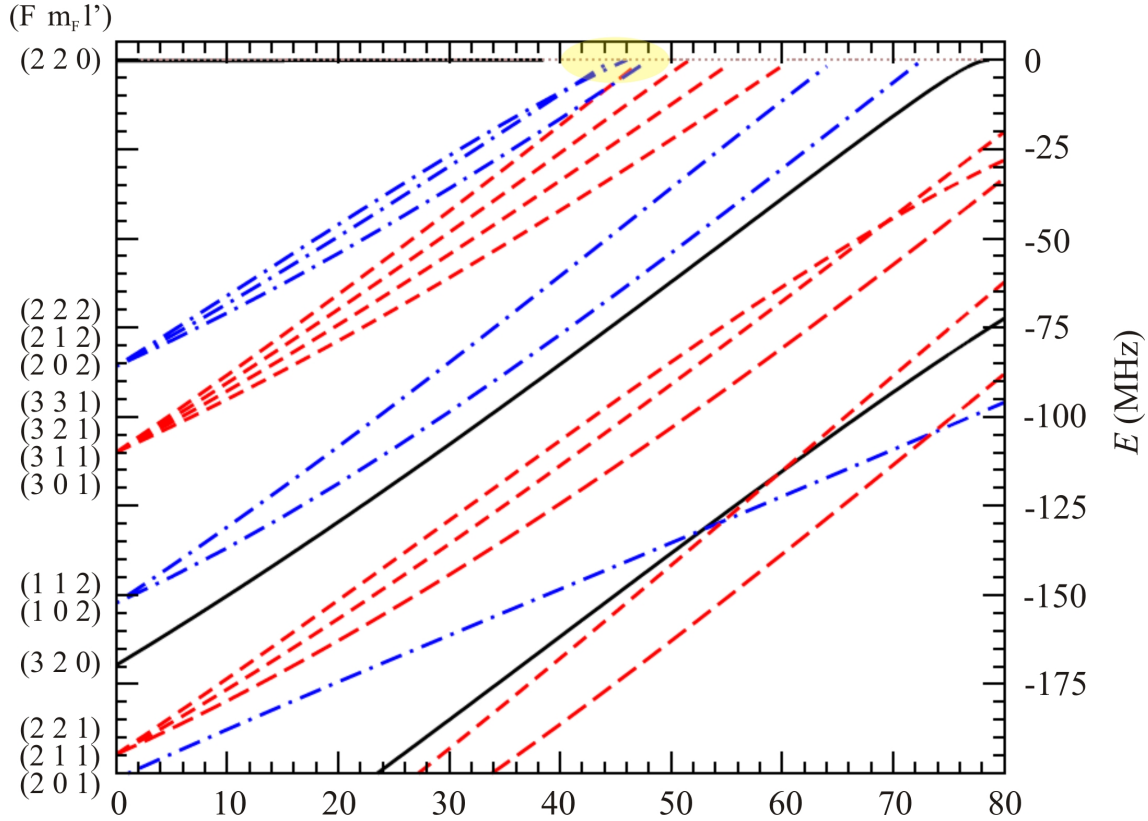


Figure 5.12: Molecular levels scheme calculated by A. Simoni [80]: Molecular levels crossing the dissociation threshold of two Rb and K atoms each in the atomic $|f, m_f\rangle = |1, 1\rangle$ state. Considered are s -wave (black solid line), p -wave (red dashed line) and d -wave (blue dashed-dotted line) of the molecular state. The relevant region is highlighted yellow.

respectively. The mixture of K and Rb is produced as described in detail in section 5.3. Both species are stored in the crossed optical dipole trap in their absolute ground states $|f, m_f\rangle = |1, 1\rangle$. The remaining total number of atoms ($N_K + N_{Rb}$) is measured after 100 ms holding time at a fixed magnetic field. To prove this loss being due to a heteronuclear effect, these measurements are also done for both species separately, with no loss peaks being detected. The width of these resonances is 100 mG and 80 mG, respectively. The magnetic field resolution is 20 mG, and the day-to-day fluctuation is about 50 mG. The latter limits the reproducibility, whereas a daily calibration of the magnetic field by microwave-driven hyperfine transitions can reduce this uncertainty. More narrow features can not be detected and resolved.

For Feshbach resonances a coupling of the closed and entrance channel occurs due to different interaction types, which are spin exchange and dipolar relaxation interactions. As a preselection, incoming atom pairs with an angular momentum $l \gg 1$ can be excluded in our system. For a non-vanishing orbital quantum number a centrifugal barrier proportional to $l(l+1)$ arises. Hence, higher order partial wave collisions are suppressed

entrance channel $ f, m_f, l, m_l\rangle$	molecular state $ F', m_{F'}, l', m_{l'}\rangle$					
	spin- exchange interac- tion $\Delta l = 0$ $\Delta m_l = 0$	dipole-dipole interaction				
		$\Delta l = 0$ $\Delta m_l = 1$	$\Delta l = 2$			
		$\Delta m_l = 0$	$\Delta m_l = 1$	$\Delta m_l = 2$	$\Delta m_l = 3$	
$ 1, 1, 0, 0\rangle$	$ 3, 2, 0, 0\rangle$		$ 2, 2, 2, 0\rangle$ $ 3, 2, 2, 0\rangle$	$ 2, 1, 2, 1\rangle$ $ 3, 1, 2, 1\rangle$	$ 2, 0, 2, 2\rangle$ $ 3, 0, 2, 2\rangle$	
$ 1, 1, 1, 0\rangle$	$ 3, 2, 1, 0\rangle$	$ 2, 1, 1, 1\rangle$ $ 3, 1, 1, 1\rangle$	$ 2, 2, 3, 0\rangle$ $ 3, 2, 3, 0\rangle$	$ 2, 1, 3, 1\rangle$ $ 3, 1, 3, 1\rangle$	$ 2, 1, 3, 1\rangle$ $ 3, 1, 3, 1\rangle$	$ 2, -1, 3, 3\rangle$ $ 3, -1, 3, 3\rangle$
$ 1, 1, 1, 1\rangle$	$ 3, 2, 1, 1\rangle$	$ 3, 3, 1, 0\rangle$	$ 2, 2, 3, 1\rangle$ $ 3, 2, 3, 1\rangle$	$ 2, 1, 3, 2\rangle$ $ 3, 1, 3, 2\rangle$ $ 3, 3, 3, 0\rangle$	$ 2, 0, 3, 3\rangle$ $ 3, 0, 3, 3\rangle$	

Table 5.1: A selection of possible coupled channels for ultracold incoming ^{41}K and ^{87}Rb atoms, each in the atomic state $|f, m_f\rangle = |1, 1\rangle$. The ultralow temperature of the two species restricts the scattering of the incoming particles to be *s*- or *p*-wave.

for temperatures in our case, as discussed in chapter 2. *P*-wave Feshbach resonances ($l=1$) of the colliding atoms were already observed in fermionic $^6\text{Lithium}$ down to a minimum temperature of $6\ \mu\text{K}$ [158]. These considerations restrict the possible entrance channels to be $|f_1, m_{f_1}, f_2, m_{f_2}, l\rangle = |1, 1, 1, 1, 0\rangle$ or $|1, 1, 1, 1, 1\rangle$, where $m_l=0..l$. A selection of possible entrance-closed channel combinations and the corresponding coupling mechanism are listed in Table 5.1. Using the model of [92], Andrea Simoni calculates the molecular level scheme for $^{41}\text{K}^{87}\text{Rb}$ relative to the dissociation threshold of the two atoms in the atomic $|1, 1\rangle$ -state plotted in figure 5.12. The calculations predict four different level crossings between 40 and 50 G. All of them belong to molecular states with $l'=1$ or 2. According to section 2.1 the selection rules for spin exchange collisions are $\Delta l=0$ and $\Delta m_F = 0$. The spin-spin and spin-orbit collisions obey $|\Delta l| = 0, 2$ and $\Delta m_F + \Delta m_l = 0$ which corresponds to a redistribution of the angular momenta. Hence, molecular states with an orbital quantum number of two can only couple by spin exchange interaction to $l=2$ or by dipolar relaxations to $l=0, 2$. An angular momentum of $l = 2$ for the incoming atoms can be excluded for ultracold temperatures. Therefore, the

feature at 44.6 G is attributed to a d -wave resonance which occurs due to dipole-dipole interactions, whereas the molecular state can be $|F, m_F, l', m_{l'}\rangle = |2, 2, 2, 0\rangle$ or $|2, 1, 2, 1\rangle$ according to figure 5.12. The second feature can be attributed to the d -wave resonance with the molecular state $|2, 0, 2, 2\rangle$ or to the p -wave resonance belonging to the state $|3, 3, 1, 0\rangle$. The latter possibility occurs due to a spin-spin collision with $\Delta l = 0$, which would couple the molecular state to an initial state of $|f, m_f, l, m_l\rangle = |1, 1, 1, 1\rangle$. In this case the stronger spin exchange coupling should lead to a further loss peak at about 52 G, which cannot be observed. Moreover, the typical doublet structure of p -wave Feshbach resonances generated by the magnetic dipole-dipole interaction is not visible. The resonance feature would split up to two peaks belonging to $|m_l| = 1$ and $m_l = 0$, as Ticknor et al. proved in [159]. This leads to the conclusion that both narrow resonances are attributed to d -wave resonances.

These newly observed resonances, together with the binding energy measurement, are used for an improved collision model of the inter-species interaction potential. In combination with the results of the two isotopic pairs [92], $^{40}\text{K}^{87}\text{Rb}$ and $^{39}\text{K}^{87}\text{Rb}$, we thus obtain for the singlet scattering length $a_s = -109.6(2) a_0$, for the triplet scattering length $a_t = -213.6(4) a_0$ and for the van-der-Waals coefficient $C_6 = 4288(2) E_h a_0^6$, where E_h is the Hartree energy.

The improvement of the parametrization of the KRb molecular potential and the production of weakly bound KRb dimers provide a good starting point to create dipolar KRb molecules in their rovibrational ground state.

6 Conclusion and outlook

6.1 A single Cs atom immersed in a Rb BEC

Significant steps have been achieved towards a controlled immersion of single Cs atoms in a Rb BEC. This final goal requires to simultaneously store both species with a considerable overlap of their wave functions, to independently manipulate them in a controlled way, and to detect them. In particular a strong confinement of the Cs atom is necessary in order to precisely localize the atom within the BEC, enabling the atom to position-dependently probe the properties of the BEC. In addition, adjusting the intra- and inter-species interaction is an essential demand for further experiments.

In this thesis I have presented the realization of the first experimental steps. Both components have been trapped and detected: a Rb BEC and a probabilistic single atom source. Furthermore, we have employed single atoms and their dynamics in a MOT as a non-destructive probe to extract the inter-species interaction parameters of a two-species MOT. Although single Rb atoms are lost due to collisions with single Cs atoms, the overall state of $\approx 10^3$ Rb atoms remains unaltered. Here, the interaction is dominated by light induced collisions which involve higher electronic states [160]. In further experiments we aim on investigating and utilizing ground state collisions which are of interest in, e.g., quantum information processing.

So far, the Rb BEC and the single atom MOT are spatially separated by 7 mm due to the different magnetic field minima of the quadrupole and QUIC traps. Meanwhile, the trap centres of both species have been spatially overlapped by a combination of magnetic transport and an overlapped dipole trap at the centre of the quadrupole trap, which corresponds to the position of the Cs atoms in the MOT. Here, the Rb atoms are stored in a purely optical trap and are transferred into a magnetic insensitive state. Thus, it is possible to load Cs atoms into a high gradient MOT, without deforming or disturbing an already existing condensate.

In contrast, control over the position of the atom and the inter-species interaction is still lacking. The former we plan to achieve by storing the Cs atoms in a species-selective optical lattice. Here, a strong confinement and large trapping frequencies will enable us to localize the atoms inside one potential well corresponding to a volume with an extent of less than $\lambda/2$ in the case of a three-dimensional lattice. In the ideal case, the species-selectivity implies that the lattice does not affect the BEC, thus allowing to probe the undisturbed BEC. This poses an enormous challenge, as the temperatures of both components differ by three orders of magnitude. They are of the order of $T_{\text{Cs}} = 100 \mu\text{K}$

for Cs and $T_{\text{Rb}} = 100 \text{ nK}$ for Rb. Thus, we have to find trapping parameters which offer a sufficient depth for Cs without affecting Rb, thus $U_{\text{Rb}}/U_{\text{Cs}} \ll T_{\text{Rb}}/T_{\text{Cs}}$, where U_i denotes the trap depth of species i . Two different types of species selective traps have been identified by LeBlanc et al. [161]. The first type uses a near red detuned wavelength close to the Cs D1- and D2-line, the second exploits a *magic* wavelength in-between the D1- and D2-lines of Rb, where the dipole potential for Rb vanishes. In the first case a small but non-zero potential for Rb remains resulting in a periodic structure of the condensate. From the second type, however, ideally no dipole potential for Rb arises. Nevertheless, the scattering rate of Rb is not negligible and can be estimated to be about 500 Hz for a trapping depth of $500 \mu\text{K}$ for Cs. Furthermore, the lattice laser wavelength is blue detuned with respect to the Cs D1- and D2- transitions. Thus, Cs is trapped in the antinodes, thereby decreasing the photon scattering. However, an additional transverse confinement is inevitable here to ensure a stable trapping configuration.

Storing Cs and Rb purely optically allows us to use the magnetic field as a free parameter and to make use of magnetic Feshbach resonances to tune the inter-species interaction strength and choose its character. K. Pilch et al. [162] investigated a series of Rb-Cs Feshbach resonances within the magnetic field range of 30 to 300 G. Here, for both species in the ground state the observed resonance at 180 G is of special interest, due to its relatively large width of 3 G. Probably, this will allow us to tune the Rb-Cs scattering length continuously about several orders of magnitude including changing its sign.

6.1.1 Cooling a single Cs atom to its motional ground state

Various theoretical proposals in quantum information processing and quantum computation suggest a single atom to be prepared as a quantum bit (qubit) with two logic states $|0\rangle$ and $|1\rangle$. Experimentally, these qubit states may correspond to different spin states. As the qubit can interact with the environment, the quantum information stored, i.e. the internal state and/or the relative phase between the two states, can be lost. The typical time period in which the coherence of the quantum system decays should therefore be as long as possible. In our system, one of the main decoherence sources of trapped single atoms is related to the temperature of the atom [35]. A possible cooling scheme has been proposed, where a qubit (single Cs atom) is immersed in a BEC, thereby cooling the qubit to the motional ground state of the trap [44, 45]. In this case, the BEC acts as a cooling bath for the single atom. Recently, Daley et al. [44] have predicted a type of sympathetic cooling of the single atom without changing its internal state. The kinetic energy of the atom is decreased by creating Bogoliubov excitations inside the BEC. Assuming the single atom to be confined in a potential well of a standing wave or a three-dimensional lattice with a trapping frequency ω , the energy of the n^{th} vibrational level is given by $n \hbar \omega$. Depending on the ratio between the energy spacing in the trap $\hbar \omega$ and a typical energy scale of the superfluid $m_{\text{Rb}} u^2/2$ given by the sound velocity, Daley et al. [44] distinguish between two cooling regimes, the subsonic $\hbar \omega \ll m_{\text{Rb}} u^2/2$ and the supersonic $\hbar \omega \gg m_{\text{Rb}} u^2/2$.

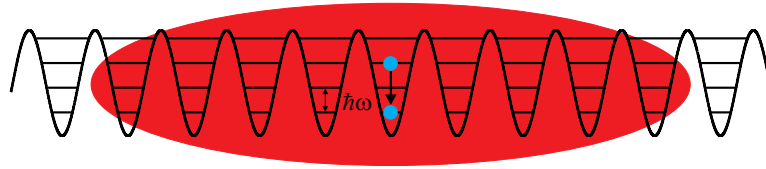


Figure 6.1: Sympathetic cooling of a single atom by a BEC (red): A single atom (blue dot) is confined in a standing wave with a trapping frequency ω . Via Bogoliubov excitations the atom is cooled from a highly excited vibrational state to the motional ground state. The black lines indicate the vibrational energy levels of the standing wave.

In the supersonic regime, the single atom oscillation velocity exceeds the speed of sound u in the BEC, resulting in particle-like Bogoliubov excitations. Here, the single atom in an initially high vibrational level can be de-excited by more than one level spacing into the motional ground state. In contrast, in the subsonic regime, an atom can only be de-excited to the next lower vibrational level. Within this regime the Bogoliubov excitation of the condensate is phonon-like and corresponds to the low energy part of the Bogoliubov spectrum. This situation is similar to the Raman side band cooling of ions [163] within and beyond the Lamb-Dicke regime [164, 165]. In order to enter the supersonic regime to efficiently cool the atom, the trapping frequency of our Cs trap must exceed $2\pi \cdot 400$ Hz by far.

The minimum temperature obtained by such a cooling process is given by the condensate temperature. Thus, the temperature of the cooling bath has to be well below $\hbar\omega$ to make sure the atom can be cooled down to the vibrational ground state of the trap. Hence, assuming a BEC temperature of 100 nK, the trapping frequencies should be chosen to be even larger than $2\pi \cdot 2$ kHz in order to cool the atom into the motional ground state.

The time scale of the cooling process can be adjusted by the interaction strength between the single Cs atom and the Rb BEC. The larger the inter-species s -wave scattering length, the more efficient the cooling.

Furthermore, this technique might not only allow to cool a qubit without changing its internal state, but also to cool entangled atom pairs while their entanglement is preserved. For these experiments, appropriate initial internal qubit states have to be chosen, so that the respective inter-species interaction strengths between each of the two qubit states and the BEC are the same. If this requirement is not met, the asymmetric interaction leads to entanglement of the single qubits with the bath which results in apparent decoherence of the two entangled qubits.

6.1.2 Probing the decoherence of a Rb BEC by a single Cs atom

Another intriguing application of a single atom immersed in a BEC is to employ the single atom as a probe, e.g. to investigate the decoherence of the Rb BEC [33]. The decoherence of a system originates from interaction with its environment, which can

be, e.g., inelastic collisions with background atoms and photon scattering. H. T. Ng et al. [33] proposed a decoherence detection method, where a single atom prepared in a superposition of two qubit states $|0\rangle$ and $|1\rangle$ is immersed in a BEC. The BEC is predominantly coupled to one of the two qubit states. The ensuing time evolution leads to an entanglement between the atom and the BEC. Assuming an ideal system without decoherence the two components periodically entangle and dis-entangle, similar to the entanglement oscillations observed in a Mott-insulator [13]. The oscillation period is inversely proportional to the inter-species interaction strength. For decoherence, the oscillation period remains constant, thus the dis-entanglement occurs after the same probing time. However, the decoherence of the BEC is imprinted on the phase between the single atom qubit states. A $\pi/2$ -pulse maps the phase information between the two states onto the populations. This decoherence measurement requires the coherence time of the probe, the single atom, to exceed both the coherence time of the BEC and the interaction time by orders of magnitude. In order to reduce the interaction time, the inter-species s -wave scattering length can be increased via a Feshbach resonance. By means of a Feshbach resonance also temporal limits of the interaction time can be set by tuning the interspecies interaction strength to zero.

6.2 Heterospecies dimers and trimers

6.2.1 Molecules in the rovibrational ground state

Heteronuclear molecules in the rovibrational ground state of the singlet and triplet potentials provide a permanent dipole moment. Their anisotropic, long-range dipole-dipole interaction forms the basis for further experiments, such as the investigation of new quantum phases [49] or the production of dipolar BECs [47]. The associated KRb dimers presented in this thesis provide the first step towards these dipolar molecules. In order to transfer the weakly bound molecules to their ground state a sufficiently long lifetime of the weakly bound molecular ensemble is required. Associating the molecules in the overlapping regime of the two atomic clouds, their lifetime is limited by inelastic atom-molecule collisions. This limit can be overcome if the two species are trapped in a three-dimensional lattice with a filling factor of unity per species, meaning one atom of each species per lattice site [154, 155]. After the association of molecules in this Mott-insulator-like system there will be exactly one KRb molecule per lattice site. A sufficient potential barrier between two neighbouring sites suppresses tunnelling, thereby avoiding inelastic atom-dimer and dimer-dimer collisions. Thus, the lifetime of these molecules is only limited by internal relaxation.

These molecules can be transferred to the rovibrational ground state from their initially highly excited state by, e.g., the application of a stimulated Raman adiabatic passage [166] (STIRAP). This technique is much more robust than Rabi pulses and has been already successfully applied for $^{87}\text{Rb}_2$ -dimers [67] as well as for fermionic $^{40}\text{K}^{87}\text{Rb}$ -dimers [68]. It is based on the coherent coupling between the weakly bound state and the rovi-

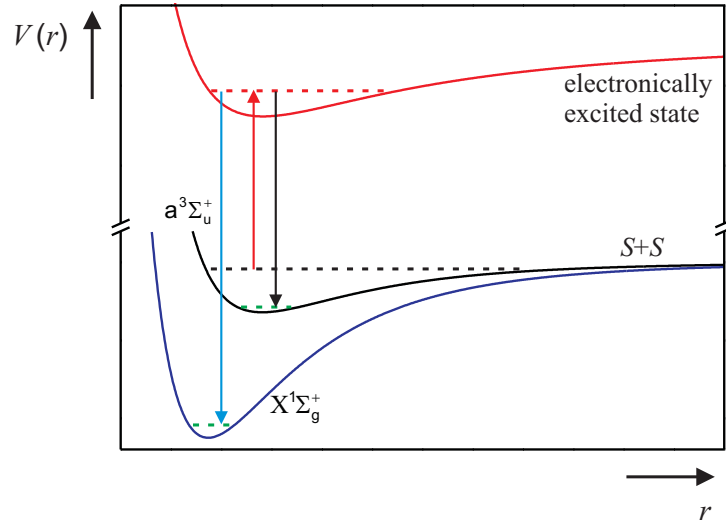


Figure 6.2: Schematic of the STIRAP technique: The blue and the black line indicate the singlet and triplet potential of the electronic ground state, respectively. An electronically excited state providing the required dark state is drawn as a red line. The dashed lines denote the weakly bound molecular state (black), the rovibrational ground states (green) and the dark state (red). The arrows mark the driven transitions.

brational ground state via an electronically excited state applying a counter-intuitive pulse sequence [166]. A cold molecular cloud is obtained with a temperature corresponding to the initial temperature of the weakly bound molecules. While the molecules are coherently transferred, the phase space density remains constant. The molecular potentials of K-Rb have to be precisely known to select appropriate frequencies to efficiently drive the transfer. Strong coupling is achieved if the frequencies match the resonance frequencies of the driven transitions close to a turning point. This results in a large Franck-Condon factor given by the overlap integral of the wave functions. This emphasizes the importance of an improved collisional model, as already mentioned above, by a more precise determination of the s -wave Feshbach resonance positions and by detecting higher order Feshbach resonances.

6.2.2 From dimer to trimer states

Already in 1970, V. Efimov predicted the existence of an infinite series of weakly bound trimer states when the two-body scattering length approaches infinity [91]. These trimer states appear for a system of three particles with pairwise resonant two-body interactions. Figure 6.3 schematically shows an energy diagram of the trimer states in the vicinity of a Feshbach resonance. The trimer states connect the positive and negative scattering length sides by crossing the singularity of the Feshbach resonance. For a

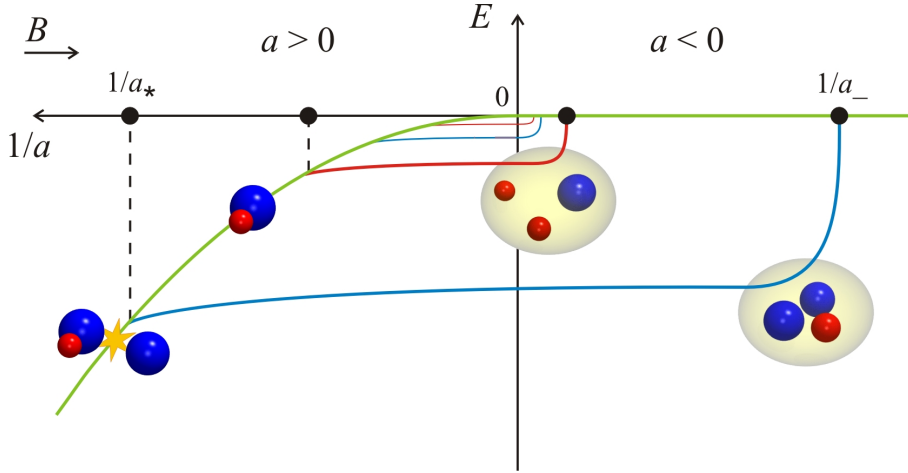
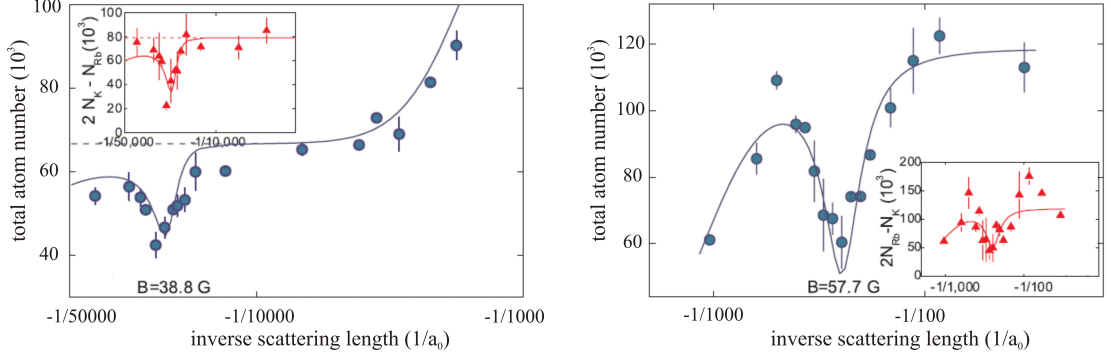


Figure 6.3: Schematic of an energy diagram with Efimov states for a K-Rb mixture around a K-Rb Feshbach resonance. The position of the Feshbach resonance corresponds to the singularity at $1/a = 0$. The green line shows the dissociation threshold of three free atoms for $a < 0$ and the atom-dimer threshold for $a > 0$. Two series of Efimov states, i.e. KRbRb and KKRb are indicated by the blue and red line, respectively. Here, $1/a_*$ and $1/a_-$ mark the Efimov resonances occurring at the atom-dimer threshold for $a > 0$ and at the dissociation threshold of three free atoms for $a < 0$. The blue and red spheres indicate the Rb and K atoms, respectively.

vanishing trimer binding energy, the trimer state intersects the dissociation threshold of three free atoms on the negative scattering length side. On the positive scattering length side, the same trimer state intersects the dimer-atom threshold featuring a parabolic behaviour as a consequence of the a^{-2} dependence of the dimer binding energy in the universal regime. Similar to the weakly bound molecules, the trimer states also exhibit universal properties. As in the two-body system this means that their properties are independent of the short-range interaction potential. More precisely, increasing the two-body scattering length, these Efimov states periodically appear in powers of the universal scaling factor $\exp(\pi/s_0)$, whereas their binding energy decreases in powers of $\exp(-2\pi/s_0)$. The dimensionless parameter s_0 is predicted to be 1.00624 in the case of three identical particles [167]. Experimentally, these trimer states can be detected as increased three-body recombination losses, when the trimer state intersects the dissociation thresholds. Here, the occupation of the trimer state is resonantly enhanced. The extremely weakly bound trimers quickly decay into deeply bound dimers, thereby converting the released difference in binding energy into kinetic energy. It is shared between the constituents, leading to trap loss. On the positive scattering length side an oscillating behaviour of the three-body recombination rate, with a minimum between two intersection points, is predicted [86, 169] and has already been experimentally observed [12, 170]. Here, weakly bound dimer states exist, as seen in chapter 5. Hence, the trimer can decay into shallow as well as deeply bound dimers.

The first Efimov resonance for $a < 0$ and a three-body recombination minimum for $a > 0$ have been detected by T. Krämer et al. [12] using ultracold bosonic Cs atoms, although



(a) Inelastic atom losses due to an Efimov resonance at 38.8 G attributed to a KKRb trimer state. The remaining total atom number of both species after a hold time of 100 ms is plotted as a function of the scattering length. The temperature of the atomic cloud is measured to be 300 nK. The inset shows the linear combination $2N_K - N_{Rb}$ to support the channel assignment.

(b) Inelastic atom losses due to an Efimov resonance at 57.7 G attributed to a KRbRb trimer state. The remaining total atom number of both species after a hold time of 500 ms is plotted as a function of the scattering length. The temperature of the atomic cloud is measured to be 400 nK. The inset shows the linear combination $2N_{Rb} - N_K$ to support the channel assignment.

Figure 6.4: Two Efimov resonances observed for negative scattering length in the vicinity of the K-Rb Feshbach resonance at 38 G. The solid lines refer to the numerical calculations in [168].

the trimer states were originally predicted in the field of nuclear physics. However, in these systems the observation of the resonances is hampered by the strong long-range Coulomb interaction. In contrast, ultracold gases provide a clean and well-controllable system, in which the interaction is described by the s -wave scattering length a and it is widely tunable. Recently, M. Zaccanti et al. could measure a first series of Efimov states [170].

Efimov trimers are not limited to three pairwise resonant interactions, but can also appear for two pairwise resonant interactions of a three-body system [94]. This implies the existence of heteronuclear Efimov resonances in two-component mixtures, as our system of bosonic K and Rb. As a consequence, there are two series of heteronuclear Efimov resonances, namely KKRb and KRbRb, next to an inter-species Feshbach resonance. The intra-species scattering lengths of K and Rb remain constant and are below $100 a_0$. The universal scaling factors of these heteronuclear systems differ from the homonuclear case and are predicted to be $\exp(\pi/s_0) = 3.51 \cdot 10^5$ for KKRb and 131 for KRbRb [94]. We have already observed two Efimov resonances for $a < 0$, at a magnetic field of 38.8 G and 57.7 G in the vicinity of the broad Feshbach resonance at 38 G, which we attribute to the KKRb and KRbRb series, respectively [168]. Both three-body recombination loss peaks can be seen in figure 6.4. To make sure that inter-species three-body collisions are responsible for these loss peaks, we proved that the peaks do not appear for single species stored. In addition, for the KRbRb peak we have measured the time evolution of the decay of the two species showing an atom loss ratio of $N_{Rb}/N_K = 1.7$. Thus,

6 Conclusion and outlook

this verifies that the peak occurs due to three-body recombination and belongs to the KRbRb series of the Efimov spectrum.

In addition, we have observed one loss feature on the positive scattering length side, which we attribute to the KRbRb channel, as more Rb than K atoms are lost. Following [170] this loss peak occurs if secondary collisions between atoms and dimers produced during the three-body recombination are resonantly enhanced. By observing heteronuclear Efimov resonances we confirm that only two resonant pairwise interactions are required.

Choosing an atomic mixture with a mass ratio larger than 10, the universal scaling factor can be reduced to less than 10 [94]. Therefore, heteronuclear systems as Li-Cs and Li-Rb would allow to observe a large series of Efimov resonances.

In addition, performing the measurements within a lattice, controlled atom-dimer collisions can be investigated [171, 172].

A Properties of ^{87}Rb , ^{133}Cs and ^{41}K

A selection of the physical properties of the alkalis ^{87}Rb , ^{133}Cs and ^{41}K is given in table A.1. Figure A.1 shows the hyperfine structure of the D2 transition of the aforementioned species.

		^{87}Rb	^{133}Cs	^{41}K
mass	m (kg)	$1.4 \cdot 10^{-25}$	$2.2 \cdot 10^{-25}$	$6.8 \cdot 10^{-26}$
nuclear spin	i	$3/2$	$7/2$	$3/2$
wavelength of the D1-transition	λ_{D1} (nm)	795.0	894.6	769.9
wavelength of the D2-transition	λ_{D2} (nm)	780.2	852.3	766.5
linewidth of the D1-transition	Γ_{D1} (MHz)	$2\pi \cdot 5.75$	$2\pi \cdot 4.56$	$2\pi \cdot 6.1$
linewidth of the D2-transition	Γ_{D2} (MHz)	$2\pi \cdot 6.07$	$2\pi \cdot 5.22$	$2\pi \cdot 6.2$

Table A.1: Selection of the physical properties of ^{87}Rb , ^{133}Cs and ^{41}K taken from [138, 173, 174].

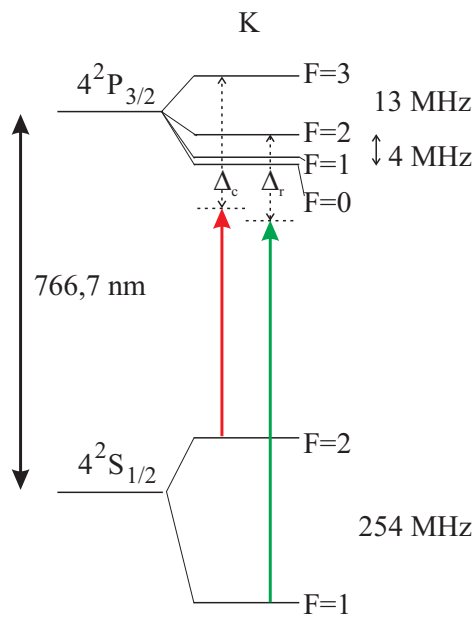
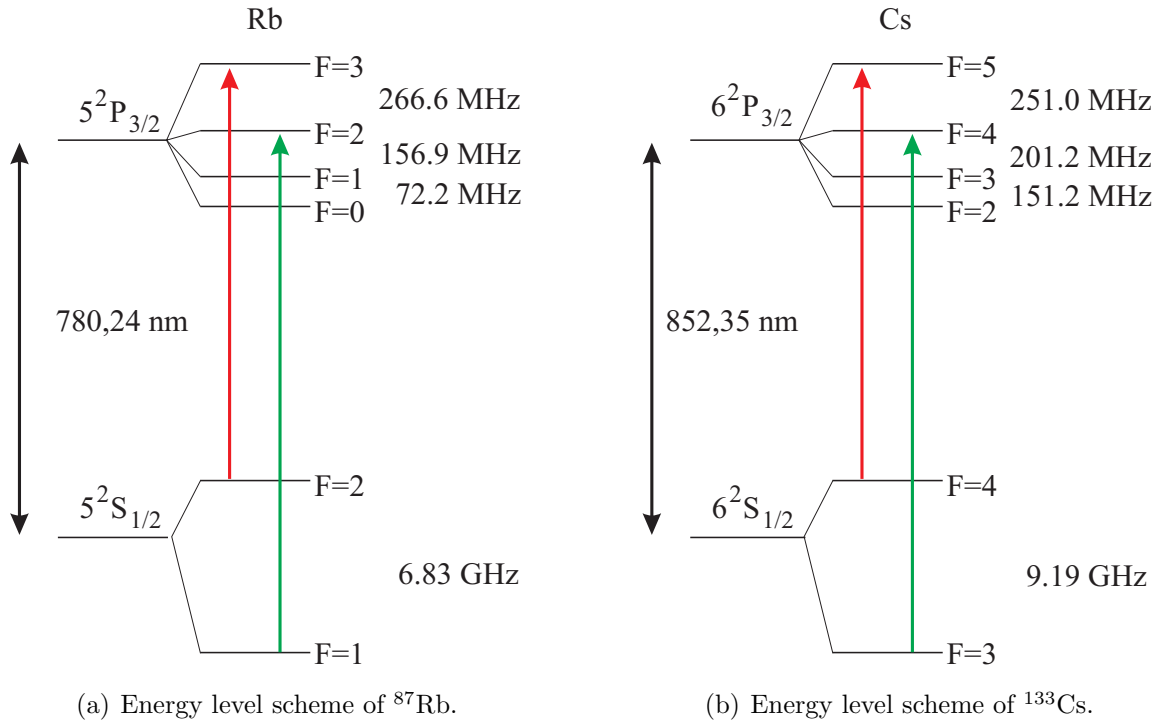


Figure A.1: Hyperfine structure of the D2 transition of ^{87}Rb , ^{133}Cs and ^{41}K . The red and green arrows indicate the cooling and repumping transitions, respectively.

B Power stabilization

A power stabilization of the dipole trap beams is built up to compensate fluctuations of the laser power as discussed in section 3.7. Figure B.1 shows a schematic of the control board of the constructed PI-controller.

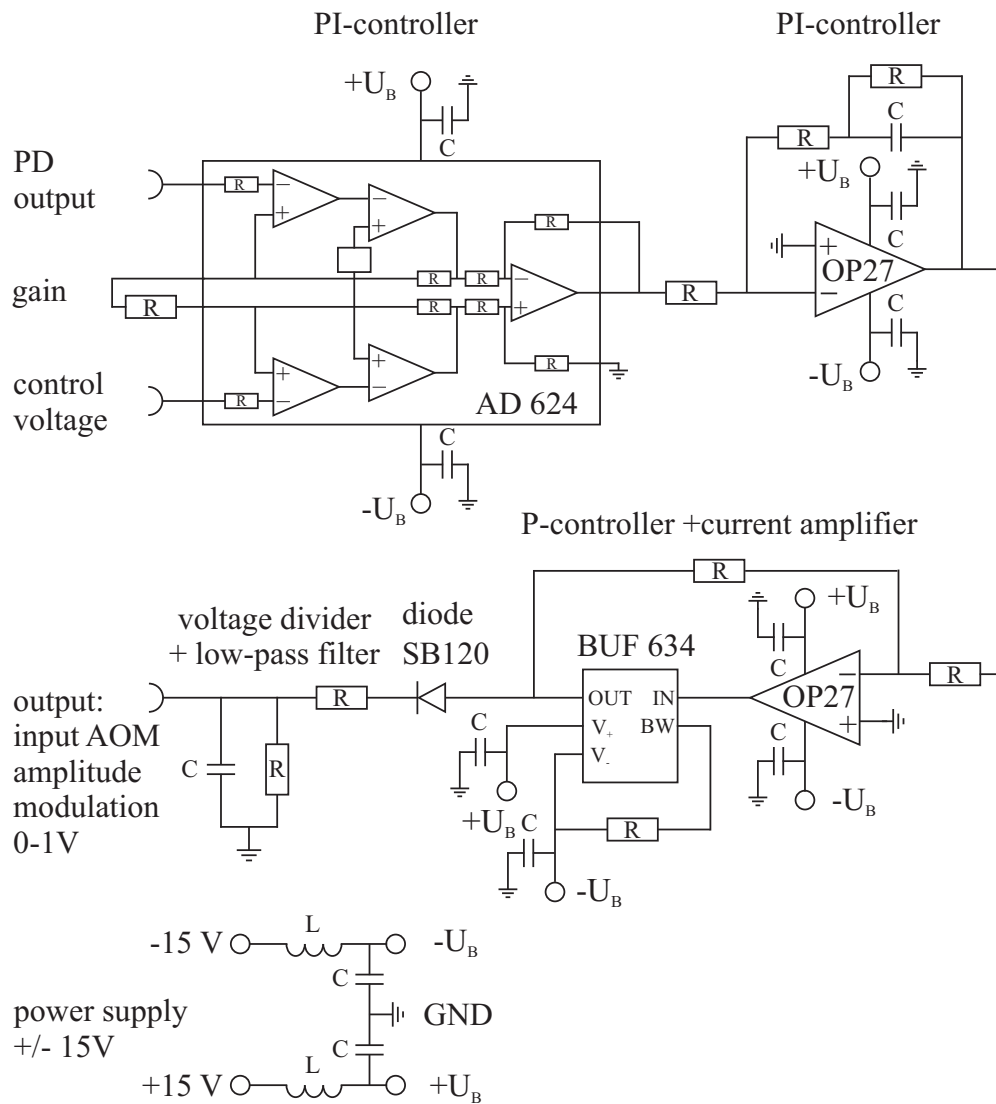


Figure B.1: Electronic schematic of the PI-controller for the Nd:YAG-laser using an AOM. Here, R, C, and L denote a resistor, a capacitor, and an inductor, respectively.

Bibliography

- [1] T. W. Hänsch and A. L. Schawlow, *Cooling of gases by laser radiation*, Opt. Commun., 13 (1975), p. 68.
- [2] H. F. Hess, *Evaporative cooling of magnetically trapped and compressed spin-polarized hydrogen*, Phys. Rev. B, 34 (1986), pp. 3476–3479.
- [3] M. H. Anderson, J. R. Ensher, M. R. Matthews, C. E. Wieman, and E. A. Cornell, *Observation of Bose-Einstein Condensation in a Dilute Atomic Vapor*, Science, 269 (1995), pp. 198–201.
- [4] K. B. Davis, M. O. Mewes, M. R. Andrews, N. J. van Druten, D. S. Durfee, D. M. Kurn, and W. Ketterle, *Bose-Einstein Condensation in a Gas of Sodium Atoms*, Phys. Rev. Lett., 75 (1995), pp. 3969–3973.
- [5] M. R. Andrews, C. G. Townsend, H.-J. Miesner, D. S. Durfee, D. M. Kurn, and W. Ketterle, *Observation of Interference Between Two Bose Condensates*, Science, 275 (1997), pp. 637–641.
- [6] J. R. Abo-Shaeer, C. Raman, J. M. Vogels, and W. Ketterle, *Observation of Vortex Lattices in Bose-Einstein Condensates*, Science, 292 (2001), pp. 476–479.
- [7] J. Billy, V. Josse, Z. Zuo, A. Bernard, B. Hambrecht, P. Lugan, D. Clément, L. Sanchez-Palencia, P. Bouyer, and A. Aspect, *Direct observation of Anderson localization of matter waves in a controlled disorder*, Nature, 453 (2008), pp. 891–894.
- [8] G. Roati, C. D’Errico, L. Fallani, M. Fattori, C. Fort, M. Zaccanti, G. Modugno, M. Modugno, and M. Inguscio, *Anderson localization of a non-interacting Bose-Einstein condensate*, Nature, 453 (2008), pp. 895–898.
- [9] M. Karski, L. Förster, J.-M. Choi, A. Steffen, W. Alt, D. Meschede, and A. Widera, *Quantum Walk in Position Space with Single Optically Trapped Atoms*, Science, 325 (2009), pp. 174–177.
- [10] M. Tinkham. *Introduction to Superconductivity*. 2nd Ed., McGraw-Hill, 1996.
- [11] R. Wynar, R. S. Freeland, D. J. Han, C. Ryu, and D. J. Heinzen, *Molecules in a Bose-Einstein Condensate*, Science, 287 (2000), pp. 1016–1019.

- [12] T. Krämer, M. Mark, P. Waldburger, J. G. Danzl, C. Chin, B. Engeser, A. D. Lange, K. Pilch, A. Jaakkola, H.-C. Nägerl, and R. Grimm, *Evidence for Efimov quantum states in an ultracold gas of caesium atoms*, *Nature*, 440 (2006), pp. 315–318.
- [13] O. Mandel, M. Greiner, A. Widera, T. Rom, T. W. Hänsch, and I. Bloch, *Controlled collisions for multi-particle entanglement of optically trapped atoms*, *Nature*, 425 (2003), p. 937.
- [14] F. K. Fatemi, K. M. Jones, and P. D. Lett, *Observation of Optically Induced Feshbach Resonances in Collisions of Cold Atoms*, *Phys. Rev. Lett.*, 85 (2000), pp. 4462–4465.
- [15] S. Inouye, M. Andrews, J. Stenger, H.-J. Miesner, D. Stamper-Kurn, and W. Ketterle, *Observation of feshbach resonances in a bose-einstein condensate*, *Nature*, 392 (1998), pp. 151–154.
- [16] M. Greiner, O. Mandel, T. Esslinger, T. W. Hänsch, and I. Bloch, *Quantum phase transition from a superfluid to a Mott insulator in a gas of ultracold atoms*, *Nature*, 425 (2002), pp. 39–44.
- [17] T. Stöferle, H. Moritz, C. Schori, M. Köhl, and T. Esslinger, *Transition from a Strongly Interacting 1D Superfluid to a Mott Insulator*, *Phys. Rev. Lett.*, 92 (2004), p. 130403.
- [18] I. B. Spielman, W. D. Phillips, and J. V. Porto, *Mott-Insulator Transition in a Two-Dimensional Atomic Bose Gas*, *Phys. Rev. Lett.*, 98 (2007), p. 080404.
- [19] T. Kinoshita, T. Wenger, and D. S. Weiss, *Observation of a One-Dimensional Tonks-Girardeau Gas*, *Science*, 305 (2004), pp. 1125–1128.
- [20] B. Paredes, A. Widera, V. Murg, O. Mandel, S. Fölling, I. Cirac, G. V. Shlyapnikov, T. W. Hänsch, , and I. Bloch, *Tonks–Girardeau gas of ultracold atoms in an optical lattice*, *Nature*, 429 (2004), pp. 277–281.
- [21] E. Haller, M. Gustavsson, M. J. Mark, J. G. Danzl, R. Hart, G. Pupillo, and H.-C. Nägerl, *Realization of an Excited, Strongly Correlated Quantum Gas Phase*, *Science*, 325 (2009), pp. 1224–1227.
- [22] B. DeMarco and D. S. Jin, *Onset of Fermi Degeneracy in a Trapped Atomic Gas*, *Science*, 285 (1999), pp. 1703–1706.
- [23] A. G. Truscott, K. E. Strecker, W. I. McAlexander, G. B. Partridge, and R. G. Hulet, *Observation of Fermi Pressure in a Gas of Trapped Atoms*, *Science*, 291 (2001), pp. 2570–2572.

- [24] S. Jochim, M. Bartenstein, A. Altmeyer, G. Hendl, S. Riedl, C. Chin, J. Hecker Denschlag, and R. Grimm, *Bose-Einstein Condensation of Molecules*, Science, 302 (2003), pp. 2101–2103.
- [25] M. W. Zwierlein, C. A. Stan, C. H. Schunck, S. M. F. Raupach, S. Gupta, Z. Hadzibabic, and W. Ketterle, *Observation of Bose-Einstein Condensation of Molecules*, Phys. Rev. Lett., 91 (2003), p. 250401.
- [26] M. Greiner, C. A. Regal, and D. S. Jin, *Emergence of a molecular Bose-Einstein condensate from a Fermi gas*, Nature, 426 (2003), pp. 537–540.
- [27] C. A. Regal, M. Greiner, and D. S. Jin, *Observation of Resonance Condensation of Fermionic Atom Pairs*, Phys. Rev. Lett., 92 (2004), p. 040403.
- [28] C. Chin, M. Bartenstein, A. Altmeyer, S. Riedl, S. Jochim, J. H. Denschlag, and R. Grimm, *Observation of the Pairing Gap in a Strongly Interacting Fermi Gas*, Science, 305 (2004), pp. 1128–1130.
- [29] J. L. Roberts, N. R. Claussen, S. L. Cornish, E. A. Donley, E. A. Cornell, and C. E. Wieman, *Controlled Collapse of a Bose-Einstein Condensate*, Phys. Rev. Lett., 86 (2001), pp. 4211–4214.
- [30] G. Thalhammer, G. Barontini, L. D. Sarlo, J. Catani, F. Minardi, and M. Inguscio, *Double Species Bose-Einstein Condensate with Tunable Interspecies Interactions*, Phys. Rev. Lett., 100 (2008), p. 210402.
- [31] A. Schirotzek, C.-H. Wu, A. Sommer, and M. W. Zwierlein, *Observation of Fermi Polarons in a Tunable Fermi Liquid of Ultracold Atoms*, Phys. Rev. Lett., 102 (2009), p. 230402.
- [32] S. Palzer, C. Zipkes, C. Sias, and M. Köhl, *Quantum Transport through a Tonks-Girardeau Gas*, Phys. Rev. Lett., 103 (2009), p. 150601.
- [33] H. T. Ng and S. Bose, *Single-atom-aided probe of the decoherence of a Bose-Einstein condensate*, Phys. Rev. A, 78 (2008), p. 023610.
- [34] M. Bruderer and D. Jaksch, *Probing BEC phase fluctuations with atomic quantum dots*, New Journal of Physics, 8 (2006), p. 87.
- [35] S. Kuhr, W. Alt, D. Schrader, I. Dotsenko, Y. Miroshnychenko, W. Rosenfeld, M. Khudaverdyan, V. Gomer, A. Rauschenbeutel, and D. Meschede, *Coherence Properties and Quantum State Transportation in an Optical Conveyor Belt*, Phys. Rev. Lett., 91 (2003), p. 213002.
- [36] W. S. Bakr, J. I. Gillen, A. Peng, S. Foelling, and M. Greiner, *A quantum gas microscope - detecting single atoms in a Hubbard regime optical lattice*, Nature, 462 (2009), pp. 74–77.

- [37] T. Gericke, P. Würtz, D. Reitz, T. Langen, and H. Ott, *High Resolution Scanning Electron Microscopy of an Ultracold Quantum Gas*, Nature Physics, 4 (2008), p. 949.
- [38] Y. Miroshnychenko, W. Alt, I. Dotsenko, L. Förster, M. Khudaverdyan, D. Meschede, D. Schrader, and A. Rauschenbeutel, *Quantum engineering: An atom-sorting machine*, Nature, 442 (2006), p. 151.
- [39] M. Khudaverdyan, W. Alt, I. Dotsenko, L. Förster, S. Kuhr, D. Meschede, Y. Miroshnychenko, D. Schrader, and A. Rauschenbeutel, *Adiabatic quantum state manipulation of single trapped atoms*, Phys. Rev. A, 71 (2005), p. 031404.
- [40] M. Karski, L. Förster, J. M. Choi, W. Alt, A. Widera, and D. Meschede, *Nearest-Neighbor Detection of Atoms in a 1D Optical Lattice by Fluorescence Imaging*, Phys. Rev. Lett., 102 (2009), p. 053001.
- [41] A. Gaëtan, Y. Miroshnychenko, T. Wilk, A. Chotia, M. Viteau, D. Comparat, P. Pillet, A. Browaeys, and P. Grangier, *Observation of collective excitation of two individual atoms in the Rydberg blockade regime*, Nature Physics, 5 (2009), pp. 115 – 118.
- [42] E. Urban, T. A. Johnson, T. Henage, L. Isenhower, D. D. Yavuz, T. G. Walker, and M. Saffman, *Observation of Rydberg blockade between two atoms*, Nature Physics, 5 (2009), pp. 110 – 114.
- [43] L. You, X. X. Yi, and X. H. Su, *Quantum logic between atoms inside a high-Q optical cavity*, Phys. Rev. A, 67 (2003), p. 032308.
- [44] A. J. Daley, P. O. Fedichev, and P. Zoller, *Single-atom cooling by superfluid immersion: A nondestructive method for qubits*, Phys. Rev. A, 69 (2004), p. 022306.
- [45] A. Griessner, A. J. Daley, S. R. Clark, D. Jaksch, and P. Zoller, *Dark-State Cooling of Atoms by Superfluid Immersion*, Phys. Rev. Lett., 97 (2006), p. 220403.
- [46] A. Klein and M. Fleischhauer, *Interaction of impurity atoms in Bose-Einstein condensates*, Phys. Rev. A, 71 (2005), p. 033605.
- [47] L. Santos, G. V. Shlyapnikov, P. Zoller, and M. Lewenstein, *Bose-Einstein Condensation in Trapped Dipolar Gases*, Phys. Rev. Lett., 85 (2000), pp. 1791–1794.
- [48] T. Koch, T. Lahaye, J. Metz, B. Fröhlich, A. Griesmaier, and T. Pfau, *Stabilization of a purely dipolar quantum gas against collapse*, Nature Physics, 4 (2008), p. 218.
- [49] K. Góral, L. Santos, and M. Lewenstein, *Quantum Phases of Dipolar Bosons in Optical Lattices*, Phys. Rev. Lett., 88 (2002), p. 170406.
- [50] S. Yi, T. Li, and C. P. Sun, *Novel Quantum Phases of Dipolar Bose Gases in Optical Lattices*, Phys. Rev. Lett., 98 (2007), p. 260405.

- [51] M. G. Kozlov and L. N. Labzowsky, *Parity violation effects in diatomics*, Journal of Physics B, 28 (1995), pp. 1933–1961.
- [52] N. S. Mosyagin, M. G. Kozlov, and A. V. Titov, *Electric dipole moment of the electron in the YbF molecule*, Journal of Physics B, 31 (1998), pp. L763–L767.
- [53] D. DeMille, *Quantum Computation with Trapped Polar Molecules*, Phys. Rev. Lett., 88 (2002), p. 067901.
- [54] F. A. van Abeelen and B. J. Verhaar, *Time-Dependent Feshbach Resonance Scattering and Anomalous Decay of a Na Bose-Einstein Condensate*, Phys. Rev. Lett., 83 (1999), pp. 1550–1553.
- [55] F. H. Mies, E. Tiesinga, and P. S. Julienne, *Manipulation of Feshbach resonances in ultracold atomic collisions using time-dependent magnetic fields*, Phys. Rev. A, 61 (2000), p. 022721.
- [56] E. A. Donley, N. R. Claussen, S. T. Thompson, and C. E. Wieman, *Atom–molecule coherence in a Bose–Einstein condensate*, Nature, 417 (2002), pp. 529–533.
- [57] S. T. Thompson, E. Hodby, and C. E. Wieman, *Ultracold Molecule Production via a Resonant Oscillating Magnetic Field*, Phys. Rev. Lett., 95 (2005), p. 190404.
- [58] C. Klempt, T. Henninger, O. Topic, M. Scherer, L. Kattner, E. Tiemann, W. Ertmer, and J. J. Arlt, *Radio-frequency association of heteronuclear Feshbach molecules*, Phys. Rev. A, 78 (2008), p. 061602.
- [59] T. M. Hanna, T. Köhler, and K. Burnett, *Association of molecules using a resonantly modulated magnetic field*, Phys. Rev. A, 75 (2007), p. 013606.
- [60] J. Herbig, T. Kraemer, M. Mark, T. Weber, C. Chin, H.-C. Nägerl, and R. Grimm, *Preparation of a Pure Molecular Quantum Gas*, Science, 301 (2003), pp. 1510–1513.
- [61] M. Mark, T. Kraemer, J. Herbig, C. Chin, H.-C. Nägerl, and R. Grimm, *Efficient creation of molecules from a cesium Bose-Einstein condensate*, Europhys. Lett., 69 (2005), p. 706.
- [62] K. Xu, T. Mukaiyama, J. R. Abo-Shaeer, J. K. Chin, D. E. Miller, and W. Ketterle, *Formation of Quantum-Degenerate Sodium Molecules*, Phys. Rev. Lett., 91 (2003), p. 210402.
- [63] S. Dürr, T. Volz, A. Marte, and G. Rempe, *Observation of Molecules Produced from a Bose-Einstein Condensate*, Phys. Rev. Lett., 92 (2004), p. 020406.
- [64] C. Ospelkaus, S. Ospelkaus, L. Humbert, P. Ernst, K. Sengstock, and K. Bongs, *Ultracold Heteronuclear Molecules in a 3D Optical Lattice*, Phys. Rev. Lett., 97 (2006), p. 120402.

Bibliography

- [65] J. J. Zirbel, K.-K. Ni, S. Ospelkaus, T. L. Nicholson, M. L. Olsen, P. S. Julienne, C. E. Wieman, J. Ye, and D. S. Jin, *Heteronuclear molecules in an optical dipole trap*, Phys. Rev. A, 78 (2008), p. 013416.
- [66] S. B. Papp and C. E. Wieman, *Observation of Heteronuclear Feshbach Molecules from a ^{85}Rb - ^{87}Rb Gas*, Phys. Rev. Lett., 97 (2006), p. 180404.
- [67] F. Lang, K. Winkler, C. Strauss, R. Grimm, and J. H. Denschlag, *Ultracold Triplet Molecules in the Rovibrational Ground State*, Phys. Rev. Lett., 101 (2008), p. 133005.
- [68] K.-K. Ni, S. Ospelkaus, M. H. G. de Miranda, A. Pe'er, B. Neyenhuis, J. J. Zirbel, S. Kotochigova, P. S. Julienne, D. S. Jin, and J. Ye, *A High Phase-Space-Density Gas of Polar Molecules*, Science, 322 (2008), pp. 231–235.
- [69] A. Einstein, *Quantentheorie des einatomigen idealen Gases*, Sitzungsberichte der Preussischen Akademie der Wissenschaften, Physikalisch-mathematische Klasse, (1924), p. 261–267.
- [70] C. Pethick and H. Smith. *Bose Einstein Condensation in dilute gases*. Cambridge University Press, 2002.
- [71] V. Bagnato, D. E. Pritchard, and D. Kleppner, *Bose-Einstein condensation in an external potential*, Phys. Rev. A, 35 (1987), pp. 4354–4358.
- [72] N. N. Bogoliubov, *On the theory of superfluidity*, J. Phys. (USSR), 11 (1947), p. 23.
- [73] E. P. Gross, *Structure of a quantized vortex in boson systems*, Nuovo Cimento, 20 (1961), p. 454.
- [74] L. P. Pitaevskii, *Vortex lines in an imperfect Bose gas*, Sov. Phys. JETP, 13 (1961), p. 451.
- [75] E. P. Gross, *Hydrodynamics of a Superfluid Condensate*, Journal of Mathematical Physics, 4 (1963), pp. 195–207.
- [76] E. G. M. van Kempen, S. J. J. M. F. Kokkelmans, D. J. Heinzen, and B. J. Verhaar, *Interisotope Determination of Ultracold Rubidium Interactions from Three High-Precision Experiments*, Phys. Rev. Lett., 88 (2002), p. 093201.
- [77] P. J. Leo, C. J. Williams, and P. S. Julienne, *Collision Properties of Ultracold ^{133}Cs Atoms*, Phys. Rev. Lett., 85 (2000), pp. 2721–2724.
- [78] S. Falke, H. Knöckel, J. Friebe, M. Riedmann, E. Tiemann, and C. Lisdat, *Potassium ground-state scattering parameters and Born-Oppenheimer potentials from molecular spectroscopy*, Phys. Rev. A, 78 (2008), p. 012503.

- [79] M. Haas, V. Leung, D. Frese, D. Haubrich, S. John, C. Weber, A. Rauschenbeutel, and D. Meschede, *Species-selective microwave cooling of a mixture of rubidium and caesium atoms*, New Journal of Physics, 9 (2007), p. 147.
- [80] G. Thalhammer, G. Barontini, J. Catani, F. Rabatti, C. Weber, A. Simoni, F. Minardi, and M. Inguscio, *Collisional and molecular spectroscopy in an ultracold Bose–Bose mixture*, New Journal of Physics, 11 (2009), p. 055044 (12pp).
- [81] G. Breit and I. I. Rabi, *Measurement of Nuclear Spin*, Phys. Rev., 38 (1931), pp. 2082–2083.
- [82] F. H. Mies, C. J. Williams, P. S. Julienne, and M. Krauss, *Estimating Bounds on Collisional Relaxation Rates of Spin-Polarized ^{87}Rb Atoms at Ultracold Temperatures*, J. Res. Natl. Inst. Stand. Technol., 101 (1996), p. 521.
- [83] P. O. Fedichev, M. W. Reynolds, and G. V. Shlyapnikov, *Three-Body Recombination of Ultracold Atoms to a Weakly Bound s Level*, Phys. Rev. Lett., 77 (1996), p. 2921.
- [84] J. Stenger, S. Inouye, M. R. Andrews, H.-J. Miesner, D. M. Stamper-Kurn, and W. Ketterle, *Strongly Enhanced Inelastic Collisions in a Bose-Einstein Condensate near Feshbach Resonances*, Phys. Rev. Lett., 82 (1999), pp. 2422–2425.
- [85] T. Weber, J. Herbig, M. Mark, H.-C. Nägerl, and R. Grimm, *Three-Body Recombination at Large Scattering Lengths in an Ultracold Atomic Gas*, Phys. Rev. Lett., 91 (2003), p. 123201.
- [86] B. D. Esry, C. H. Greene, and J. P. Burke, *Recombination of Three Atoms in the Ultracold Limit*, Phys. Rev. Lett., 83 (1999), pp. 1751–1754.
- [87] P. F. Bedaque, E. Braaten, and H.-W. Hammer, *Three-body Recombination in Bose Gases with Large Scattering Length*, Phys. Rev. Lett., 85 (2000), pp. 908–911.
- [88] H. Feshbach, *Unified theory of nuclear reactions*, Annals of Physics, 5 (1958), pp. 357 – 390.
- [89] G. Inoue, J. K. Ku, and D. W. Setser, *Photoassociative laser-induced fluorescence of XeCl^* and kinetics of $\text{XeCl}(B)$ and $\text{XeCl}(C)$ in Xe* , The Journal of Chemical Physics, 80 (1984), pp. 6006–6019.
- [90] H. R. Thorsheim, J. Weiner, and P. S. Julienne, *Laser-induced photoassociation of ultracold sodium atoms*, Phys. Rev. Lett., 58 (1987), pp. 2420–2423.
- [91] V. Efimov, *Energy levels arising from resonant two-body forces in a three-body system*, Physics Letters B, 33 (1970), pp. 563 – 564.
- [92] A. Simoni, M. Zaccanti, C. D’Errico, M. Fattori, G. Roati, M. Inguscio, and G. Modugno, *Near-threshold model for ultracold KRb dimers from interisotope Feshbach spectroscopy*, Phys. Rev. A, 77 (2008), p. 052705.

Bibliography

- [93] A. J. Moerdijk, B. J. Verhaar, and A. Axelsson, *Resonances in ultracold collisions of ^6Li , ^7Li , and ^{23}Na* , Phys. Rev. A, 51 (1995), pp. 4852–4861.
- [94] E. Braaten and H.-W. Hammer, *Universality in few-body systems with large scattering length*, Physics Reports, 428 (2006), pp. 259 – 390.
- [95] E. Timmermans, P. Tommasini, M. Hussein, and A. Kerman, *Feshbach resonances in atomic Bose-Einstein condensates*, Phys. Rep., 315 (1999), p. 199.
- [96] T. Köhler, K. Góral, and P. S. Julienne, *Production of cold molecules via magnetically tunable Feshbach resonances*, Rev. Mod. Phys., 78 (2006), p. 1311.
- [97] M. Stoll and T. Köhler, *Production of three-body Efimov molecules in an optical lattice*, Phys. Rev. A, 72 (2005), p. 022714.
- [98] D. S. Petrov, *Three-Boson Problem near a Narrow Feshbach Resonance*, Phys. Rev. Lett., 93 (2004), p. 143201.
- [99] G. F. Gribakin and V. V. Flambaum, *Calculation of the scattering length in atomic collisions using the semiclassical approximation*, Phys. Rev. A, 48 (1993), pp. 546–553.
- [100] K. Goral, T. Kohler, S. A. Gardiner, E. Tiesinga, and P. S. Julienne, *Adiabatic association of ultracold molecules via magnetic-field tunable interactions*, Journal of Physics B, 37 (2004), pp. 3457–3500.
- [101] K. L. Corwin, Z.-T. Lu, C. F. Hand, R. J. Epstein, and C. E. Wieman, *Frequency-Stabilized Diode Laser with the Zeeman Shift in an Atomic Vapor*, Appl. Opt., 37 (1998), pp. 3295–3298.
- [102] A. Millett-Sikking, I. G. Hughes, P. Tierney, and S. L. Cornish, *DAVLL lineshapes in atomic rubidium*, Journal of Physics B, 40 (2007), pp. 187–198.
- [103] C. Wieman and T. W. Hänsch, *Doppler-Free Laser Polarization Spectroscopy*, Phys. Rev. Lett., 36 (1976), pp. 1170–1173.
- [104] H. J. Metcalf and P. van der Straten. *Laser Cooling and Trapping*. Springer Verlag, 1999.
- [105] S. Chu, L. Hollberg, J. E. Bjorkholm, A. Cable, and A. Ashkin, *Three-dimensional viscous confinement and cooling of atoms by resonance radiation pressure*, Phys. Rev. Lett., 55 (1985), pp. 48–51.
- [106] J. Dalibard and C. Cohen-Tannoudji, *Laser cooling below the Doppler limit by polarization gradients: simple theoretical models*, J. Opt. Soc. Am. B, 6 (1989), pp. 2023–2045.

- [107] E. L. Raab, M. Prentiss, A. Cable, S. Chu, and D. E. Pritchard, *Trapping of Neutral Sodium Atoms with Radiation Pressure*, Phys. Rev. Lett., 59 (1987), pp. 2631–2634.
- [108] T. Walker, D. Sesko, and C. Wieman, *Collective behavior of optically trapped neutral atoms*, Phys. Rev. Lett., 64 (1990), pp. 408–411.
- [109] D. Sesko, T. Walker, C. Monroe, A. Gallagher, and C. Wieman, *Collisional losses from a light-force atom trap*, Phys. Rev. Lett., 63 (1989), pp. 961–964.
- [110] A. Gozzini, F. Mango, J. H. Xu, G. Alzetta, F. Maccarrone, and R. A. Bernheim, *Light-induced ejection of alkali atoms in polysiloxane coated cells*, Il Nuovo Cimento D, 15 (1993), p. 709.
- [111] C. Klempt, T. van Zoest, T. Henninger, O. Topic, E. Rasel, W. Ertmer, and J. Arlt, *Ultraviolet light-induced atom desorption for large rubidium and potassium magneto-optical traps*, Phys. Rev. A, 73 (2006), p. 013410.
- [112] A. L. Migdall, J. V. Prodan, W. D. Phillips, T. H. Bergeman, and H. J. Metcalf, *First Observation of Magnetically Trapped Neutral Atoms*, Phys. Rev. Lett., 54 (1985), pp. 2596–2599.
- [113] E. Majorana, *Atomi orientati in campo magnetico variabile*, Nuovo Cimento, 9 (1932), p. 43.
- [114] W. Petrich, M. H. Anderson, J. R. Ensher, and E. A. Cornell, *Stable, Tightly Confining Magnetic Trap for Evaporative Cooling of Neutral Atoms*, Phys. Rev. Lett., 74 (1995), pp. 3352–3355.
- [115] D. E. Pritchard, *Cooling Neutral Atoms in a Magnetic Trap for Precision Spectroscopy*, Phys. Rev. Lett., 51 (1983), pp. 1336–1339.
- [116] T. Esslinger, I. Bloch, and T. W. Hänsch, *Bose-Einstein condensation in a quadrupole-Ioffe-configuration trap*, Phys. Rev. A, 58 (1998), pp. R2664–R2667.
- [117] M. Haas, *Sympathetisches Kühlen in einer Rubidium-Cäsium-Mischung: Erzeugung ultrakalter Cäsiumatome*, PhD thesis, Universität Bonn, 2007.
- [118] C. Cohen-Tannoudji and S. Reynaud, *Dressed-atom description of resonance fluorescence and absorption spectra of a multi-level atom in an intense laser beam*, Journal of Physics B, 10 (1977), pp. 345–363.
- [119] R. Grimm, M. Weidemüller, and Y. B. Ovchinnikov, *Optical dipole traps for neutral atoms*, Advances in Atomic, Molecular and Optical Physics, 42 (2000), p. 95.
- [120] W. Alt, *Optical control of single neutral atoms*, PhD thesis, Universität Bonn, 2004.

- [121] H. Nyquist, *Thermal Agitation of Electric Charge in Conductors*, Phys. Rev., 32 (1928), pp. 110–113.
- [122] J. B. Johnson, *Thermal Agitation of Electricity in Conductors*, Phys. Rev., 32 (1928), p. 97.
- [123] D. Meschede. *Optik, Licht und Laser*. Teubner, 1999.
- [124] W. Ketterle, D. S. Durfee, and D. M. Stamper-Kurn, *Making, probing and understanding: Bose-Einstein Condensation in Atomic Gases*, Proceedings of the international school of physics Enrico Fermi, Course CXL (1999), p. 67.
- [125] M. K. Tey, Z. Chen, S. A. Aljunid, B. Chng, F. Huber, G. Maslennikov, and C. Kurtsiefer, *Strong interaction between light and a single trapped atom without the need for a cavity*, Nature Physics, 4 (2008), p. 924.
- [126] D. Haubrich, H. Schadwinkel, F. Strauch, B. Ueberholz, R. Wynands, and D. Meschede, *Observation of individual neutral atoms in magnetic and magneto-optical traps*, Europhys. Lett., 34 (1996), pp. 663–668.
- [127] C. Monroe, W. Swann, H. Robinson, and C. Wieman, *Very cold trapped atoms in a vapor cell*, Phys. Rev. Lett., 65 (1990), pp. 1571–1574.
- [128] D. Haubrich, A. Höpe, and D. Meschede, *A simple model for optical capture of atoms in strong magnetic quadrupole fields*, Opt. Commun., 102 (1993), p. 225.
- [129] S. Kuhr, *A controlled quantum system of individual neutral atoms*, PhD thesis, Universität Bonn, 2003.
- [130] T. Weikum. *Ein System zur Fluoreszenzdetektion einzelner Cäsiumatome in einem Rubidium-Bose-Einstein-Kondensat*, 2009.
- [131] S. A. Hopkins and A. V. Durrant, *Parameters for polarization gradients in three-dimensional electromagnetic standing waves*, Phys. Rev. A, 56 (1997), pp. 4012–4022.
- [132] T. Walker and P. Feng. *Measurements of Collisions Between Laser-Cooled Atoms*. volume 34 of *Advances In Atomic, Molecular, and Optical Physics*, pp. 125 – 170. Academic Press, 1994.
- [133] J. Weiner, V. S. Bagnato, S. Zilio, and P. S. Julienne, *Experiments and theory in cold and ultracold collisions*, Rev. Mod. Phys., 71 (1999), pp. 1–85.
- [134] B. Ueberholz, *Kalte Stöße in einer magnetooptischen Falle mit hohem Magnetfeldgradienten*, PhD thesis, Universität Bonn, 2001.
- [135] J. Vigué, *Possibility of applying laser-cooling techniques to the observation of collective quantum effects*, Phys. Rev. A, 34 (1986), pp. 4476–4479.

- [136] A. Gallagher and D. E. Pritchard, *Exoergic collisions of cold Na*-Na*, Phys. Rev. Lett., 63 (1989), pp. 957–960.
- [137] P. S. Julienne and J. Vigué, *Cold collisions of ground- and excited-state alkali-metal atoms*, Phys. Rev. A, 44 (1991), pp. 4464–4485.
- [138] D. A. Steck, *Rubidium 87 D Line Data*, <http://steck.us/alkalidata>, revision 2.0.1 (2008).
- [139] M. L. Harris, P. Tierney, and S. L. Cornish, *Magnetic trapping of a cold Rb-Cs atomic mixture*, Journal of Physics B, 41 (2008), p. 035303 (9pp).
- [140] S. Kotochigova, P. S. Julienne, and E. Tiesinga, *Ab initio calculation of the KRb dipole moments*, Phys. Rev. A, 68 (2003), p. 022501.
- [141] J. Catani, *A New Apparatus for ultracold K-Rb Bose-Bose atomic mixtures*, PhD thesis, Università degli studi di Firenze, 2006.
- [142] K. Dieckmann, R. J. C. Spreeuw, M. Weidemüller, and J. T. M. Walraven, *Two-dimensional magneto-optical trap as a source of slow atoms*, Phys. Rev. A, 58 (1998), pp. 3891–3895.
- [143] C. Fort, A. B. L. Cacciapuoti, F. Cataliotti, M. Prevedelli, G. Tino, and M. Inguscio, *Cooling mechanisms in potassium magneto-optical traps*, Eur. Phys. J. D, 3 (1998), p. 113.
- [144] R. Wang, M. Liu, F. Minardi, and M. Kasevich, *Reaching ^7Li quantum degeneracy with a minitrap*, Phys. Rev. A, 75 (2007), p. 013610.
- [145] J. F. Bertelsen and K. M. Imer, *Association of heteronuclear molecules in a harmonic oscillator well*, Phys. Rev. A, 76 (2007), p. 043615.
- [146] S. Ospelkaus, *Quantum Degenerate Fermi-Bose Mixtures of ^{40}K and ^{87}Rb in 3D Optical Lattices*, PhD thesis, Universität Hamburg, 2006.
- [147] T. Köhler, E. Tiesinga, and P. S. Julienne, *Spontaneous Dissociation of Long-Range Feshbach Molecules*, Phys. Rev. Lett., 94 (2005), p. 020402.
- [148] S. T. Thompson, E. Hodby, and C. E. Wieman, *Spontaneous Dissociation of ^{85}Rb Feshbach Molecules*, Phys. Rev. Lett., 94 (2005), p. 020401.
- [149] S. Knoop, M. Mark, F. Ferlaino, J. G. Danzl, T. Kraemer, H.-C. Nägerl, and R. Grimm, *Metastable Feshbach Molecules in High Rotational States*, Phys. Rev. Lett., 100 (2008), p. 083002.
- [150] C. A. Regal, M. Greiner, and D. S. Jin, *Lifetime of Molecule-Atom Mixtures near a Feshbach Resonance in ^{40}K* , Phys. Rev. Lett., 92 (2004), p. 083201.

Bibliography

- [151] T. Mukaiyama, J. R. Abo-Shaeer, K. Xu, J. K. Chin, and W. Ketterle, *Dissociation and Decay of Ultracold Sodium Molecules*, Phys. Rev. Lett., 92 (2004), p. 180402.
- [152] E. Braaten and H.-W. Hammer, *Enhanced dimer relaxation in an atomic and molecular Bose-Einstein condensate*, Phys. Rev. A, 70 (2004), p. 042706.
- [153] J. P. D’Incao and B. D. Esry, *Scattering Length Scaling Laws for Ultracold Three-Body Collisions*, Phys. Rev. Lett., 94 (2005), p. 213201.
- [154] G. Thalhammer, K. Winkler, F. Lang, S. Schmid, R. Grimm, and J. H. Denschlag, *Long-Lived Feshbach Molecules in a Three-Dimensional Optical Lattice*, Phys. Rev. Lett., 96 (2006), p. 050402.
- [155] T. Volz, N. Syassen, D. M. Bauer, E. Hansis, S. Dürr, and G. Rempe, *Preparation of a quantum state with one molecule at each site of an optical lattice*, Nature Physics, 2 (2006), p. 692.
- [156] C. Weber, G. Barontini, J. Catani, G. Thalhammer, M. Inguscio, and F. Minardi, *Association of ultracold double-species bosonic molecules*, Phys. Rev. A, 78 (2008), p. 061601.
- [157] D. M. Bauer, M. Lettner, C. Vo, G. Rempe, and S. Dürr, *Controlling a magnetic Feshbach resonance with laser light*, Nature Physics, 5 (2009), p. 339.
- [158] C. H. Schunck, M. W. Zwierlein, C. A. Stan, S. M. F. Raupach, W. Ketterle, A. Simoni, E. Tiesinga, C. J. Williams, and P. S. Julienne, *Feshbach resonances in fermionic ${}^6\text{Li}$* , Phys. Rev. A, 71 (2005), p. 045601.
- [159] C. Ticknor, C. A. Regal, D. S. Jin, and J. L. Bohn, *Multiplet structure of Feshbach resonances in nonzero partial waves*, Phys. Rev. A, 69 (2004), p. 042712.
- [160] S. D. Gensemer, P. L. Gould, P. J. Leo, E. Tiesinga, and C. J. Williams, *Ultracold ${}^{87}\text{Rb}$ ground-state hyperfine-changing collisions in the presence and absence of laser light*, Phys. Rev. A, 62 (2000), p. 030702.
- [161] L. J. LeBlanc and J. H. Thywissen, *Species-specific optical lattices*, Phys. Rev. A, 75 (2007), p. 053612.
- [162] K. Pilch, A. D. Lange, A. Prantner, G. Kerner, F. Ferlaino, H.-C. Nägerl, and R. Grimm, *Observation of interspecies Feshbach resonances in an ultracold Rb-Cs mixture*, Phys. Rev. A, 79 (2009), p. 042718.
- [163] F. Diedrich, J. C. Bergquist, W. M. Itano, and D. J. Wineland, *Laser Cooling to the Zero-Point Energy of Motion*, Phys. Rev. Lett., 62 (1989), pp. 403–406.
- [164] W. Neuhauser, M. Hohenstatt, P. Toschek, and H. Dehmelt, *Optical-Sideband Cooling of Visible Atom Cloud Confined in Parabolic Well*, Phys. Rev. Lett., 41 (1978), pp. 233–236.

- [165] J. Javanainen and S. Stenholm, *Laser cooling of trapped particles III: The Lamb-Dicke limit*, Applied Physics A, 24 (1981), p. 151.
- [166] K. Bergmann, H. Theuer, and B. W. Shore, *Coherent population transfer among quantum states of atoms and molecules*, Rev. Mod. Phys., 70 (1998), pp. 1003–1025.
- [167] V. Efimov, *Weakly-bound states of three resonantly-interacting particles*, Sov. J. Nucl. Phys., 12 (1971), pp. 589–595.
- [168] G. Barontini, C. Weber, F. Rabatti, J. Catani, G. Thalhammer, M. Inguscio, and F. Minardi, *Observation of Heteronuclear Atomic Efimov Resonances*, Phys. Rev. Lett., 103 (2009), p. 043201.
- [169] E. Nielsen and J. H. Macek, *Low-Energy Recombination of Identical Bosons by Three-Body Collisions*, Phys. Rev. Lett., 83 (1999), pp. 1566–1569.
- [170] M. Zaccanti, B. Deissler, C. D’Errico, M. Fattori, M. Jona-Lasinio, S. Müller, G. Roati, M. Inguscio, and G. Modugno, *Observation of an Efimov spectrum in an atomic system*, Nature Physics, 5 (2009), p. 586.
- [171] S. Knoop, F. Ferlaino, M. Mark, M. Berninger, H. Schöbel, H.-C. Nägerl, and R. Grimm, *Observation of an Efimov-like trimer resonance in ultracold atom-dimer scattering*, Nature Physics, 5 (2009), p. 227.
- [172] K. Helfrich and H.-W. Hammer, *Resonant atom-dimer relaxation in ultracold atoms*, Europhys. Lett., 86 (2009), p. 53003.
- [173] D. A. Steck, *Cesium D Line Data*, <http://steck.us/alkalidata>, revision 1.6 (2003).
- [174] E. B. Saloman, *A resonance ionization spectroscopy/resonance ionization mass spectrometry data service. IV - Data sheets for Be, In, Li, K, Rb, Ag, Ti, V and an update of the data sheet for Ni*, Spectrochimica Acta, 48B (1993), pp. 1139–1203.

Bibliography

Danke! Grazie!

An dieser Stelle möchte ich mich bei all denjenigen bedanken, die mich während meiner Promotionszeit in Bonn und in Florenz unterstützt haben.

An erster Stelle danke ich Prof. D. Meschede, der mir die Möglichkeit gegeben hat an einem interessanten Forschungsprojekt zu arbeiten.

Likewise, I want to thank Prof. M. Inguscio who gave me the possibility to join his group for half a year and to work on a fascinating experiment. Moreover, I thank him to be my second supervisor.

Ein besonderer Dank geht an meine Bonner Laborkollegen Shincy John und Nicolas Spethmann mit denen ich die längste Zeit am BEC-Experiment verbracht habe. Die gute und harmonische Zusammenarbeit, sowie euer unermüdlicher Einsatz hat dazu beigetragen, dass mir die Laborarbeit viel Spaß gemacht hat. Euch danke ich auch für das Korrekturlesen meiner Arbeit.

Bedanken möchte ich mich auch bei unseren ehemaligen Kollegen Dr. Michael Haas, der mich ins Experiment eingeführt hat, und unserer Diplomandin Tatjana Weikum für die tatkräftige Unterstützung.

Als Postdoc unseres Teams hat Dr. Artur Widera uns mit seinem immerwährenden Optimismus motiviert. Seine Erfahrung und sein Ideenreichtum haben uns in unserer Forschungsarbeit sehr unterstützt. Ihm danke ich auch für das kritische Lesen und die konstruktive Kritik an meiner Doktorarbeit.

Auch Dr. Wolfgang Alt hat uns immer als Ansprechpartner zur Verfügung gestanden und uns insbesondere beim Aufbau von Elektronik und der Einzelatomdetektion hilfreiche Hinweise gegeben.

Grazie anche al team BEC3! It was a pleasure to join your group for some months. From the very first day you trust me with your experiment. I could learn a lot from each member of your team: Giovanni Barontini, Dr. Jacopo Catani, Francesco Rabatti, Dr. Gregor Thalhammer, and the group leader Dr. Francesco Minardi!

Ein großen Anteil an meiner Arbeit haben natürlich auch die Elektronik- und Feinmechanikwerkstatt. Stellvertretend sind hier die jeweiligen Leiter Herr Brähler und Herr Langen zu nennen.

Allen Mitarbeitern der Verwaltungsetage Annelise Miglo, Fien Latumahina, Ilona Jaschke und Dr. Dietmar Haubrich danke ich für ihre stetige Hilfsbereitschaft und die angenehme Atmosphäre im Institut. Annelise Miglo danke ich besonders für das Korrekturlesen meiner Arbeit.

Besonders bedanken möchte ich mich bei meinen Eltern, die mich während meiner

Bibliography

gesamten Studium- und Promotionszeit in jeglicher Weise unterstützt haben.
Der Bonn-Cologne Graduate School of Physics and Astronomy danke ich für die finanzielle Unterstützung.